ORKUSTOFNUN
NATIONAL ENERGY AUTHORITY

THE UNITED NATIONS UNIVERSITY

THE MT/AMT ELECTROMAGNETIC METHOD IN GEOTHERMAL EXPLORATION

Stanley H. Ward
and
Philip E. Wannamaker

UNU Geothermal Training Programme, Iceland.

Report 1983-5

THE MT/AMT ELECTROMAGNETIC METHOD IN GEOTHERMAL EXPLORATION

by

Stanley H. Ward
and
Philip E. Wannamaker

Earth Science Laboratory
University of Utah Research Institute
and
Department of Geology and Geophysics
University of Utah

TABLE OF CONTENTS

FIGURE CAPTIONS

Figure 1. Generalized spectrum of natural magnetic fields (after Campbell, 1967).

Figure 2. Typical model, apparent resistivity, and impedance phase for a layered (1D) earth.

Figure 3. Model, modes of excitation, and formulation for a 2D earth.

Figure 4. Illustrative behavior of electric and magnetic fields over a 2D body in a homogeneous half-space.

Figure 5. Illustration of surface charges at boundaries, due to an electric field excitation.

Figure 6. Illustration of conceptual notions of current gathering and local induction.

Figure 7. Typical behavior of TE and TM mode apparent resistivities and impedance phases at two points near a 2D body in a homogeneous half-space.

Figure 8. Plan view of measuring axes (x,y) and symmetry axes (x',y') for an MT survey over 2D body in a homogeneous half-space.

Figure 9. Illustration of impossibility of mode identification for an equidimensional 3D body.

Figure 10. Plan view of measuring axes (x,y) and symmetry axes (x',y') for an MT survey over a 3D body in a homogeneous half-space.

Figure 11. Plan map showing location of measuring points A and B over a 3D body in homogeneous half-space.

Figure 12. Typical apparent resistivity and impedance phase curves for points A and B of Figure 11.

Figure 13. Magnetotelluric sensor deployment in the field (after Sternberg et al., 1982).

Figure 14. Conoco Research MT system (after Sternberg et al., 1982).

Figure 15. Earth Science Laboratory MT system overview (after Stodt, 1983).

Figure 16. E field and coil H field receivers of Earth Science Laboratory MT system (after Stodt, 1983).

Figure 17. Distortion of current flow lines due to topography.

Figure 18. TM mode ($E_{\perp}$) and TE mode ($E_{\parallel}$) anomalies over a 2D ridge (after Ngoc, 1980).

Figure 19. Apparent resistivity 1D curve (solid) and computed data points for four different equidimensional 3D slabs (after Ting and Hohmann, 1981).

Figure 20. 3D model of magma chamber in a layered earth (after Newman and Wannamaker, 1983).

Figure 21. Apparent resistivity and impedance phase curves over the magma chamber of Figure 20, layered earth (after Newman and Wannamaker, 1983).

Figure 22. Apparent resistivity and impedance phase curves over the magma chamber of Figure 20, homogeneous half-space (after Newman and Wannamaker, 1983).

Figure 23. Effect of anistropy on apparent resistivities (after Wannamaker, 1983).

Figure 24. Locations of MT/AMT stations, Roosevelt Hot Springs KGRA, Utah (after Wannamaker et al., 1980).

Figure 25. Geologic map of Roosevelt Hot Springs KGRA and vicinity (after Sibbett and Nielson, 1980).

Figure 26. Observed apparent resistivity (ρ_{xy}) pseudosection and continous 1-D inversion results for N-S trending profile of stations over thermal anomaly area. Contour values for pseudosection are in Ω-m. Continuous inversion results plotted on a logarithmic scale with a reference value in Ω-m given for each sounding (note elaborated scale for station 77-16) (after Wannamaker et al., 1980).

Figure 27. Finite element resistivity section computed using lateral inhomogeneities in only the upper 500 m to fit the observations in the top half of Figure 25. Values of individual media in Ω-m (after Wannamaker et al., 1980).

Figure 28. Computed apparent resistivity (ρ_{xy}) pseudosection and continuous 1-D inversion results corresponding to the finite element model of Figure 26. Conventions are as for Figure 25 (after Wannamaker et al., 1980).

Figure 29. Observed apparent resistivity and impedance phase pseudosections for profile B-B' of Figure 24. Contours of ρ_{yx} are in Ω-m while those of ϕ_{yx} are in degrees (after Wannamaker et al., 1980).

Figure 30. Computed apparent resistivity and impedance phase pseudosections for model finite element section for profile B-B' of Figure 24. Contours as in Figure 28 (after Wannamaker et al., 1980).

Figure 31. Best 2-D TM finite element section fitting the observations for profile B-B' of Figure 24. Values of individual media are in Ω-m. Vertical exaggeration is 6:1 (after Wannamaker et al., 1980).

Figure 32. Observed apparent resistivity and impedance phase pseudosections for profile C-C' of Figure 24. Contours as in Figure 28 (after Wannamaker et al., 1980).

Figure 33. Computed apparent resistivity and impedance phase pseudosections for model finite element section for profile C-C' of Figure 24. Contours as in Figure 28 (after Wannamaker et al., 1980).

Figure 34. Best-fit 2-D TM finite element section fitting the observations for profile C-C' of Figure 24. Conventions as in Figure 30 (after Wannamaker et al., 1980).

Figure 35. Best-fit crust and upper mantle resistivity profile for RHS compared to physical model using aqueous electrolytic conduction in rock pores, solid state semiconduction in minerals and electrolytic conduction in partial melts in conjunction with thermally conductive geotherm using data of Chapman et al (1981) (after Wannamaker et al., 1983).

ABSTRACT

The article commences with an overview of the literature. This is followed by a statement of the targets to which the MT/AMT method should be applied. The tensor magnetotelluric/audiofrequency magnetotelluric method is usually too expensive to be used for mapping the resistivity distribution in the shallow parts of a geothermal system. Hence it is more logically used to map regional structure, to attempt to map magma chambers, and to detect and delineate zones of partial melt in the deep crust and upper mantle.

The next part of the article presents a reasonably detailed explanation of the basic principles of the method when applied to 1D, 2D, and 3D earths. It is concluded here that application of the method in 2D and 3D environments requires considerable care in planning data acquisition, data processing, and data interpretation. Seldom is the earth 1D and this has not been recognized, generally, in application of the method. Totally erroneous interpretations of the conductivity distribution in the earth can be made if the dimensionality of the conductivity distribution is not recognized.

The problems encountered in use of MT/AMT surveys involve such noise sources as cultural fields, overburden, topography, current channeling by extraneous geological features and finite source dimensions for the natural fields upon which the method depends. Means for minimizing these noise sources are discussed as are their impact on detecting the MT/AMT targets of interest. The depth of exploration and target detectability are subjects for further discussion.

To illustrate how members of the Earth Science Laboratory of the University of Utah Research Institute use and interpret MT/AMT data within the

framework of integrated geological, geochemical, and geophysical exploration, the case history of MT/AMT studies at the Roosevelt Hot Springs thermal area is presented. Aside from the near surface electrical anomaly associated with fracturing, faulting, and hydrothermal alteration, the only significant anomaly yet resolved by the MT/AMT survey here is attributed to a partial melt in the upper mantle. This partial melt, a manifestation of concentrated diapirism and melting in the eastern Great Basin driving this and nearby geothermal systems, is the subject of ongoing studies.

1.0 INTRODUCTION

The magnetotelluric (MT) and audiomagnetotelluric (AMT) methods have both been used in geothermal exploration in recent years. The magnetotelluric method relies upon measurement of three orthogonal components of natural magnetic fields and two horizontal orthogonal components of natural electric fields in the frequency band 10^{-4} Hz to 10 Hz (Tikhonov, 1950; Cagniard, 1953). The audiomagnetotelluric method relies upon measurements of the same components of magnetic and electric fields, but in the frequency range 10 Hz to 10^4 Hz (Strangway et al., 1973). While the two methods utilize different sets of equipment and rely upon fields from fundamentally different sources, they are essentially the same method and will be so treated in this manuscript to the extent that such is possible. The abbreviation MT/AMT will be used throughout to refer to the method.

A representative set of early references on the magnetotelluric method include Tikhonov (1950), Cagniard (1953), Cantwell (1960), Bostick and Smith (1962), Wait (1962), Swift (1967), Sims et al. (1971), and Vozoff (1972).

The paper by Vozoff (1972) has become the standard reference for a reasonably current description of the magnetotelluric method. Gamble et al. (1979a,b) describe the use of a remote reference for eliminating bias errors in resistivity estimates obtained with MT data. Papers describing its application in geothermal areas include Hermance et al. (1975), Hermance and Pedersen (1977), Stanley et al. (1977), Goldstein et al. (1978), Morrison et al. (1979), Dupis et al. (1980), Gamble et al. (1980), Musmann et al. (1980), Ngoc (1980), Wannamaker et al. (1980), Aiken and Ander (1981), Berktold (1982), Berktold and Kemmerle (1982), Goldstein et al. (1982), Hutton et al.

(1982), Martinez et al. (1982), Stanley (1982), Wannamaker et al. (1983) and others.

Pertinent references on the audiomagnetotelluric method include Keller (1970), Strangway and Vozoff (1970), Strangway et al. (1973), Dupis et al. (1974), Dupis and Iliceto (1974), Keller and Rapolla (1974), Hoover and Long (1975), Hoover et al. (1976), Hoover et al. (1978), Isherwood and Mabey (1978), Jackson and O'Donnell (1980), Long and Kauffman (1980) and others. The article by Strangway et al. (1973) is usually taken as the point of departure for literature surveys of the AMT method.

2.0 THE TARGETS AND BASIS OF THE MT/AMT METHOD

2.1 MT/AMT Targets

The broadband tensor MT/AMT method cannot compete, cost-effectively, with the resistivity or CSAMT methods for delination of the shallower (< 1 km) parts of geothermal systems. Hence, they should be used to detect and delineate deep (> 1 km) targets such as a brine reservoir or hot or partially molten rock in the crust or mantle. Table 1 summarizes these targets but also summarizes the other sources of resistivity anomalies which will influence the MT/AMT results. Except for the regional vertical resistivity profile, these other sources constitute geologic noise in MT/AMT surveys.

One should note, however, that the U. S. Geological Survey (Hoover et al., 1978) has used the scalar AMT method for rapid reconnaissance and shallow exploration of geothermal systems.

2.2 Basic Principles

2.2.1 Sources of fields

The MT/AMT method utilizes the earth's natural electric and magnetic fields to infer the electrical resistivity of the subsurface. Figure 1 contains a generalized spectrum of natural magnetic field amplitude taken from Campbell (1967). There is, of course, a corresponding electric field spectrum, related through Maxwell's equations.

The fields above about 1 Hz are due to worldwide thunderstorms, the principal centers being in equatorial South America, Africa, and the Southwest Pacific. Because the ionosphere is a plasma, i.e. a highly conducting medium, the energy propagates in a wave guide mode in the earth-ionosphere cavity. The resonances shown in Figure 1 are due to constructive interference.

MT TARGETS

- DEEP BRINE RESERVOIR
- HOT, PARTIALLY MOLTEN, ROCK HEAT SOURCE

OTHER SOURCES OF RESISTIVITY ANOMALIES

- SURFICIAL ALTERATION AND BRINE FRACTURE ZONES
- VALLEY SEDIMENTS
- REGIONAL VERTICAL RESISTIVITY PROFILE

TABLE 1

NATURAL MAGNETIC FIELD SPECTRUM

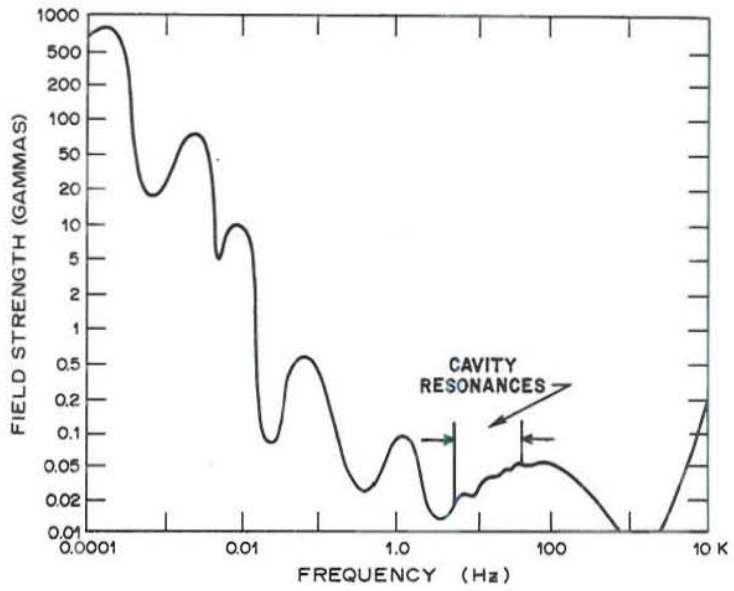

Figure 1. Generalized spectrum of natural magnetic fields (after Campbell, 1967).

Below 1 Hz the fields, called micropulsations, are mainly due to the interaction of the solar wind with the earth's magnetic field and ionosphere. As Figure 1 shows, the amplitude of the electromagnetic field increases with decreasing frequency below 0.1 Hz. Important references on natural electromagnetic fields are Bleil (1964), Matsushita and Campbell (1967), and Jacobs (1970).

These natural fields represent noise for controlled-source electromagnetic methods (CSEM), but they are the source fields for MT. Since low frequencies are needed for deep penetration, it is easy to see from Figure 1 why MT has been used so extensively for crustal studies and deep exploration: the source fields increase at low frequencies for MT while the same fields constitute noise for CSEM, and hence noise increases as frequency is lowered in CSEM. Furthermore, CSEM sources undergo a strong geometric decay, which plane waves do not.

Audiomagnetotelluric (AMT), simply refers to MT in the audio frequency range of 10 to 10^4 Hz. Its advantage is that data can be collected much faster, but, of course, depth of exploration is less than for lower frequencies. Unfortunately, low source fields have hindered the application of AMT, especially in regions remote from the equator. One remedy has been to utilize an artificial source, usually a grounded wire carrying current, located at a large distance from the survey area. This technique is called controlled-source audiomagnetotellurics (CSAMT).

2.2.2 Formulation for a one dimensional (1D) earth

The basic formulation for the MT/AMT method applied to a homogeneous earth is given in Table 2. Orthogonal electric and magnetic field pairs, $[E_x, H_y]$ or $[E_y, H_x]$ are measured at the surface of the earth. These

quantities are simply related to the electromagnetic impedance, Z, of a plane wave. When displacement currents are neglected, which is totally justifiable for earth materials at the frequencies employed in MT/AMT surveys, then the impedance may be computed from

$$Z = \frac{\omega\mu_o}{k} = \frac{E_x}{H_y} = -\frac{E_y}{H_x} . \tag{1}$$

When displacement current are neglected, then, (1) can be rewritten as

$$Z = \frac{\omega\mu_o}{\sqrt{-i\mu_o\sigma\omega}} = \sqrt{i}\ \sqrt{\omega\mu_o\rho} = \sqrt{\omega\mu_o\rho}\ \ e^{i\pi/4} \tag{2}$$

The impedance phase is 45° with E_x leading H_y by this amount. The resistivity of the half-space is then given as

$$\rho = \frac{1}{\omega\mu_o}\,|Z|^2 = 0.2T\ \left|\frac{E_x}{H_y}\right|^2 \tag{3}$$

where E_x is in mv/km, H_y is in gamma, and period T is in seconds.

When the earth is layered, as in Figure 2, the plane wave impedance is given by the recursive formula

$$\hat{Z}_1 = Z_1 \frac{\hat{Z}_2 + Z_1 \tanh\,(i\,k_1h_1)}{Z_1 + \hat{Z}_2 \tanh\,(ik_1h_1)} , \tag{4}$$

$$\hat{Z}_{n-1} = Z_{n-1} \frac{\hat{Z}_n + Z_{n-1} \tanh\,(i\,k_{n-1}\,h_{n-1})}{Z_{n-1} + \hat{Z}_n \tanh\,(i\,k_{n-1}\,h_{n-1})} , \tag{5}$$

in which the $Z_i = \frac{\omega\mu_o}{k_i}$ is the intrinsic impedance of i^{th} medium, $\hat{Z}_i$ is the impedance at the top of the i^{th} layer, while k_i and h_i are the wave number and thickness, respectively, of the i^{th} layer. From (4) one can compute the impedance phase ϕ and the apparent resistivity ρ_a,

$$\hat{Z}_1 = |\hat{Z}_1|e^{i\phi} \tag{6}$$

MT ID

$$Z \equiv \frac{\omega\mu}{k} = \frac{E_x}{H_y} = -\frac{E_y}{H_x}$$

$$k^2 = \mu\epsilon\omega^2 - i\mu\sigma\omega \sim -i\mu\sigma\omega$$

$$\left|\rho_{xy}\right| = \left|\frac{1}{\sigma}\right| = \frac{1}{\mu\omega}\left|\frac{E_x}{H_y}\right|^2 = 0.2T\left|\frac{E_x}{H_y}\right|^2 \text{ in traditional units}$$

but Z=complex, hence ρ_{xy} and ϕ_{xy}

TABLE 2

$$\rho_a = \frac{1}{\omega \mu_o} |\hat{Z}_1|^2 \qquad (7)$$

Figure 2b shows schematically the appearance of the ρ_a versus f and ϕ versus f curves for the three layer earth depicted in Figure 2a. Boehl et al. (1977) show that one can predict the phase from the apparent resistivity approximately by

$$\phi \simeq 45^o + 45^o \frac{\partial \ln \rho_a}{\partial \ln \omega} \qquad (8)$$

which may be observed in principle in Figure 2b. Equation (8) is based on an assumption that the resistivity and impedance phase are related through a Hilbert transform for a 1D earth (Kunetz, 1972). Our observations suggest, but do not prove, that the Hilbert transform relationship usually is obeyed by 2D and 3D earths (Wannamaker et al., 1982).

2.2.3 Formulation for a two dimensional (2D) earth

2.2.3.1 Modes of excitation

For a two dimensional earth, i.e. one in which the resistivity in the strike direction differs from the resistivity in the orthogonal direction, the electric field in either of these principal directions may be related to the magnetic fields in both directions. Then a tensor relationship between electric and magnetic fields must be used as illustrated in Figure 3. The mode of excitation wherein the electric vector is oriented parallel to strike, i.e. $E_{\parallel}$ is referred to as the TE mode whereas when the electric vector is perpendicular to strike, i.e. $E_{\perp}$, the TM mode is excited. Usually both modes are excited simultaneously.

The electric and magnetic fields for TE and TM mode excitation of a conductive 2D body are shown schematically in Figure 4. For the TE mode, where the electric field is parallel to the body, the anomalous normalized

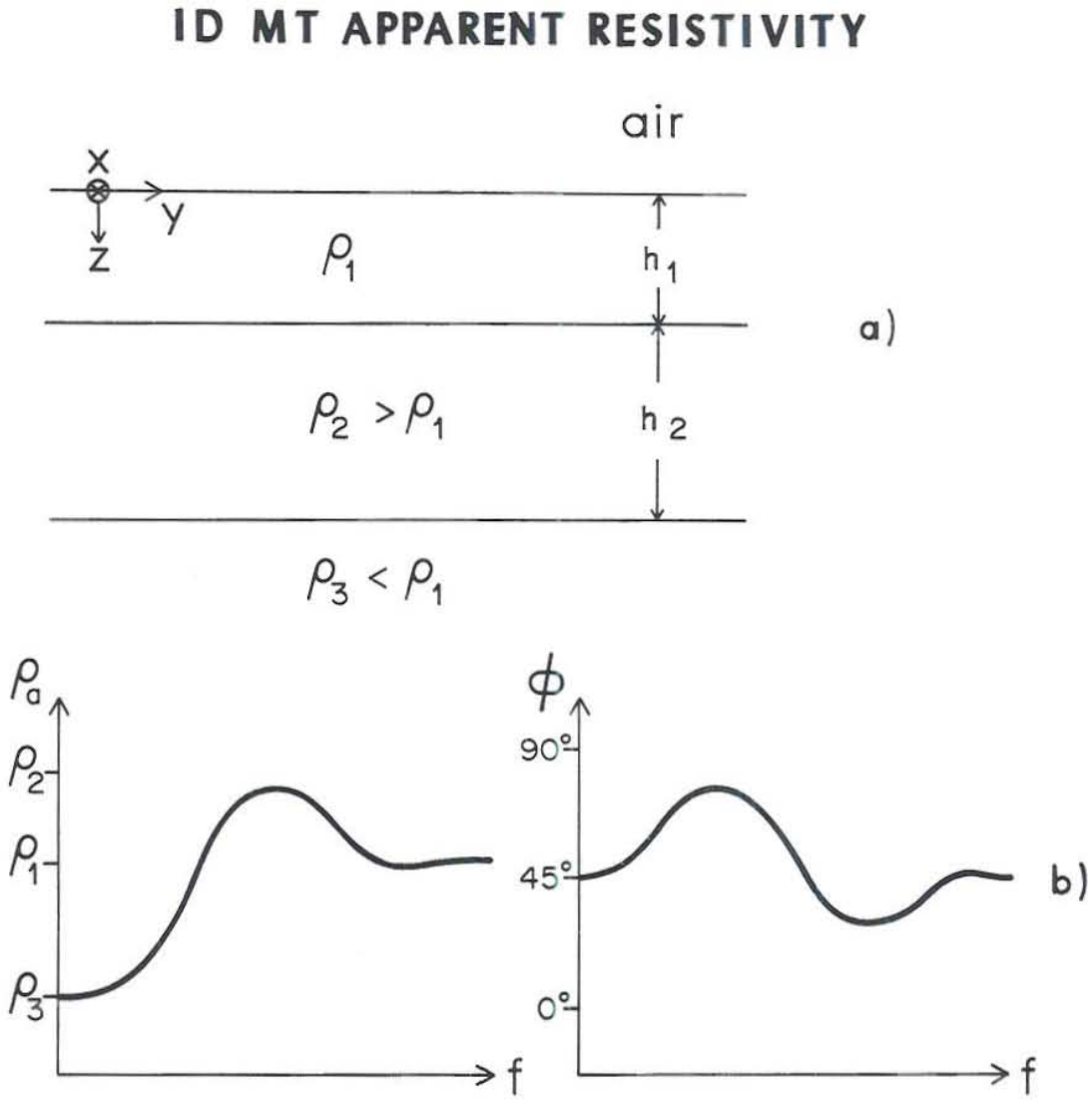

Figure 2. Typical model, apparent resistivity, and impedance phase for a layered (1D) earth.

Figure 3. Model, modes of excitation, and formulation for a 2D earth.

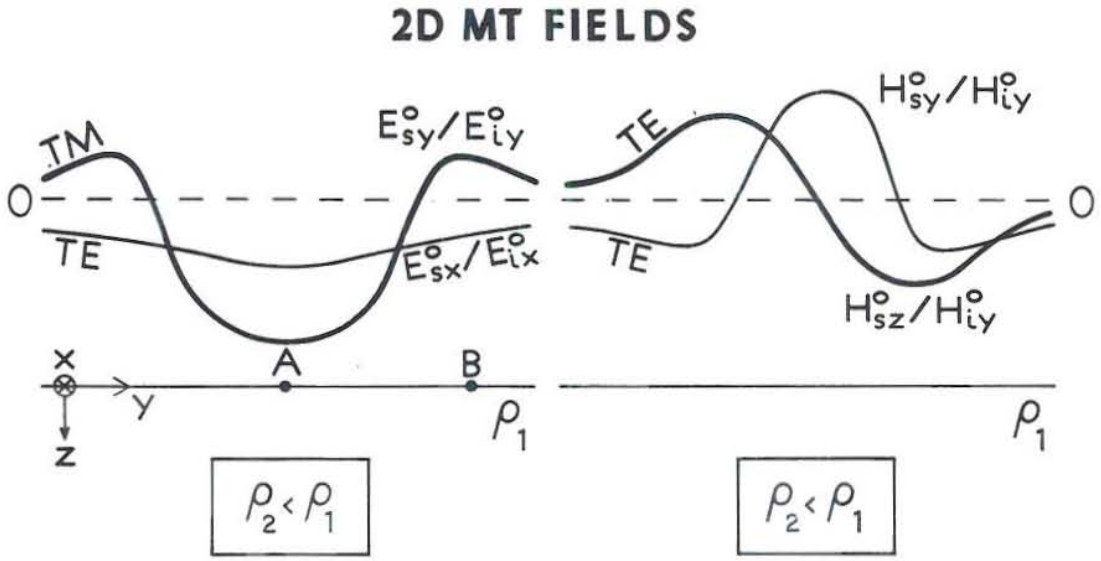

Figure 4. Illustrative behavior of electric and magnetic fields over a 2D body in a homogeneous half-space.

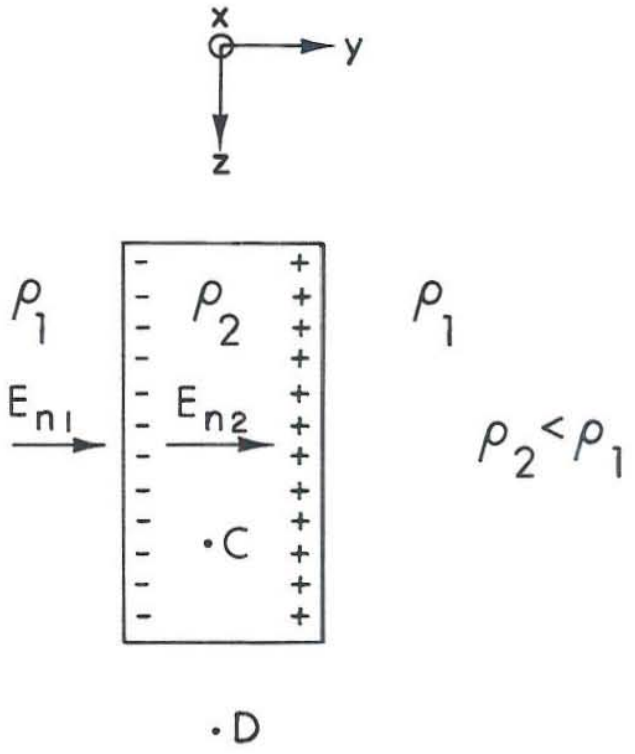

Figure 5. Illustration of surface charges at boundaries, due to an electric field excitation.

electric field $\frac{E^0_{sx}}{E^0_{ix}}$ varies from its normal value well off to the side of the body to low values over the body. The corresponding TE mode magnetic field $\frac{H^0_{sz}}{H^0_{iy}}$ reverses over the body while $\frac{H^0_{sy}}{H^0_{iy}}$ is negative outside the body and positive over the body, as appropriate for a line source of current along the axis of the body. These secondary induced fields become vanishingly small as frequencies approach zero (Wannamaker et al., 1982). For the TM mode one observes in Figure 4 that the normalized anomalous electric field $\frac{E^0_{sy}}{E^0_{si}}$ is positive outside the body and negative over it. This characteristic of the TM mode is indicative of dipolar fields, does not vanish as frequency falls, and requires some explanation.

2.2.3.2 Surface charge and current channeling

The explanation for this dipolar behavior lies in the existence of a surface charge density ρ_s. If we start with the equation of continuity in the frequency domain

$$\nabla \cdot \vec{J} = -i_\omega \rho_s \tag{9}$$

With the aid of Ohm's Law we convert (9) to

$$\nabla \cdot (\sigma \vec{E}) = -i_\omega \rho_s \ , \tag{10}$$

or

$$(\nabla\sigma) \cdot \vec{E} + \sigma\nabla \cdot \vec{E} = -i_\omega \rho_s \ . \tag{11}$$

Next we substitute the Maxwell equation

$$\nabla \cdot \vec{E} = \rho_s/\varepsilon_0 \tag{12}$$

in (11) to yield

$$(\nabla\sigma) \cdot \vec{E} + \frac{\sigma}{\varepsilon_o} \rho_s = -i\omega\rho_s \quad . \tag{13}$$

Upon rearrangement (13) becomes

$$\rho_s = -\frac{\varepsilon_o}{\sigma + i\varepsilon_o\omega} (\nabla\sigma) \cdot \vec{E} \tag{14}$$

If displacement currents are neglected, i.e. $\sigma >> \varepsilon_o\omega$, we have

$$\rho_s = -\frac{\varepsilon_o}{\sigma} (\nabla\sigma) \cdot \vec{E} \tag{15}$$

For the configuration of Figure 5, equation (15) becomes

$$\rho_s = \varepsilon_o \frac{\sigma_1 - \sigma_2}{\sigma_1} E_{n2}. \tag{16}$$

Although the surface charge density ρ_s is small because $\varepsilon_o \sim 10^{-11}$ farad/m, its electric field is large because in a whole space (at low frequencies) it is given by

$$\vec{E} = -\nabla V = -\nabla \int_s \frac{\rho_s}{4\pi\varepsilon_o |\vec{r}|} ds = -\nabla \int_s \frac{1}{4\pi} \frac{\sigma_1 - \sigma_2}{\sigma_1 |\vec{r}|} E_{n2} ds = -\nabla \int_s \frac{1}{4\pi} \frac{\rho_2 - \rho_1}{\rho_2 |\vec{r}|} E_{n2} ds. \tag{17}$$

Note that this electric field is independent of frequency at low frequencies. For MT, the E-field response is predominantly dipolar, although higher order multipoles may be important at higher frequencies (see Stratton, 1941, p. 563-573). The electric field at C in Figure 5 due to this polarization is in the direction of the external electric field E_{n1} while the electric field at D due to the polarization is in the opposite direction to E_{n1}. Upon addition of the incident field, this gives the appearance of currents in the external medium being deflected into the more conducting medium. This phenomenon is referred to as current channeling. If the two dimensional body of Figure 5 was more resistive than its surroundings, i.e. ρ_2

$> \rho_1$, then the currents would be deflected away from the body as equation (17) would predict. Current channeling as opposed to local induction of eddy currents is illustrated in Figure 6. The two effects are superimposed when an electromagnetic field impinges on an earth in which a conductive inhomogeneity exists.

Figure 7 contains plots of apparent resistivity and impedance phase versus frequency for points A and B of Figure 4. The apparent resistivity and impedance phase for both of points A and B at the highest frequencies will be that for a homogeneous half-space of resistivity ρ_1 since the skin depth δ_1

$$\delta_1 = \frac{2}{\sqrt{\omega\mu\sigma_1}} \sim 500 \sqrt{\frac{\rho_1}{f}} \qquad (18)$$

in the half-space is so small that little energy reaches the 2D body. On the other hand, at the lowest frequencies the 2D body will be transparent to the downward traveling electromagnetic wave, since the TE mode does not involve surface charges and current gathering, so that once again the apparent resistivity and impedance phase at both A and B will be that for a homogeneous half-space of resistivity ρ_1 (Wannamaker et al., 1982). Between the low and high frequency extremes, the TE mode apparent resistivity, ρ_{TE}, drops below ρ_1 at A and B since the 2D body is of resistivity lower than ρ_1 and its effect is observed. The behavior of the impedance phase ϕ_{TE} is then somewhat predictable from ρ_{TE} if equation (8) is loosely applied.

On the other hand, ρ_{TM} at point A starts at ρ_1 at the highest frequency where the waves have not penetrated to the 2D body, but continues to decrease with decreasing frequency until it asymptotes at some value dictated by the current channeling effect. Note that A is located in a region where the total electric field is lower than the incident field as for point D of Figure 5.

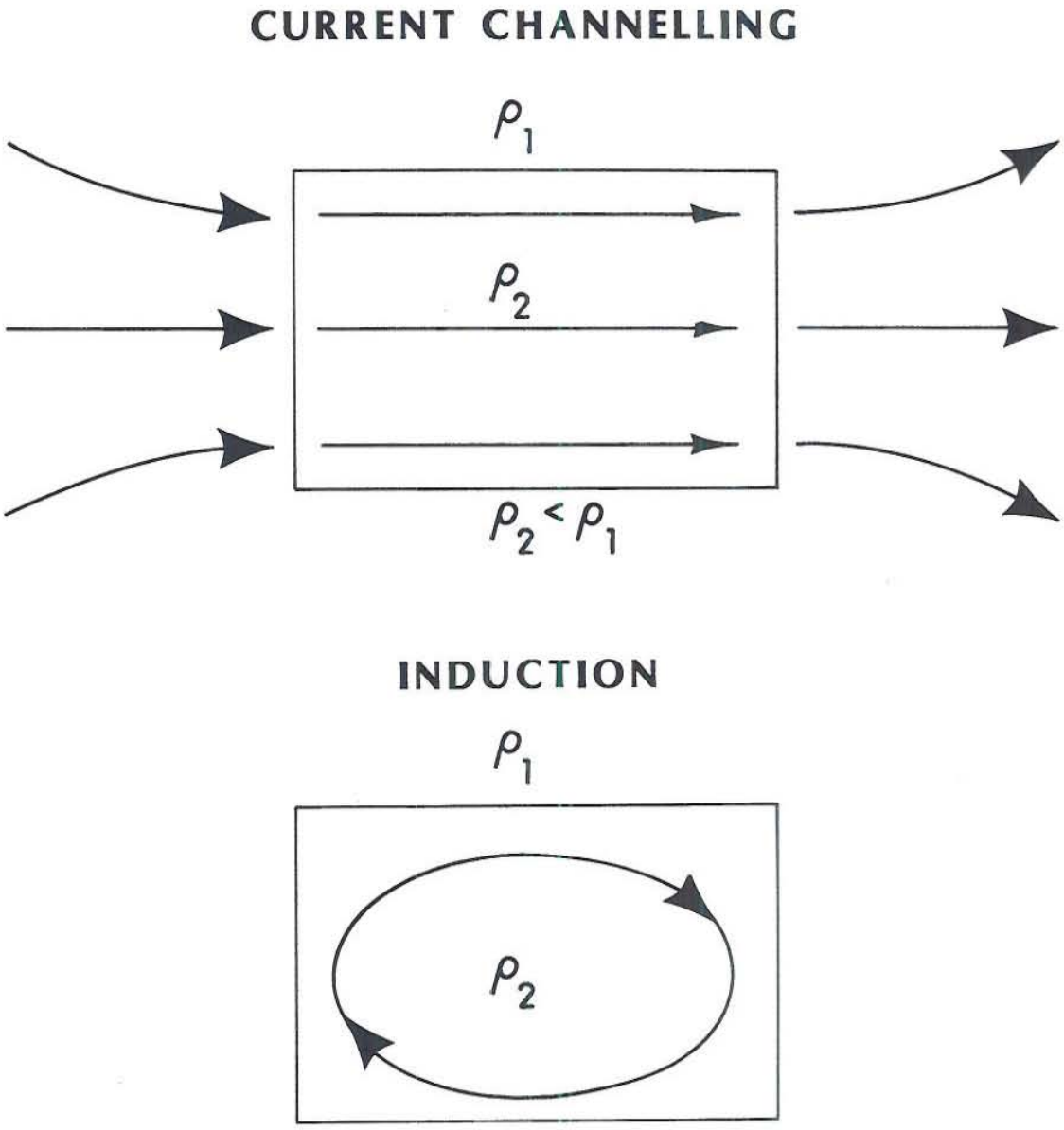

Figure 6. Illustration of conceptual notions of current gathering and local induction.

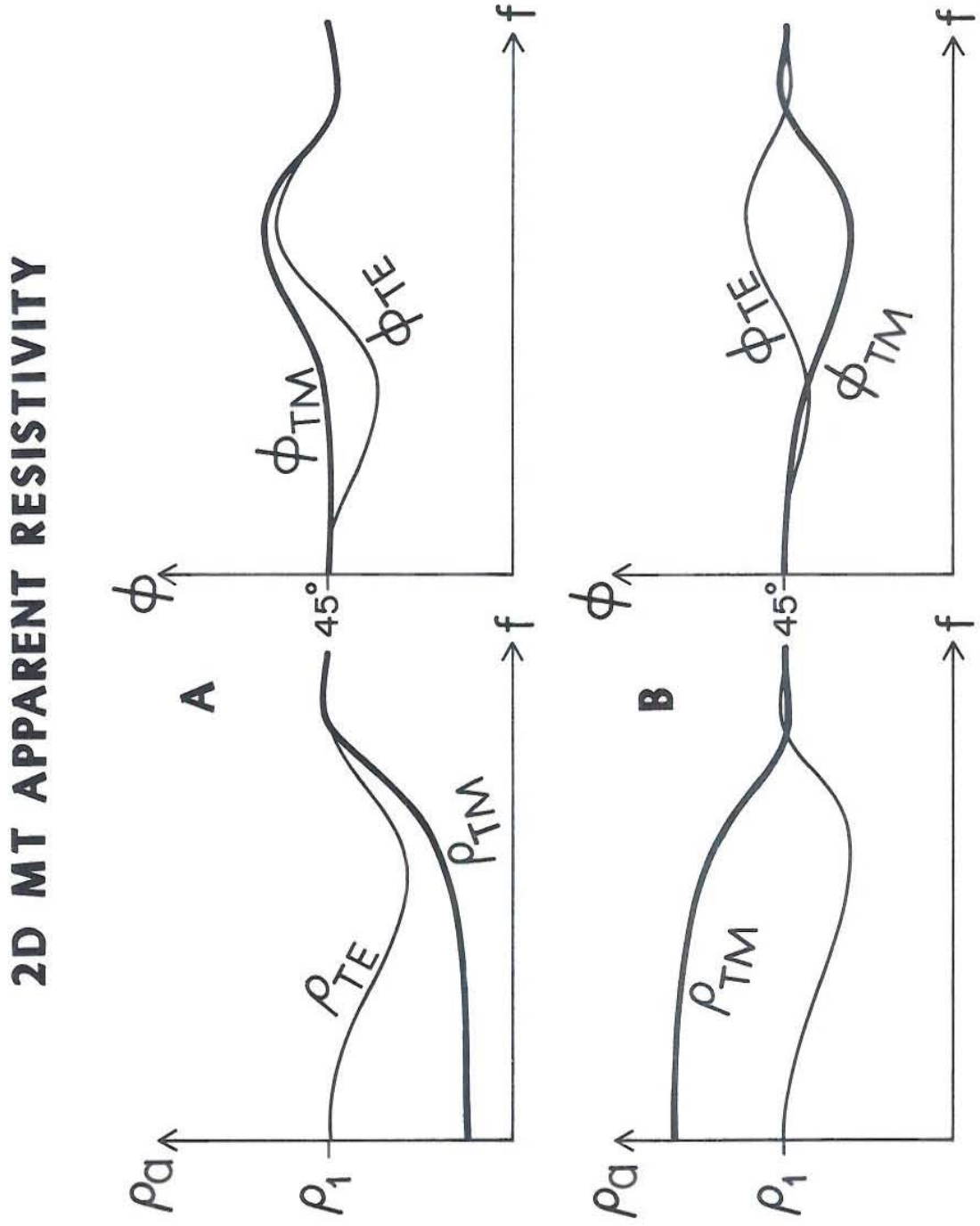

Figure 7. Typical behavior of TE and TM mode apparent resistivities and impedance phases at two points near a 2D body in a homogeneous half-space.

Off to the side of the 2D body, as at B, of Figure 4, the electric field due to the polarization charges add to the incident field. Hence, the apparent resistivity, calculated from an expression of the form

$$\rho_{TM} = 0.2T \left| \frac{E_y}{H_x} \right|^2 \tag{19}$$

will increase with decreasing frequency until a low frequency asymptote has been reached. Once again ϕ_{TM} roughly follows the gradient of ρ_{TM} versus frequency.

2.2.3.3 The impedance tensor

We have seen that there are two basic modes of excitation TE ($E_{\parallel}$) and TM ($E_{\perp}$) as illustrated in Figure 3. In practice we do not know the strike or x direction *a priori* so that our field data is taken in rotated directions which may be at any angle to x and y. Hence we need to have some means of rotating field data into TE and TM modes.

If x is the strike direction, then we write

$$Z_{TE} = \frac{E_x}{H_y} = Z_{xy}, \tag{20}$$

and

$$Z_{TM} = -\frac{E_y}{H_x} = Z_{yx}.$$

The impedance tensor given in Figure 3 becomes, when the fields are aligned parallel and perpendicular to strike,

$$\begin{bmatrix} E_x \\ E_y \end{bmatrix} = \begin{bmatrix} 0 & Z_{xy} \\ Z_{yx} & 0 \end{bmatrix} \cdot \begin{bmatrix} H_x \\ H_y \end{bmatrix}, \tag{21}$$

i.e. $Z_{xx} = Z_{yy} = 0$.

Now let us turn to the field case where the electrical strike direction

is unknown. Then measurements are made in a rotated xy coordinate system of Figure 8.

The x'y' coordinate system is aligned with the strike so that we have

$$E_x' = Z_{TE} H_y' \ , \tag{22}$$

and

$$E_y' = -Z_{TM} H_x' \ . \tag{23}$$

In the xy coordinate system rotated by an angle Θ,

$$E_x = E_x' \cos\Theta + E_y' \sin\Theta \ , \tag{24}$$

$$E_y = -E_x' \sin\Theta + E_y' \cos\Theta \ , \tag{25}$$

$$H_x = H_x' \cos\Theta + H_y' \sin\Theta \ , \tag{26}$$

and

$$H_y = -H_x' \sin\Theta + H_y' \cos\Theta \ . \tag{27}$$

Substituting (22) and (23) in (24) we obtain

$$E_x = Z_{TE} H_y' \cos\Theta - Z_{TM} H_x' \sin\Theta \ . \tag{28}$$

We can write, for the reverse coordinate transformation,

$$H_x' = H_x \cos\Theta - H_y \sin\Theta \ , \tag{29}$$

and

$$H_y' = H_x \sin\Theta + H_y \cos\Theta \ . \tag{30}$$

When (29) and (30) are substituted in (28) there results

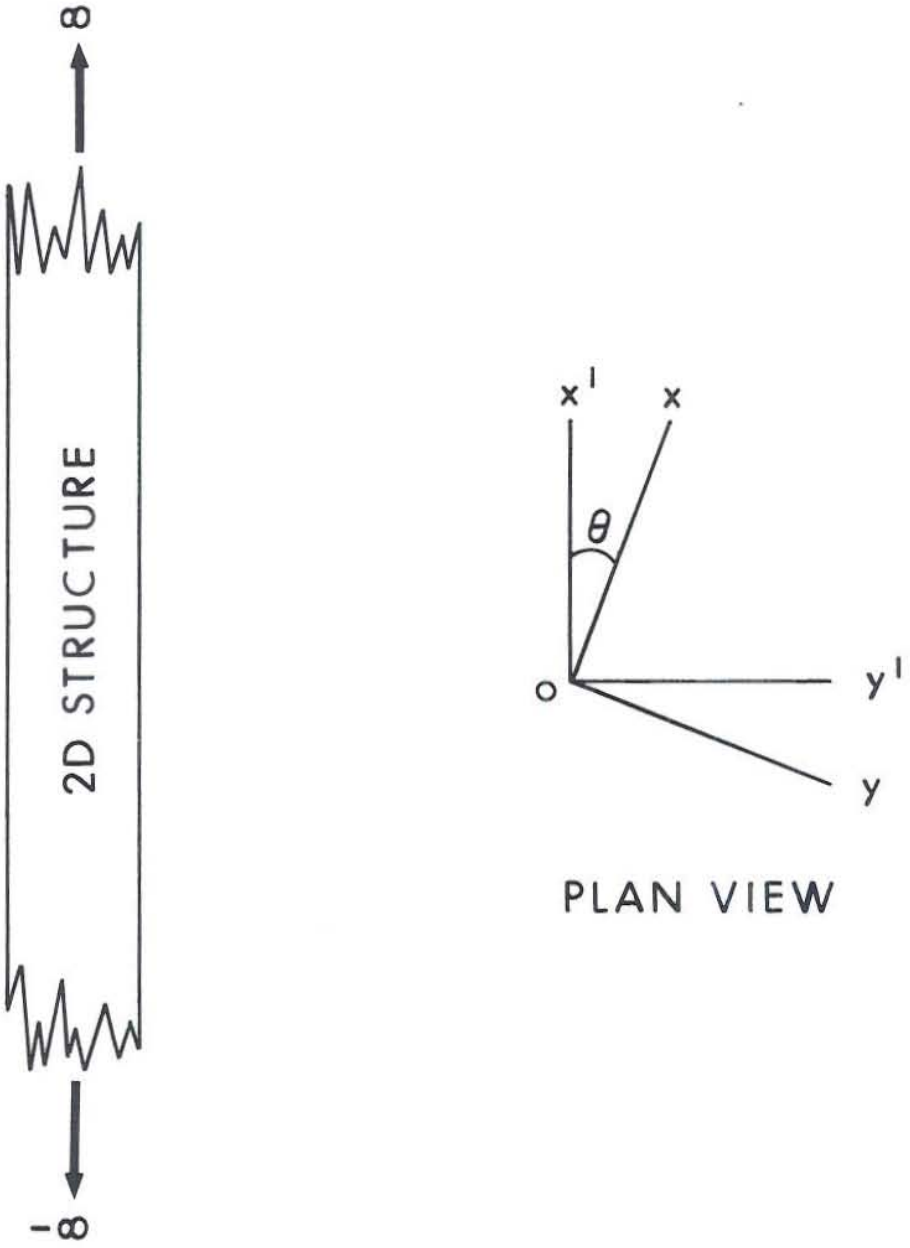

Figure 8. Plan view of measuring axes (x,y) and symmetry axes (x',y') for an MT survey over 2D body in a homogeneous half-space.

$$E_x = Z_{TE} (H_x \sin\theta + H_y \cos\theta) \cos\theta$$

$$-Z_{TM} (H_x \cos\theta - H_y \sin\theta) \sin\theta$$

$$= H_x (Z_{TE} - Z_{TM}) \sin\theta \cos\theta + H_y (Z_{TE} \cos^2\theta + Z_{TM} \sin^2\theta)$$

$$= H_x \left(\frac{Z_{TE} - Z_{TM}}{2}\right) \sin 2\theta + H_y [Z_{TE} - Z_{TM}) \sin^2\theta] \qquad (31)$$

$$= H_x \left(\frac{Z_{TE} - Z_{TM}}{2}\right) \sin 2\theta + H_y \left[\left(\frac{Z_{TE} + Z_{TM}}{2}\right) + \left(\frac{Z_{TE} - Z_{TM}}{2}\right) \cos 2\theta\right],$$

where use has been made of the trigonometric identities

$$2 \sin\theta \cos\theta = \sin 2\theta,$$

$$2 \sin^2\theta = 1 - \cos 2\theta,$$

and

$$2 \cos^2\theta = 1 + \cos 2\theta.$$

Hence, if we write, in the rotated coordinate system,

$$E_x = Z_{xx} H_x + Z_{xy} H_y , \qquad (32)$$

then by comparing (31) with (32) we get

$$Z_{xx} = \left(\frac{Z_{TE} - Z_{TM}}{2}\right) \sin 2\theta , \qquad (33)$$

and

$$Z_{xy} = \left(\frac{Z_{TE} + Z_{TM}}{2}\right) + \left(\frac{Z_{TE} - Z_{TM}}{2}\right) \cos 2\theta . \qquad (34)$$

Similarly we get

$$Z_{yx} = -\left(\frac{Z_{TE} + Z_{TM}}{2}\right) + \left(\frac{Z_{TE} - Z_{TM}}{2}\right) \cos 2\theta , \qquad (35)$$

and

$$Z_{yy} = \frac{Z_{TM} - Z_{TE}}{2} \sin 2\Theta \quad . \tag{36}$$

The important conclusion to be drawn from (33) through (36) is that the impedance elements obtained in the field coordinate system are complicated combinations of TE and TM mode impedance elements.

From (33) and (36) we find that

$$Z_{xx} = -Z_{yy} \ , \tag{37}$$

while from (33) and (34)

$$Z_{xy} - Z_{yx} = Z_{TM} + Z_{TE} . \tag{38}$$

Both (37) and (38) are independent of the angle Θ.

If the earth is 2D then one measures orthogonal electric and magnetic fields in the arbitrary field coordinate system and calculate the impedances Z'_{xx}, Z'_{xy}, Z'_{yx}, and Z'_{yy}. From these data one would then attempt to find a direction in which $Z_{xx} = Z_{yy} = 0$ and then resulting $Z_{xy} = Z_{TE}$ and $Z_{yx} = -Z_{TM}$. The directions at which this occurs, for clockwise rotation, are given by Vozoff (1972) as

$$\tan (4\Theta_0) = \frac{(Z'_{xx} - Z'_{yy})(Z'_{xy} + Z'_{yx}) + (Z'_{xx} + Z'_{yy})(Z'_{xy} - Z'_{yx})}{|Z'_{xx} - Z'_{yy}|^2 - |Z'_{xy} + Z'_{yx}|^2} . \tag{39}$$

Such principal directions occur every 90°, so that the strike direction cannot be distinguished from the dip axis using the impedance alone.

This ambiguity is removed using the *tipper* T, defined as

$$T = [|A|^2 + |B|^2]^{1/2} \quad , \tag{40}$$

where

$$H_z = AH_x + BH_y \, . \tag{41}$$

For the TM mode ($E_\perp$) mode, no H_z results, so that the direction x which results in A reducing to zero is strike.

2.2.4 Formulation for a three dimensional earth

Figure 9 illustrates that for an equidimensional 3D object, mode identification is no longer possible. All components of secondary field are induced by any orientation of the incident field. Furthermore, current channeling takes place for any orientation of the incident field.

Sims and Bostick (1969) show that the usual impedance tensor of Figure 3 is valid for 3D models. In Figure 10 we illustrate the 3D body, the measuring axes xy, and the symmetry axes x'y'. The electric and magnetic fields are related not by (20), but by the following equations

$$E'_x = Z'_{xx} H'_x + Z'_{xy} H'_y \quad , \tag{42}$$

and

$$E'_y = Z'_{yx} H'_x + Z'_{yy} H'_y \, , \tag{43}$$

in which the impedance elements Z_{ij} are functions of θ as are the fields.

The electric field in the x direction is

$$E_x = E'_x \cos\theta + E'_y \sin\theta. \tag{44}$$

When (42) and (43) are substituted in (44) there results

Figure 9. Illustration of impossibility of mode identification for an equidimensional 3D body.

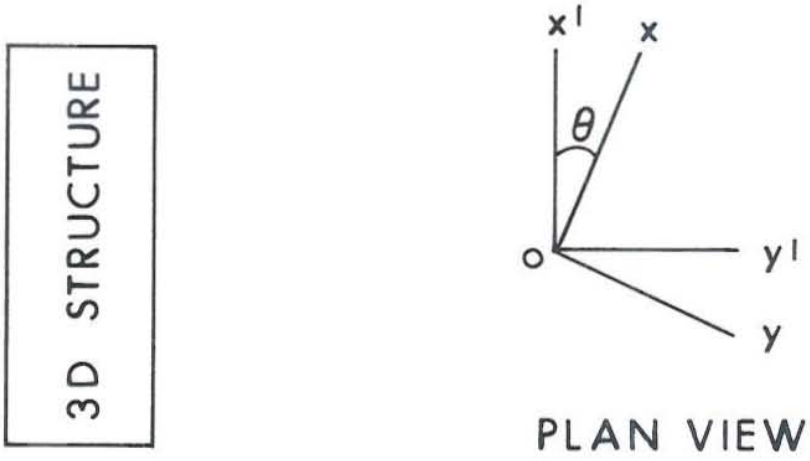

Figure 10. Plan view of measuring axes (x,y) and symmetry axes (x',y') for an MT survey over a 3D body in a homogeneous half-space.

$$E_x = (Z'_{xx} H'_x + Z'_{xy} H'_y) \cos\Theta + (Z'_{yx} H'_x + Z'_{yy} H'_y) \sin\Theta$$

$$= (Z'_{xx} \cos\Theta + Z'_{yx} \sin\Theta) H'_x + (Z'_{xy} \cos\Theta + Z'_{yy} \sin\Theta) H'_y . \quad (45)$$

Then we substitute H'_x and H'_y according to (29) and (30), respectively, to obtain

$$E_x = (Z'_{xx} \cos\Theta + Z'_{yx} \sin\Theta) (H_x \cos\Theta - H_y \sin\Theta)$$

$$+ (Z'_{xy} \cos\Theta + Z'_{yy} \sin\Theta) (H_x \sin\Theta + H_y \cos\Theta). \quad (46)$$

When rearranged, (46) yields

$$E_x = [Z'_{xx} \cos^2\Theta + Z'_{yy} \sin^2\Theta + (Z'_{yx} + Z'_{xy}) \sin\Theta \cos\Theta] H_x$$

$$+ [Z'_{xy} \cos^2\Theta - Z'_{yx} \sin^2\Theta + (Z'_{yy} - Z'_{xx}) \sin\Theta \cos\Theta] H_y . \quad (47)$$

In the field coordinate system xy we expect to observe that

$$E_x = Z_{xx} H_x + Z_{xy} H_y , \quad (48)$$

so that we identify Z_{xx} and Z_{yy} as follows

$$Z_{xx} = Z'_{xx} \cos^2\Theta + Z'_{yy} \sin^2\Theta + (Z'_{xy} + Z'_{yx}) \sin\Theta \cos\Theta, \quad (49)$$

and

$$Z_{xy} = Z'_{xy} \cos^2\Theta - Z'_{yx} \sin^2\Theta + (Z'_{yy} - Z'_{xx}) \sin\Theta \cos\Theta. \quad (50)$$

Using the same trigonometric identities as for the 2D case, equations (49) and (50) reduce to

$$Z_{xx} = Z_1 + Z_2 \cos 2\Theta + Z_3 \sin 2\Theta, \quad (51)$$

and

$$Z_{xy} = Z_4 + Z_3 \cos 2\theta - Z_2 \sin 2\theta. \tag{52}$$

Similarly, we find

$$Z_{yx} = -Z_4 + Z_3 \cos 2\theta - Z_2 \sin 2\theta, \tag{53}$$

and

$$Z_{yy} = Z_1 - Z_2 \cos 2\theta - Z_3 \sin 2\theta \ . \tag{54}$$

In (51) through (54) we have shortened the notation by using the following definitions

$$Z_1 = \frac{Z'_{xx} + Z'_{yy}}{2} \ , \qquad Z_2 = \frac{Z'_{xx} - Z'_{yy}}{2} \ , \tag{55}$$

$$Z_3 = \frac{Z'_{xy} + Z'_{yx}}{2} \ , \qquad \text{and} \qquad Z_4 = \frac{Z'_{xy} - Z'_{yx}}{2} \ . \tag{56}$$

From (51) and (54) we observe that

$$\frac{Z_{xx} + Z_{yy}}{2} = Z_1 \ , \tag{57}$$

while from (52) and (53) we observe that

$$\frac{Z_{xy} - Z_{yx}}{2} = Z_4 \ . \tag{58}$$

Note from a comparison of (55) with (57) and (56) with (58) that Z_1 and Z_4 are invariant under rotation. In the 2-D case, equation (37), we found that $Z_1 = 0$. Hence the *skewness* S has been introduced as a measure of three-dimensionality. S is defined by

$$S = \frac{|Z_1|}{|Z_4|} = \frac{|Z'_{xx} - Z'_{yy}|}{|Z'_{xy} - Z'_{yx}|} \ . \tag{59}$$

If S is large, then three-dimensionality is indicated. However, if S is small, it is not easy to deduce whether or not the earth is 2-D or 3-D.

It is clear from (57) that the elements Z_{xx} and Z_{yy} of the impedance tensor do not become zero in the presence of a 3D body except along any axis of symmetry. However, for a 3D body, principal axes generally may be defined where Z_{xx} and Z_{yy} are minimized. Hence it is customary to estimate an approximate strike direction Θ_0 and to estimate the principal impedances $Z_{xy} = Z_{TE}$ and $Z_{yx} = Z_{TM}$ in such principal directions. Several methods have been used to find the angle Θ_0 between the measuring axes and the principal axes. For example one can maximize $|Z_{xy}|^2 + |Z_{yx}|^2$, minimize $|Z_{xx}|^2 + |Z_{yy}|^2$, maximize $|Z_{xy}|$ or $|Z_{yx}|$, minimize $|Z_{xx}|$ or $|Z_{yy}|$, maximize $|Z_{xy} + Z_{yx}|$ and so on. Each procedure will give the strike direction if the earth is two dimensional. When the earth is three-dimensional these methods do not give the same results. The most common method used is that of maximizing the absolute value of the sum of the off-diagonal elements, i.e. maximize $|Z_{xy} + Z_{yx}|$. This is done analytically (Swift, 1967; Sims and Bostick, 1969).

As for the case of a 2D structure, principal directions of the impedance occur every 90°. Defining TE and TM modes requires that this 90° ambiguity be removed. This can be accomplished precisely for a 2D structure using tipper strike since H_z is correlated with the horizontal magnetic field perpendicular to the strike. A unique tipper strike is possible to define for 3D bodies as well, with the principal impedance closest to this strike being assigned to the TE mode. Principal apparent resistivities follow as

$$\rho'_{xy} = 0.2T\,|Z'_{xy}(\Theta_0)|^2 \qquad \text{(TE mode)} \tag{60}$$

and

$$\rho'_{yx} = 0.2T\,|Z'_{yx}(\Theta_0)|^2 \qquad \text{(TM mode)} \tag{61}$$

with impedance phase derived directly from Z'_{xy} and Z'_{yx}. Tipper strike possesses the additional advantage that it is relatively insensitive to near-surface geological noise (Wannamaker et al., 1980, 1982). This procedure does not allow necessarily, however, that 2D algorithms can be applied routinely to principal apparent resistivities and impedance phases gathered over 3D structures.

The basic behavior of apparent resistivities ρ_{xy} and ρ_{yx} and impedance phase ϕ_{xy} and ϕ_{yx}, at points A and B over the 3D body in a half-space, where the x and y coordinates of the MT quantities pertain to those drawn in Figure 11, has been plotted in Figure 12. At point A, note that ρ_{xy} and ρ_{yx} fall as frequency falls until they asymptote to some low-frequency limit somewhere below ρ_1. Regardless of the orientation of the inducing electric field, some boundary polarization charge will exist. This charge creates qualitatively a dipolar electric field anomaly over the body, which resembles that of the TM mode of a 2D body. At low frequencies current-gathering is by far the dominant factor in determining both ρ_{xy} and ρ_{yx}.

The character of the impedance phases ϕ_{xy} and ϕ_{yx}, at point A is complementary to that of ρ_{xy} and ρ_{yx}, although departures from the 2D responses again occur. For the 3D body, ϕ_{xy} and ϕ_{yx} at all but the highest frequencies possess values exceeding 45°. Eventually at low frequencies, ϕ_{xy} and ϕ_{yx} will asymptote to 45°, but will never drop below it. Note that, qualitatively, the apparent resistivities and impedance phases obey Hilbert transform relations as was observed over 2D structures. We again have no proof of this relation for 3D bodies, but it has been our experience with 3D computer simulations and the vast majority of field observations that in

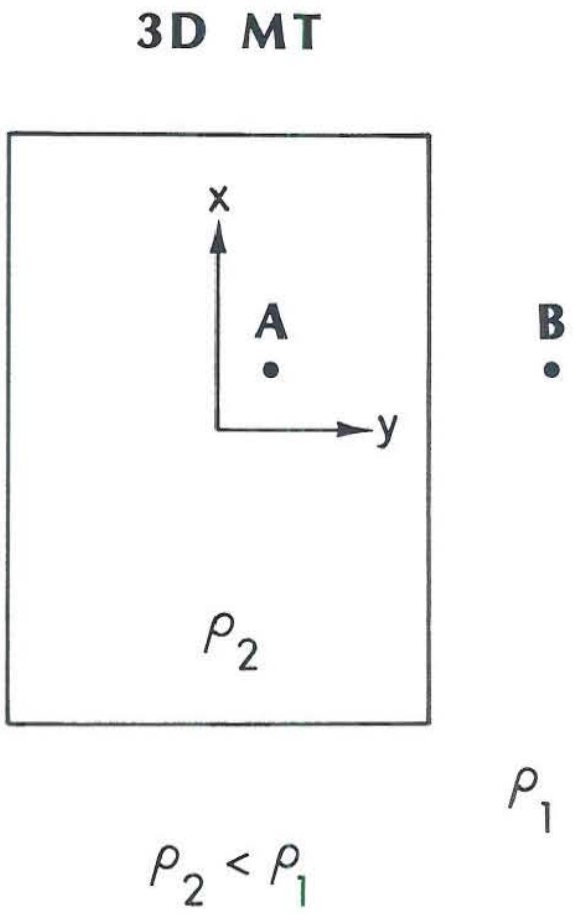

Figure 11. Plan map showing location of measuring points A and B over a 3D body in homogeneous half-space.

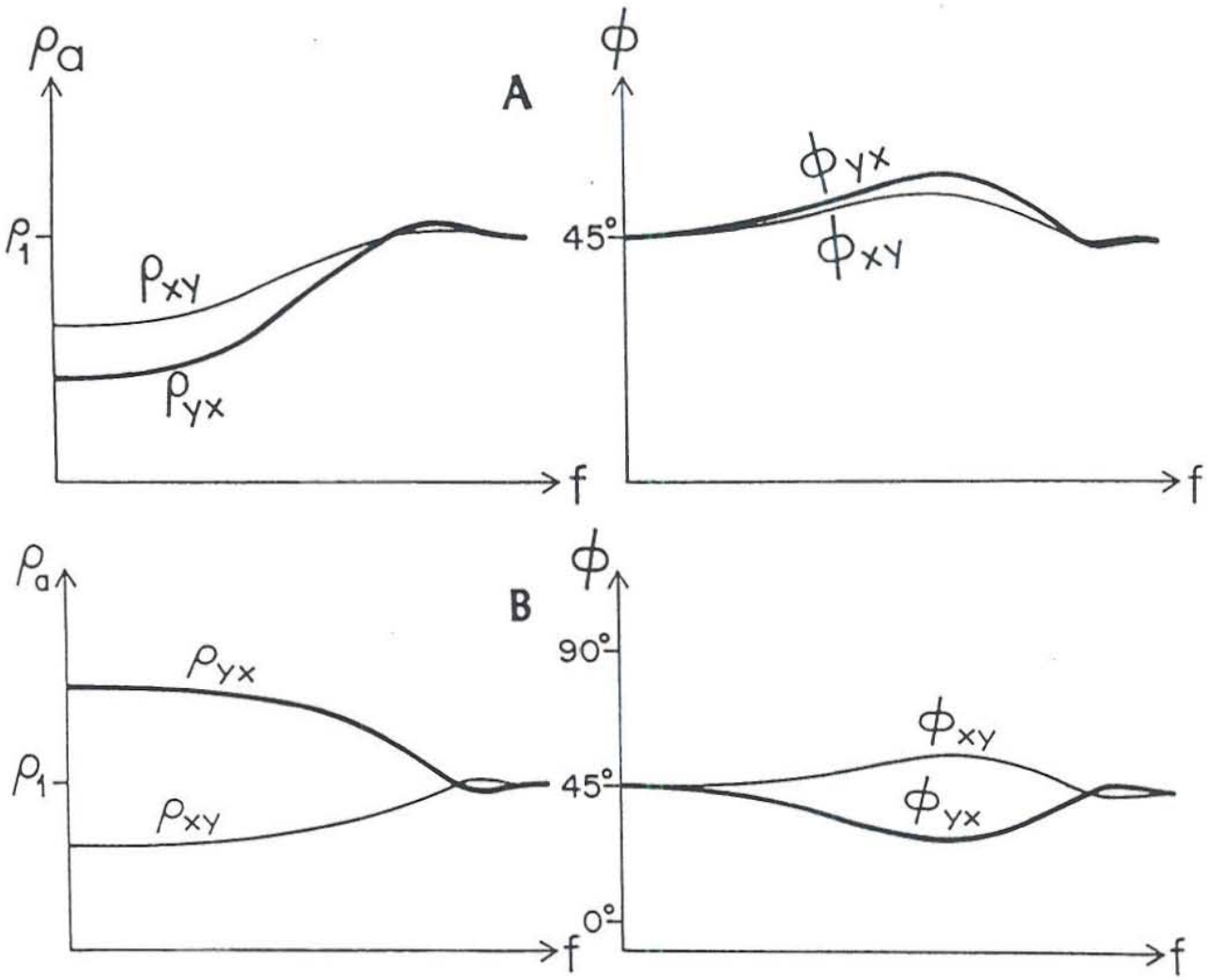

Figure 12. Typical apparent resistivity and impedance phase curves for points A and B of Figure 11.

general this transform relation seems to hold.

In the lower part of Figure 12, the sounding curves correspond to point B outside the 3D prism. Apparent resistivity ρ_{xy} and impedance phase ϕ_{xy} here resemble those at point A, except that they are relatively subdued in their variations.

2.3 Data Acquisition

Vozoff (1972) provides a useful overview of MT data acquisition. Sternberg et al. (1982) present an updated and more detailed description of the subject. Figure 13 shows a schematic representation of the disposition of E and H sensors for MT soundings.

The E fields are detected between orthogonal sets of non-polarizing electrodes. The electrodes are connected by 50 m to 300 m wires to electric field preamplifiers in the recording truck. While Vozoff (1972) early advocated use of large distances ($\geq$ 600 m) between electrodes, Wannamaker (1983) advocates electrode separations as short as possible, consistent with adequate signal. Modern E field preamplifiers are of sufficiently low internal noise that shorter spacings are now possible. One seeks to avoid placing the electrodes of a pair on opposite sides of a surficial resistivity change; the shorter the wire the less likely the electrodes will be on opposite sides. We will refer to this matter again later. The electrodes are either Cd-$CdCl_2$ or Cu-$CuSO_4$ nonpolarizing type. The former are thought to be of slightly lower noise, i.e. chemical drift, but $CdCl_2$ is highly toxic.

The H fields are detected with induction coils or SQUIDS (cryogenic magnetometers). Most modern MT surveys employ two complete MT stations so that the E or the H fields from one may be used as a remote reference for the

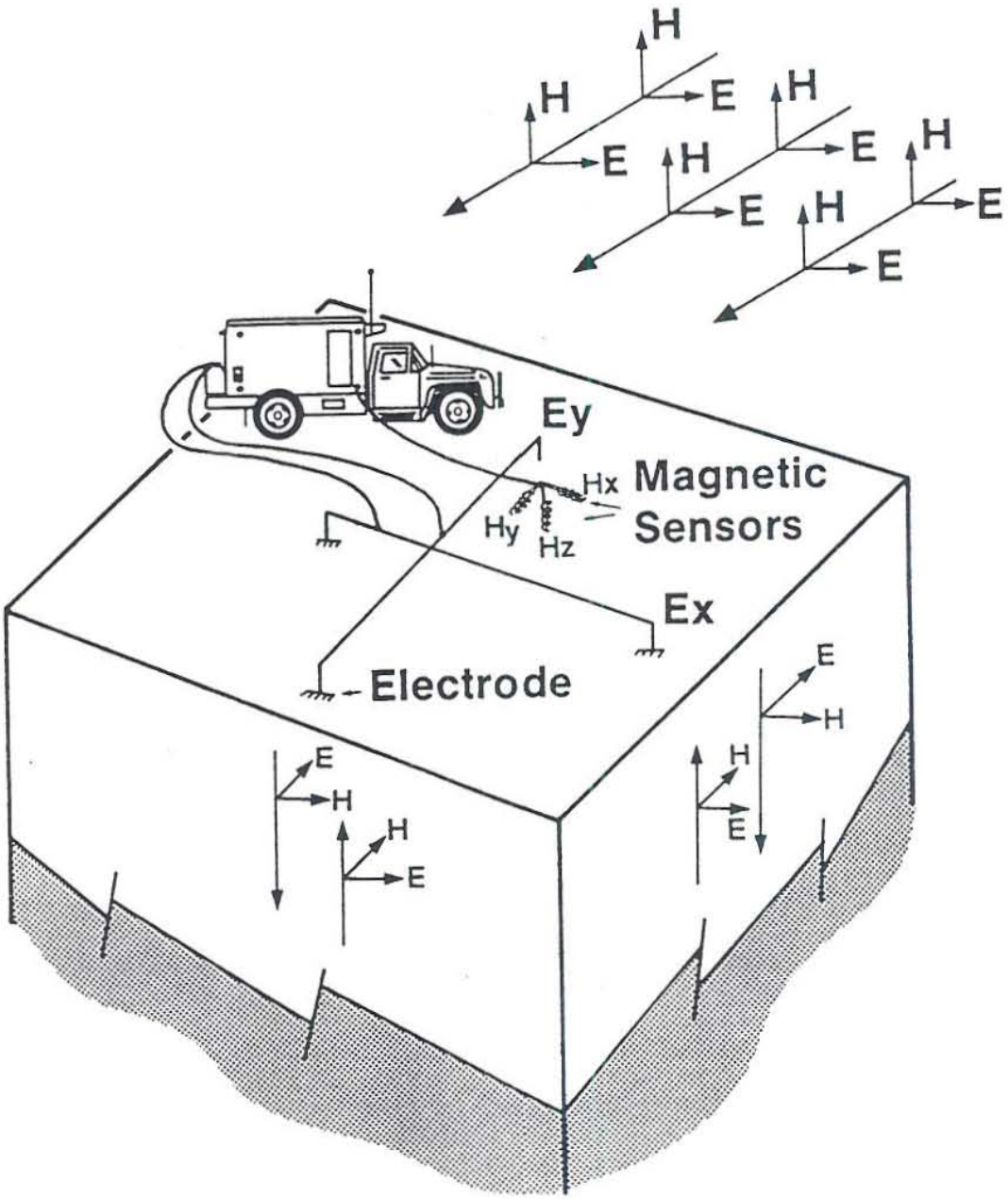

Figure 13. Magnetotelluric sensor deployment in the field (after Sternberg et al., 1982).

other. Gamble et al. (1979a,b) demonstrate that bias in estimates of impedances, derived from MT measurements, may be reduced by use of a remote reference. Stodt (1983) has made a comprehensive review of bias and random errors in MT surveys, and demonstrates that bias removal can be effected, under certain conditions, without resort to remote reference. The use of a remote reference is, nevertheless, to be preferred. This topic will be discussed again later.

Figure 14 shows the system used for MT research by CONOCO, Inc. According to Sternberg et al. (1982),

"The system consists of two data acquistion (or DA) vehicles, each being equipped with the necessary electronics to record three components of the magnetic field with either squid magnetometers or induction coils along with four electric field sensors to record two pairs of orthogonal electric fields. The extra satellite electric field sensor is typically deployed at a distance of a few hundred to a few thousand feet from the main-base electric field sensor. The two DA vehicles may be separated by any distance but are generally 1 to 10 miles apart. Time synchronization between the two vehicles is obtained by signals from WWVB.

A signal analysis (SA) truck is located in the vicinity of both DA trucks and is used to process the MT data. Magnetic tapes are transported from the DA trucks to the SA truck. We have found that the use of telemetry links to transmit the data from one vehicle to another can severely restrict one's flexibility in choosing site locations. Furthermore, transportation of the tapes usually leads to an insignificant delay in comparison with the site occupation time, particularly for a research system. The SA truck is capable of performing all of the MT processing, including remote reference processing,

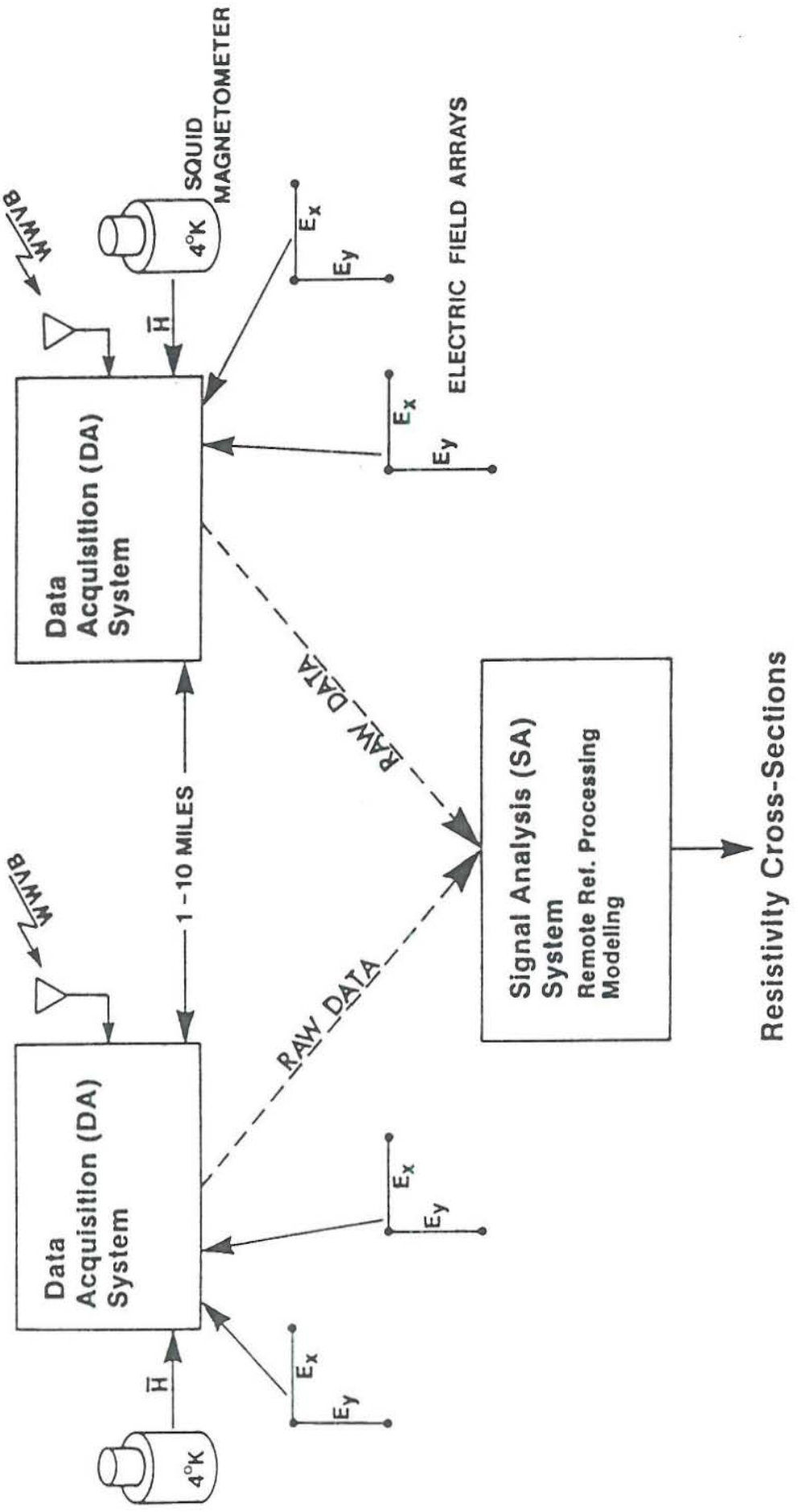

Figure 14. Conoco Research MT system (after Sternberg et al., 1982).

modeling, and generation of final resistivity cross sections."

Figure 15 presents a block diagram overview of a system designed by the Earth Science Laboratory to cope with the wide dynamic range of signal levels encountered in MT/AMT (Stodt, 1983). Output from the electric field sensors is fed into a signal conditioning and line drive box located at the sensors. Line drivers send preamplified and conditioned signals to the recording truck, approximately 100 m from the sensors. At the recording truck, the incoming signals are presented to a line receiver and fed to 4 pole low pass filters with programmable cutoffs for anti-aliasing protection. Optional programmable gain and high pass filter stages are also available at this point. The signal on each channel is then fed to a separate sample and hold amplifier, controlled by a programmable time base. Voltages are then digitized with a minimum of 12 bits of resolution and stored for processing.

Figure 16 presents an expanded block diagram of the electric field and coil receivers of Figure 15. The electric field measurements are processed in the following stages. They are presented to differential pre-amplifiers with RFI filter and transient suppression, then to optional high pass and 60 Hz - 180 Hz notch filters, and finally to programmable gain differential output amplifiers with programmable offset. The coil magnetic field signals are presented to a differential pre-amplifier with RFI filter and transient suppression, and then to optional high pass and 60 Hz-180 Hz notch filters. Line drivers send the conditioned signals to the recording truck. The SQUID magnetic field signals are sent directly to the truck.

Gain in the system is introduced as early as possible to avoid contaminating the measurements with instrument noise. The purpose of the optional high pass and notch filters, and the programmable offset in the

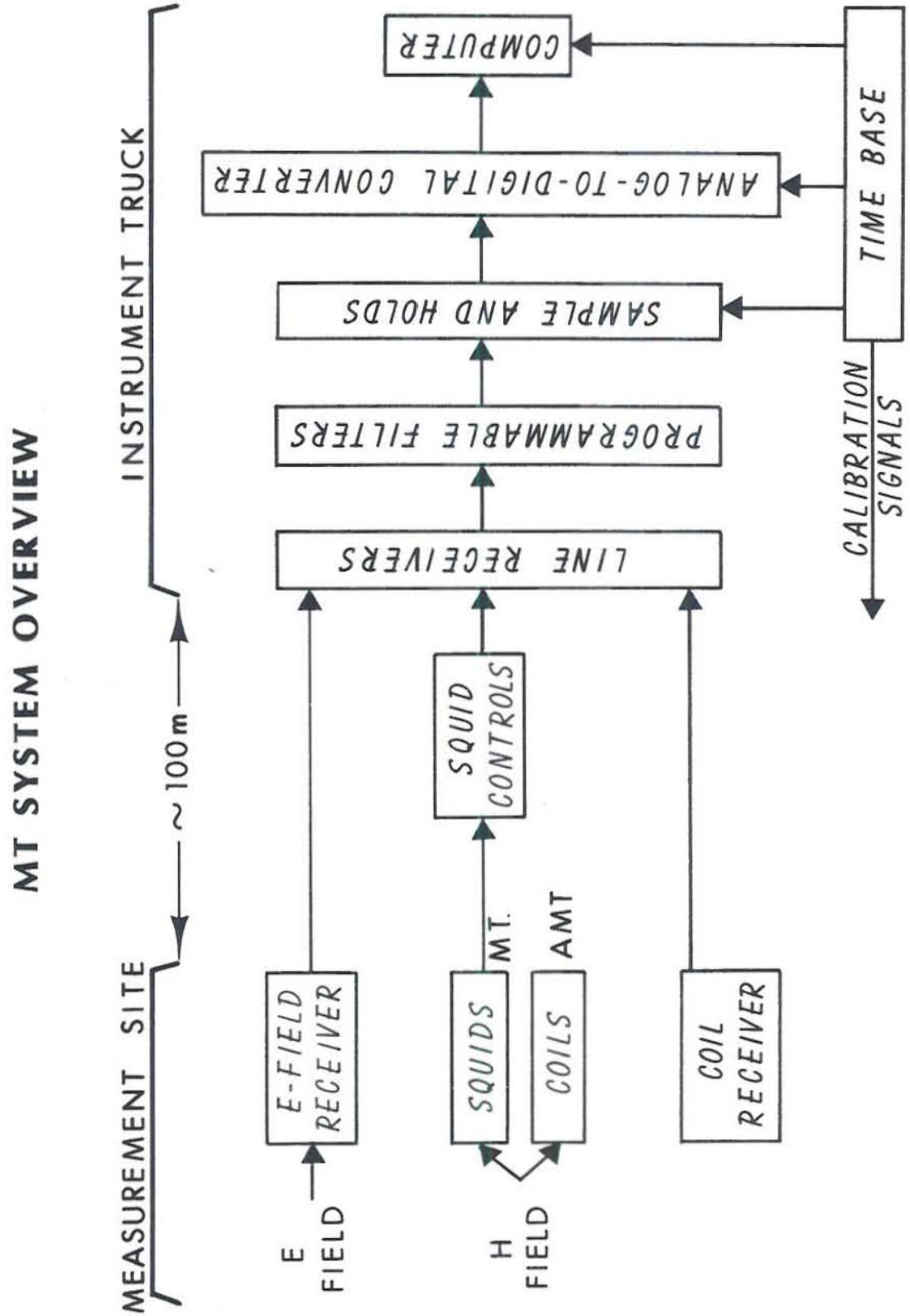

Figure 15. Earth Science Laboratory MT system overview (after Stodt, 1983).

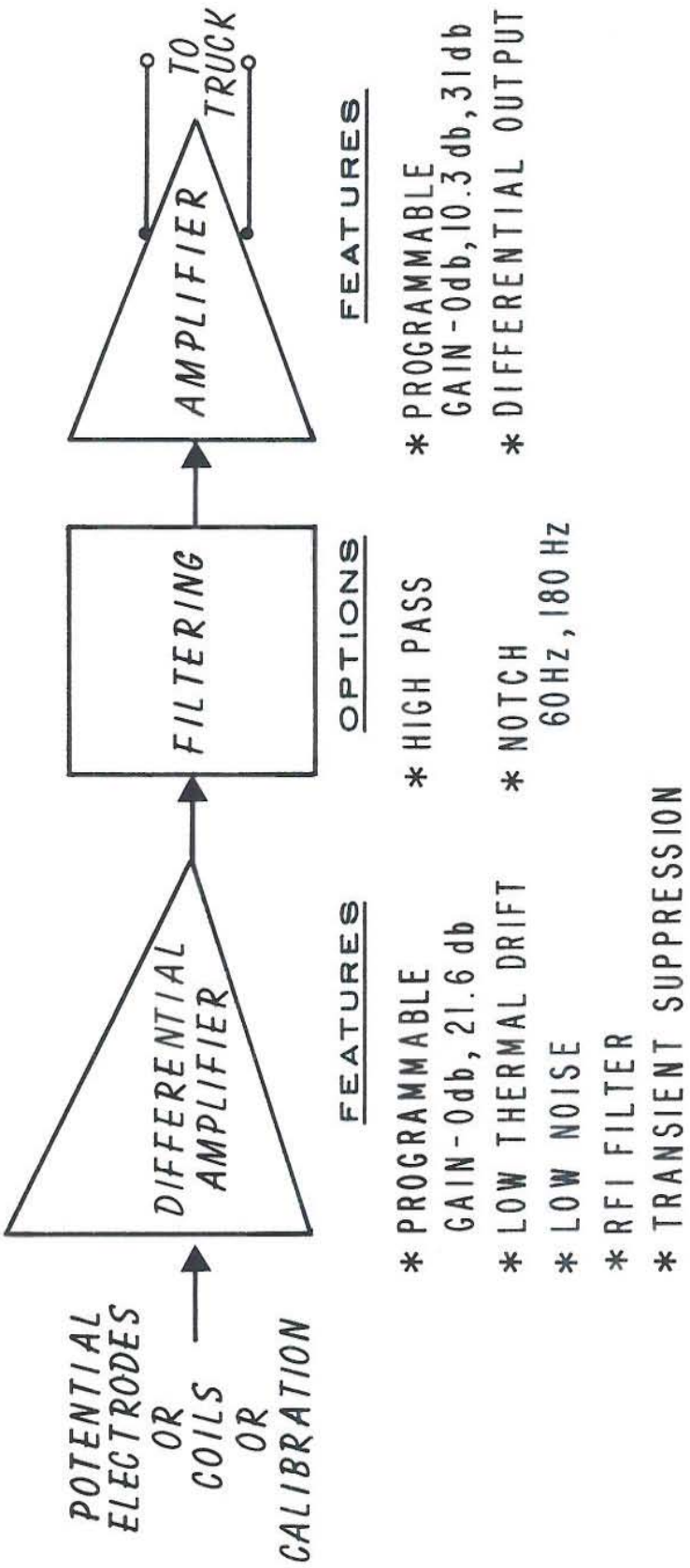

Figure 16. E field and coil H field receivers of Earth Science Laboratory MT system (after Stodt, 1983).

electric field channels, is to tailor the signal so the gain can be turned up without incurring saturations issued by energy at frequencies which are not of interest.

Because of the steeply varying nature of the spectra as a function of frequency, and the nonstationary character of MT signals, dynamic range in the A/D conversion is a problem which requires very careful consideration. Usually 14 bit to 16 bit A to D conversion is required for each of several bands over the 10^{-3} Hz to 100 Hz range of frequencies to be recorded. A premphasis filter is also used to whiten the spectrum and thus reduce the dynamic range requirements.

2.4 Data Processing

Stodt (1983) presents a particularly clean approach to MT data processing from which we quote in part,

"Magnetotelluric (MT) data are obtained as sets of simultaneous measurements of orthogonal electric (E_x, E_y) and magnetic field (H_x, H_y, H_z) components at a given site on the earth's surface. The data sets are Fourier transformed and used to calculate complex transfer functions which relate the field components to each other in the frequency domain at the air-earth interface. When the usual assumptions concerning the plane-wave nature of the source fields are satisfied (e.g. Madden and Nelson, 1964; Swift, 1967), the signal components (subscript s) of the measured fields are related to each other in the following manner:

$$E_{si} = Z_{ix}H_{sx} + Z_{iy}H_{sy}, \quad i = x \text{ or } y, \tag{62}$$

and

$$H_{sx} = T_{zx}H_{sx} + T_{zy}H_{sy} \, . \tag{63}$$

The tensor impedances, Z_{ix} and Z_{iy}, and the tipper functions, T_{zx} and T_{zy}, are functions of frequency and conductivity structure. Equations (62) and (63) can be written in the general form

$$O_{si} = G_{ix}I_{sx} + G_{iy}I_{sy}, \quad i = x, y, \text{ or } z, \tag{64}$$

where, from the viewpoint of linear system theory, G_{ix} and G_{iy} are transfer functions of a dual input, single output linear system through which the inputs, I_{sx} and I_{sy}, are related deterministically to the output, O_{si}. The goal of MT is to deduce the conductivity structure of the earth from the frequency dependent behavior of the impedance and tipper functions.

Generally, MT field measurements consist of signal components of variable amplitude, contaminated by noise. Noise can be defined in general terms as any components of the processed field measurements which do not satisfy the plane-wave impedance relationships given by equations (62) and (63). This general definition includes systematic errors in addition to additive random noise components. Systematic errors are caused by deviations from the assumed model, e.g., errors due to sources which are not plane waves, cultural noise, and analogue or digital processing errors from instrument drift, aliasing, or truncation effects. It is important to distinguish between systematic errors and random noise when developing estimation procedures and error analysis for the impedance and tipper functions.

Impedances and tippers are usually calculated as unweighted least squares estimates. We distinguish between conventional and remote reference impedance and tipper estimates. Conventional estimates are calculated entirely from field measurements obtained at a single base site (e.g. Sims et al, 1971). Two of the horizontal field measurements are used as references with equations

(62) or (63) to compute the estimates. In contrast, remote reference estimates (Goubau, et al, 1978; Gamble et al, 1979a,b) are computed by introducing two reference fields which are measured at a separate location. This is done to avoid correlations between the noises in the base and reference field measurements which introduce bias errors into the estimates."

Details of the derivation of the MT transfer function calculations are given in a number of references, including Swift (1967), Sims and Bostick (1969), Word, Smith, and Bostick (1970), and Vozoff (1972). We shall present a brief summary of salient points.

The impedances Z_{xx}, Z_{xy}, and Z_{yy} are complex, and as noted earlier, are given by

$$E_x = Z_{xx} H_x + Z_{xy} H_y \tag{65}$$

and

$$E_y = Z_{yx} H_x + Z_{yy} H_y \tag{66}$$

We wish to solve for the Z_{ij}.

Since we have more observed field quantities than unknowns, we can utilize this information by multiplying equations (65) and (66) by the complex conjugate of each of the fields,

$$\langle E_x A^* \rangle = Z_{xx} \langle H_x A^* \rangle + Z_{xy} \langle H_y A^* \rangle \tag{67}$$

$$\langle E_x B^* \rangle = Z_{xx} \langle H_x B^* \rangle + Z_{xy} \langle H_y B^* \rangle \tag{68}$$

$$\langle E_y A^* \rangle = Z_{yx} \langle H_x A^* \rangle + Z_{yy} \langle H_y A^* \rangle \tag{69}$$

$$\langle E_y B^* \rangle = Z_{yx} \langle H_x B^* \rangle + Z_{yy} \langle H_y B^* \rangle \tag{70}$$

where A* and B* are the complex conjugates of any two of H_x, H_y, E_x, or E_y and the brackets denote frequency band averages.

This yields more possible equations than unknowns. Since each of the solutions to these equations responds differently to noise on any one of the field components, it is customary to discard some of the solutions and average others to obtain the best estimate.

Solving for the Z_{ij} (e.g., Vozoff, 1972), we obtain:

$$Z_{xx} = \frac{\langle E_x A^* \rangle \langle H_y B^* \rangle - \langle E_x B^* \rangle \langle H_y A^* \rangle}{\langle H_x A^* \rangle \langle H_y B^* \rangle - \langle H_x B^* \rangle \langle H_y A^* \rangle} \quad ; \tag{71}$$

$$Z_{xy} = \frac{\langle E_x A^* \rangle \langle H_x B^* \rangle - \langle E_x B^* \rangle \langle H_x A^* \rangle}{\langle H_y A^* \rangle \langle H_x B^* \rangle - \langle H_y B^* \rangle \langle H_x A^* \rangle} \quad ; \tag{72}$$

$$Z_{yx} = \frac{\langle E_y A^* \rangle \langle H_y B^* \rangle - \langle E_y B^* \rangle \langle H_y A^* \rangle}{\langle H_x A^* \rangle \langle H_y B^* \rangle - \langle H_x B^* \rangle \langle H_y A^* \rangle} \quad ; \tag{73}$$

and

$$Z_{yy} = \frac{\langle E_y A^* \rangle \langle H_x B^* \rangle - \langle E_y B^* \rangle \langle H_x A^* \rangle}{\langle H_y A^* \rangle \langle H_x B^* \rangle - \langle H_y B^* \rangle \langle H_x A^* \rangle} \quad . \tag{74}$$

These are the Z_{ij} estimated in the conventional way. For remote reference estimates of the Z_{ij} we multiply equations (65) and (66) by the magnetic fields (H_{xr} and H_{yr}) at a distant site. Then the following results

$$Z_{xx} = \frac{\overline{(E_x H_{xr}^*}\ \overline{H_y H_{yr}^*} - \overline{E_x H_{yr}^*}\ \overline{H_y H_{xr}^*)}}{\overline{(H_x H_{xr}^*}\ \overline{H_y H_{yr}^*} - \overline{H_x H_{yr}^*}\ \overline{H_y H_{xr}^*)}} \quad , \tag{75}$$

$$Z_{xy} = \frac{(\overline{E_x H_{yr}^*}\ \overline{H_x H_{xr}^*} - \overline{E_x H_{xr}^*}\ \overline{H_x H_{yr}^*})}{(\overline{H_x H_{xr}^*}\ \overline{H_y H_{yr}^*} - \overline{H_x H_{yr}^*}\ \overline{H_y H_{xr}^*})}, \tag{76}$$

$$Z_{yx} = \frac{(\overline{E_y H_{xr}^*}\ \overline{H_y H_{yr}^*} - \overline{E_y H_{yr}^*}\ \overline{H_y H_{xr}^*})}{(\overline{H_x H_{xr}^*}\ \overline{H_y H_{yr}^*} - \overline{H_x H_{yr}^*}\ \overline{H_y H_{xr}^*})}, \tag{77}$$

$$Z_{yy} = \frac{(\overline{E_y H_{yr}^*}\ \overline{H_x H_{xr}^*} - \overline{E_y H_{xr}^*}\ \overline{H_x H_{yr}^*})}{(\overline{H_x H_{xr}^*}\ \overline{H_y H_{yr}^*} - \overline{H_x H_{yr}^*}\ \overline{H_y H_{xr}^*})}, \tag{78}$$

where the bar denotes an average over a frequency window as well as over all data sets.

The expressions in equations (75) through (78) involve only cross powers between the base and the remote stations. If the noise at the base station is not correlated with the noise at the remote reference station and if a sufficient number of data sets are averaged, these impedance estimates will be unbiased by noise. Furthermore, since equations (65) and (66) were multiplied in turn by a single reference field, the values of the impedance elements are independent of the magnitudes and phases of the reference fields and of the resistivity structure at the reference site. Further details on the remote reference processing method are given in Goubau et al. (1978); Gamble et al. (1979a); and Gamble et al. (1979b).

2.5 Data Interpretation

For 1D earths, inversion is used to obtain the thickness and resistivities of each layer. (Wu, 1968; Nabetani and Rankin, 1969; Patrick and Bostick, 1969; Jupp and Vozoff, 1975; Patella, 1976; Bostick, 1977;

Petrick et al., 1977; Oldenburg, 1979; Larsen, 1981; Parker and Whaler, 1981; and others). From inversion one expects to obtain estimates of the parameters of the earth model plus one or more estimates of uncertainties in the parameter estimates. This method has almost entirely replaced the former curve matching system wherein a field curve was matched with one or more members of a catalogue of curves computed from forward modeling of a layered earth. Catalogues of forward computed curves appear in Cagniard (1953), Yungul (1961), and Srivastava (1967). In recent years it has become increasingly apparent that the earth is seldom plane layered so that numerical algorithms for two and three dimensional earths are becoming necessary in interpretation of MT/AMT data (Ranganayaki and Madden, 1980; Wannamaker et al., 1980, 1982).

Two dimensional models of the earth which have been reported in the literature include the vertical contact (Neves, 1957; Patrick and Bostick, 1969; Vozoff, 1972; Morrison et al., 1979), a vertical dipping dike (Vozoff, 1972), a 2D prism (Patrick and Bostick, 1969), a deep valley fill (Ward et al., 1973), and in recent years the general two dimensional earth (Pascoe and Jones, 1972; Rijo, 1977; Stodt, 1978; Morrison et al., 1979; Wannamaker et al., 1980; Nutter, 1981; Jiracek et al., 1982). The MT effects of two dimensional topographic features have been studied by Ku et al. (1973) and by Ngoc (1980). All of these algorithms compute the MT/AMT responses for both TE and TM modes of excitation. Two dimensional MT inversion has been discussed by Jupp and Vozoff (1977).

Means for calculating the MT responses of 3D earths have been reported by Jones and Vozoff (1978), Ting and Hohmann (1981), Wannamaker and Hohmann (1982), Wannamaker et al. (1982), Wannamaker (1983), and others.

Most MT data has been interpreted using 1D earth models at each site along a profile of stations. The resulting interpretation is a 2D cross-section of the earth (e.g. Stanley et al., 1977). Wannamaker et al. (1980, 1982) demonstrate that this approach can produce grossly misleading earth models. For 3D environments with strong preferred orientations, 2D TM mode modeling is preferred while TE algorithms are of limited use due to current-gathering (Wannamaker et al., 1982). Otherwise, full 3D interpretation is required. Wannamaker et al. (1982), Newman et al. (1983) and Wannamaker (1983) in addition demonstrate the importance of layering in which 3D bodies are situated.

3.0 PROBLEMS WITH THE MT/AMT METHOD

3.1 Overview

A number of problems arise which make it difficult to acquire MT data of high quality. If high quality data is gathered, however, a new set of problems arises in interpreting the data. In the next few paragraphs we sketch these problems.

3.2 Source Dimensions

All of the formulation presented above assumes that the MT fields are propagated as plane waves. This assumption was the source of much controversy in the early days of MT, but Madden and Nelson (1964) showed that usually the field is a plane wave at frequencies greater than 10^{-3} Hz in mid latitudes.

At frequencies below 1 Hz, the primary concern appears to be whether or not the fields due to equatorial and auroral electrojet ring currents in the E layer of the ionosphere can be treated as planar. Hermance and Peltier (1970) and Peltier and Hermance (1971) have studied the effects of such ring currents. They conclude that in conductive environments, the plane wave assumption is valid in the frequency range 10^{-4} Hz to 1 Hz. However, significant erorrs can occur at frequencies less than 10^{-1} Hz in areas where high resistivities are encountered if measurements are made within 500 km of the position vertically beneath the electrojet.

At frequencies above 1 Hz, the proximity of lightning discharges becomes important. Bannister (1969) studied the fields radiated from a vertical electric dipole over a homogeneous earth and concluded that the plane wave assumption is valid for distances greater than seven skin depths from the source.

Recently, Dimitriev and Berdichevsky (1979) showed that the plane wave formulation is applicable to a layered earth even if the fields vary linearly in the horizontal plane. If however, the plane wave assumption is not valid, then the extra field components associated with non-planar waves will be processed so as to produce bias in MT estimates (Stodt, 1983).

3.3 Random Noise

Random noise may arise in 1) the electrodes for E field measurement via chemical disequilibrium, b) movement of the E field wires in the earth's magnetic field when wind agitates them, c) movement of the H field sensors in the earth's magnetic field due to wind or seismic activity, d) microphonics in the H field sensors due to any motion e) thermal noise in the E and H field preamplifiers, f) quantization noise in A/D converters, g) non-linear behavior of the total recording system, h) sporadic departure from plane wave propagation, and i) sporadic cultural noise due to power lines, telephone lines, rail electrification, pipeline corrosion protection, radio interference, and the power sources in the recording instrumentation. Obviously one attempts to minimize these noise sources prior to recording and processing. Ultimately, the processing system must be designed to minimize, evaluate, and place statistical limits on errors introduced into MT transfer functions by random noise.

3.4 Systematic Noise

Most of the noise sources described in 3.3 above are also capable of introducing systematic noise into estimates of the MT transfer functions. As Stodt (1983) points out, the systematic noise must be treated independently of the random noise in any statistical evaluation of noise in MT data. As a result of systematic noise, biased estimates of the MT transfer functions

result. To attempt to eliminate this problem, the use of a remote reference has become common practice (Gamble et al., 1979). Stodt (1983) demonstrates that to some extent this bias can be removed from conventional data, i.e. data recorded without a remote reference. Nevertheless, use of a remote reference is recommended.

3.5 Geological Noise Due to Overburden

In areas where there is irregular conductive overburden, current channeling into a patch of deeper or more conductive overburden will produce anomalies even to the lowest frequencies. Unless these anomalies are interpreted via 2D or 3D modeling, they can be mistaken for deep seated features. Wannamaker (1983) illustrates these effects. We shall demonstrate them clearly in the case history to follow.

3.6 Resolution

In MT surveys, resolution of layers in a flatly dipping layered structure is usually of more concern than resolution of adjacent steeply dipping bodies. Mostly this arises because we rely upon active source systems for delineating fractures and faults in the shallower parts of geothermal systems, while we rely upon MT for detecting the more diffuse heat sources at depth.

Madden (1971) demonstrated the principle of equivalence in MT soundings. For simplicity we shall analyze the MT response of a two layer earth, although the analysis is readily extended to more layers.

If layer 1 is electromagnetically thin, i.e. wavelengths in the layer are much greater than the thickness of the layer ($k_1 h_1 \ll 1$), then $\tanh(ik_1h_1) \approx ik_1h_1$ and equation (4) becomes

$$\hat{Z}_1 \approx Z_2 \frac{1 + ik_2h_1}{1 + Z_2\sigma_1 h_1}, \tag{79}$$

where we have made use of the definition of the intrinsic impedance. If layer 1 is conductive, i.e. $\sigma_1 >> \sigma_2$, then (79) reduces to

$$\hat{Z}_1 \simeq Z_2/(1 + Z_2\sigma_1 h_1) \quad . \tag{80}$$

The effect of a thin conductive layer upon $\hat{Z}_1$ arises only from its conductivity-thickness product; neither σ_1 nor h_1 can be resolved independently. If, on the other hand, layer 1 is resistive, meaning $\sigma_1 << \sigma_2$, then (79) reduces to

$$\hat{Z}_1 \simeq Z_2 (1 + k_2 h_1) \tag{81}$$

One sees that the effect of a thin resistive layer upon $\hat{Z}_1$ arises solely from its thickness. These conclusions can be shown to apply to any layer within an arbitrarily layered sequence. In the general case, a buried layer ℓ appears thin if $k_\ell h_\ell << 1$ throughout the frequency range for which EM waves are able to penetrate from the surface to the buried layer.

3.7 Topography

The effect of topography on the results of an MT survey may be significant. Figure 17 illustrates distortion of telluric currents at low frequencies. Anomalous secondary electric and magnetic fields result. The TE and TM apparent resistivities due to a ridge of two different resistivities at two different frequencies are illustrated in Figure 18. (Ku et al., 1973; Ngoc, 1980). A valley causes just the opposite effect on the electric field. Also, as is the case for buried structures, the TM response of 2D topography asymptotes to a non-zero low-frequency limit where boundary charges on the surface of the earth act as sources for current variations below.

Note also that the TM mode topographic effects are much stronger than

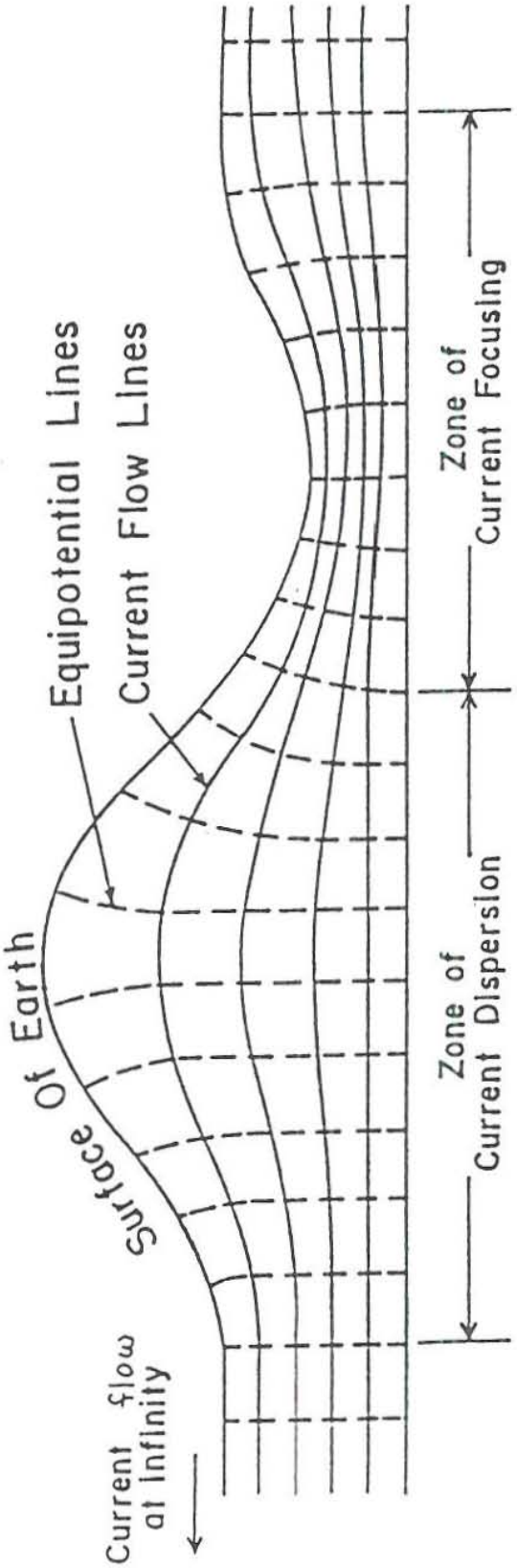

Figure 17. Distortion of current flow lines due to topography.

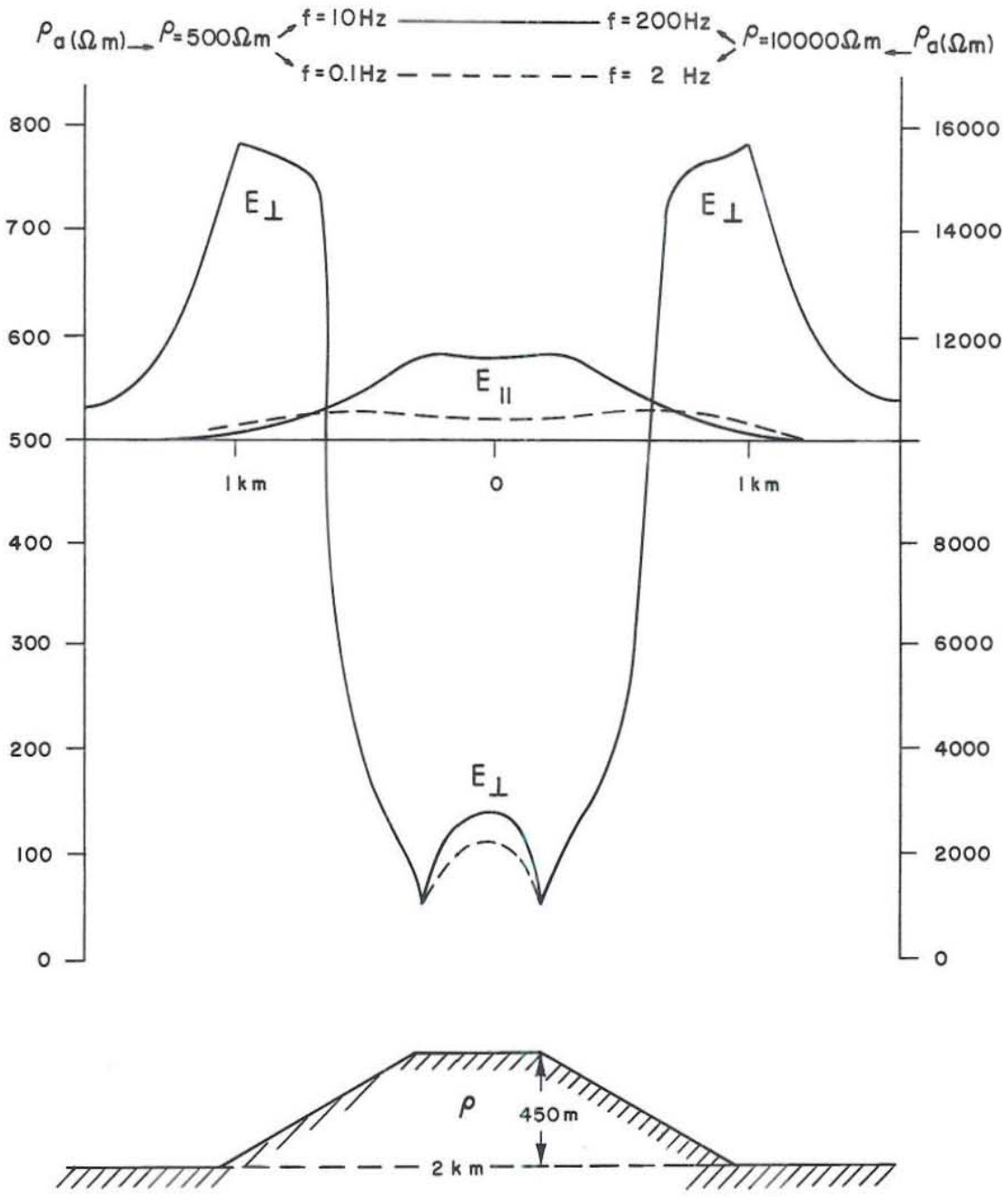

Figure 18. TM mode ($E_{\perp}$) and TE mode ($E_{\parallel}$) anomalies over a 2D ridge (after Ngoc, 1980).

those of the TE mode, especially near corners of the structure. The magnitude of the responses in this case indicates that one should give careful consideration to the effects of topography if the breaks in slope in the survey area are as steep and abrupt as those studied here.

3.8 Current Channeling

Current channeling is merely part of the response of a 2D or 3D earth. One-dimensional earth models do not include it at all while 2D earth models include it only for the TM mode. Thus current channeling is only a problem if it is ignored in the modeling process. Ting and Hohmann (1981) provide a particularly good ilustration of the effects of current channeling and we repeat it here.

Theoretical results for a three layer model are compared with those for horizontal 3D square slabs in place of the middle layer. The 1D model consists of an anomalous layer with resistivity 5 Ω-m and thickness 100 m buried 200 m deep in a half space of resistivity 100 Ω-m. To compare with 3D models, we replace the infinite anomalous layer by a finite square slab having different lateral extents. The apparent resistivity is calculated over the center of the slabs and plotted as a function of frequency. The comparison is shown in Figure 19 for square slabs 400, 800, 1200 and 1600 meters on a side. The 3D results should be reasonably accurate based on convergence checks and comparisons with 2D TM models.

The largest 3D slab shown is 1600 m. The 3D results appear to be converging to the 1D curve, but the convergence is very slow at the lower frequencies. This illustrates the important point that because surface charges at its boundaries are important, a 3D slab must be very large for 1D interpretation to apply. If 1D inversion is applied to the results obtained

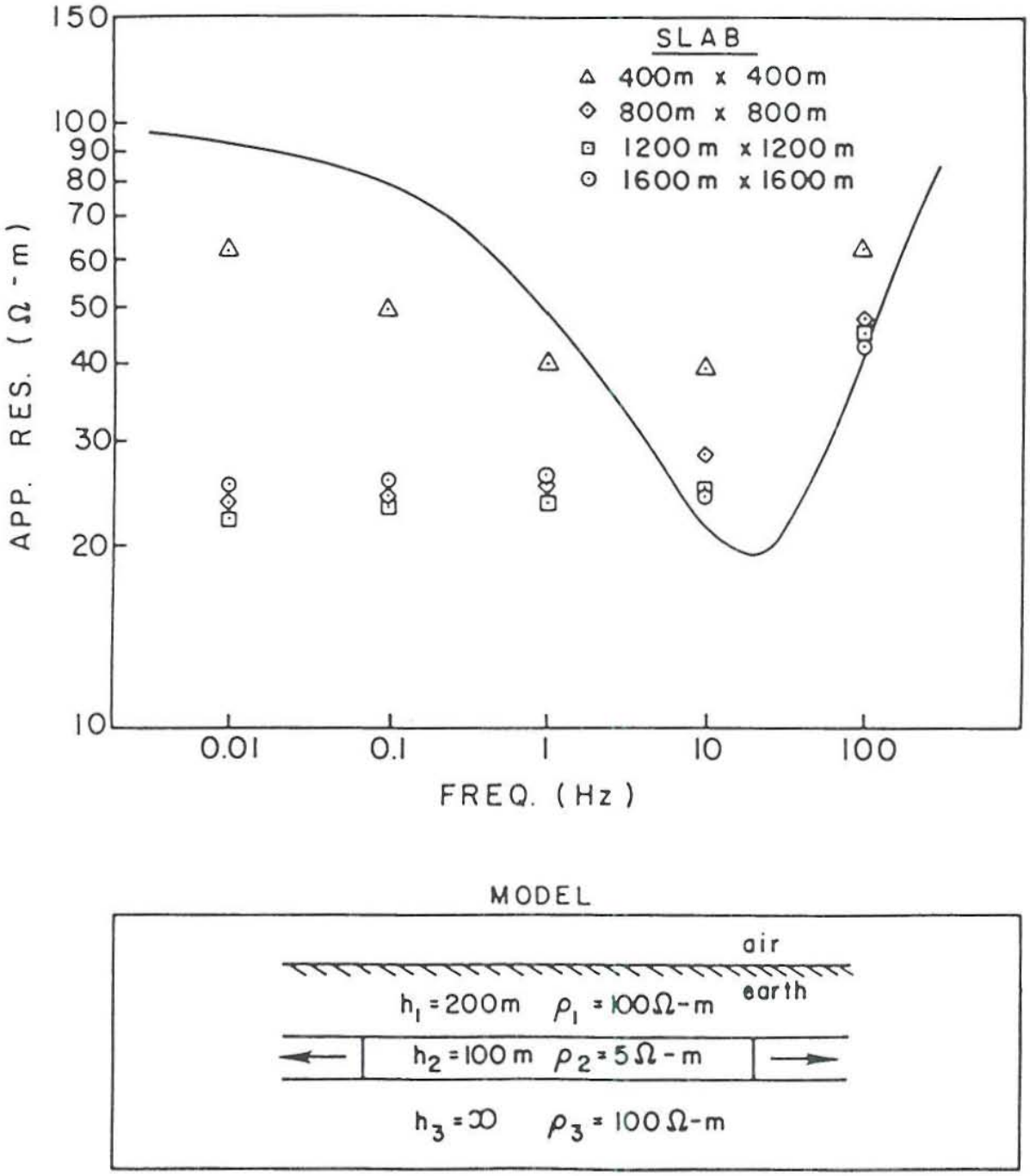

Figure 19. Apparent resistivity 1D curve (solid) and computed data points for four different equidimensional 3D slabs (after Ting and Hohmann, 1981).

for the largest slab, the results will be erroneous.

3.9 Depth of Exploration and Detectability

Depth of exploration is often stated to be one skin depth δ, where

$$\delta = \sqrt{\frac{2}{\omega\mu\sigma}} . \tag{82}$$

This simplification is misleading, because noisy data or surface geological noise can obscure the responses of deep bodies. However, with care in both data acquisition and in data interpretation, depths of exploration well in excess of 100 km can be achieved for infinite interfaces.

For 2D or 3D bodies, depth of exploration can be considerably less. Newman et al. (1983) have explored the possibility of detecting deep magma chambers with MT. If the magma chamber is electrically connected to a highly conducting half-space, it probably will not be detected. On the other hand, if the basal half-space is resistive or if the earth is not layered, the magma chamber is more readily detected.

Apparent resistivity and impedance phase sounding curves directly over the 3D model of Figure 20 appear in Figure 21 and are compared to curves centered over a 2D structure of identical cross-section and to curves representing the response of just the 1D layered sequence in the absence of the inhomogeneity (Newman et al., 1983). Note that departures from the purely layered response by both modes of the 3D body signature are very subdued; we would consider such a response to stand a low probability of being recognized, particularly in light of the frequent existence of near-surface geological noise which obscures target MT anomalies (Wannamaker et al., 1982). The 2D TM and corresponding 3D results agree very closely as expected indicating that increasing the strike length of this structure will not facilitate its

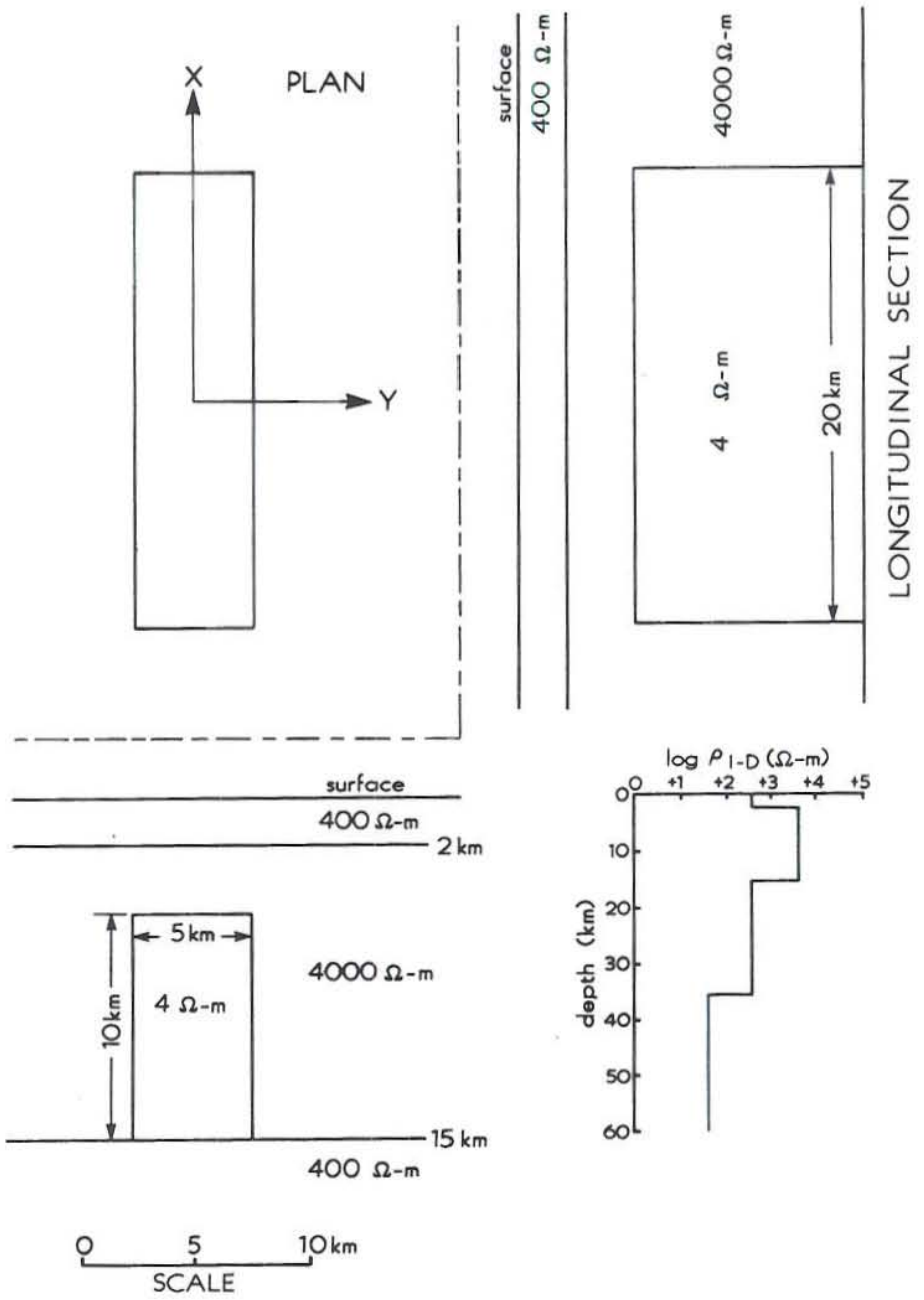

Figure 20. 3D model of magma chamber in a layered earth (after Newman and Wannamaker, 1983).

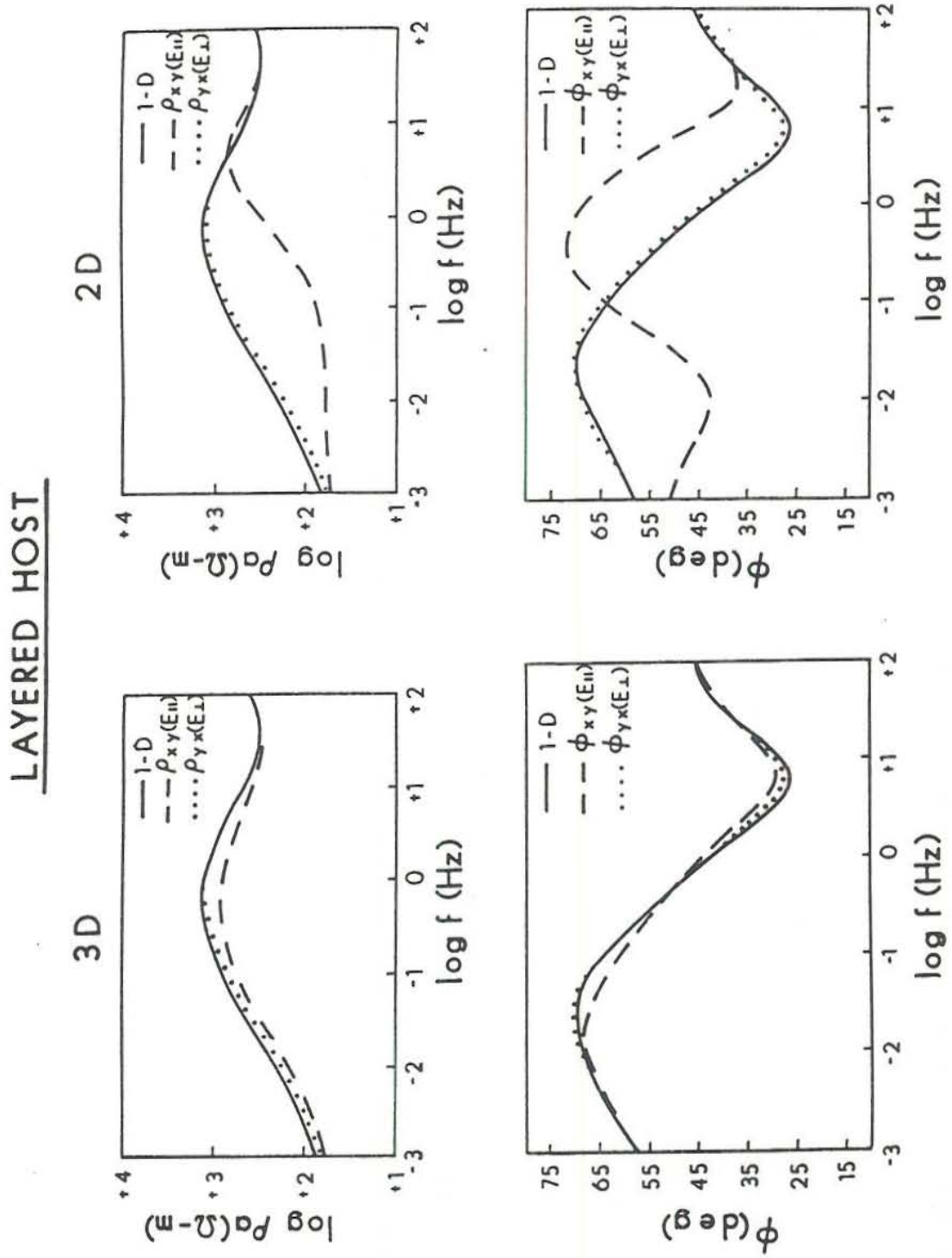

Figure 21. Apparent resistivity and impedance phase curves over the magma chamber of Figure 20, layered earth (after Newman and Wannamaker, 1983).

detection using the apparent resistivity ρ_{yx} and impedance phase ϕ_{yx}. On the other hand, the 2D TE response in Figure 21 is quite strong, dwarfing the corresponding anomalies in ρ_{xy} and ϕ_{xy} caused by the 3D structure. We interpret this discrepancy as being due to current-gathering in the 3D body, whereby secondary currents induced about the 3D structure are essentially short-circuited into deeper, less resistive media of the layered host and are inhibited by the 4000 Ω-m material from reaching the surface to produce an anomaly (Newman et al., 1983).

To verify this interpretation, the 3D body of Figure 20 was removed from its layered host and simulated within a uniform 400 Ω-m half-space (see Figure 22). In this case, the 2D TM anomaly as well as the anomalies in both (ρ_{xy}, ϕ_{xy}) and (ρ_{yx}, ϕ_{yx}) over the 3D body are much stronger than the anomalies in Figure 21. (Anomalies here mean departure from 1D response.) This high sensitivity of the response of a 3D body to its layered host underscores the importance of simulations using an algorithm handling 3D bodies in arbitrarily layered earths.

3.10 Frequency-independent Anistropy

In Figure 23 we see principal tensor apparent resistivities ρ_{xy} and ρ_{yx} and impedance phases ϕ_{xy} and ϕ_{yx} at a single site over the frequency range 10^2 to 10^{-3} Hz. This sounding comes from a hydrocarbon environment, but the particular characteristics upon which we dwell have been noticed in many areas. Specifically, we refer to the nearly order-of-magnitude anisotropy in apparent resistivity persisting to the very highest frequencies at which data was recorded. The anisotropy does not vary significantly as frequency falls and, correspondingly, no substantial anisotropy in impedance phase is noted throughout the frequency range.

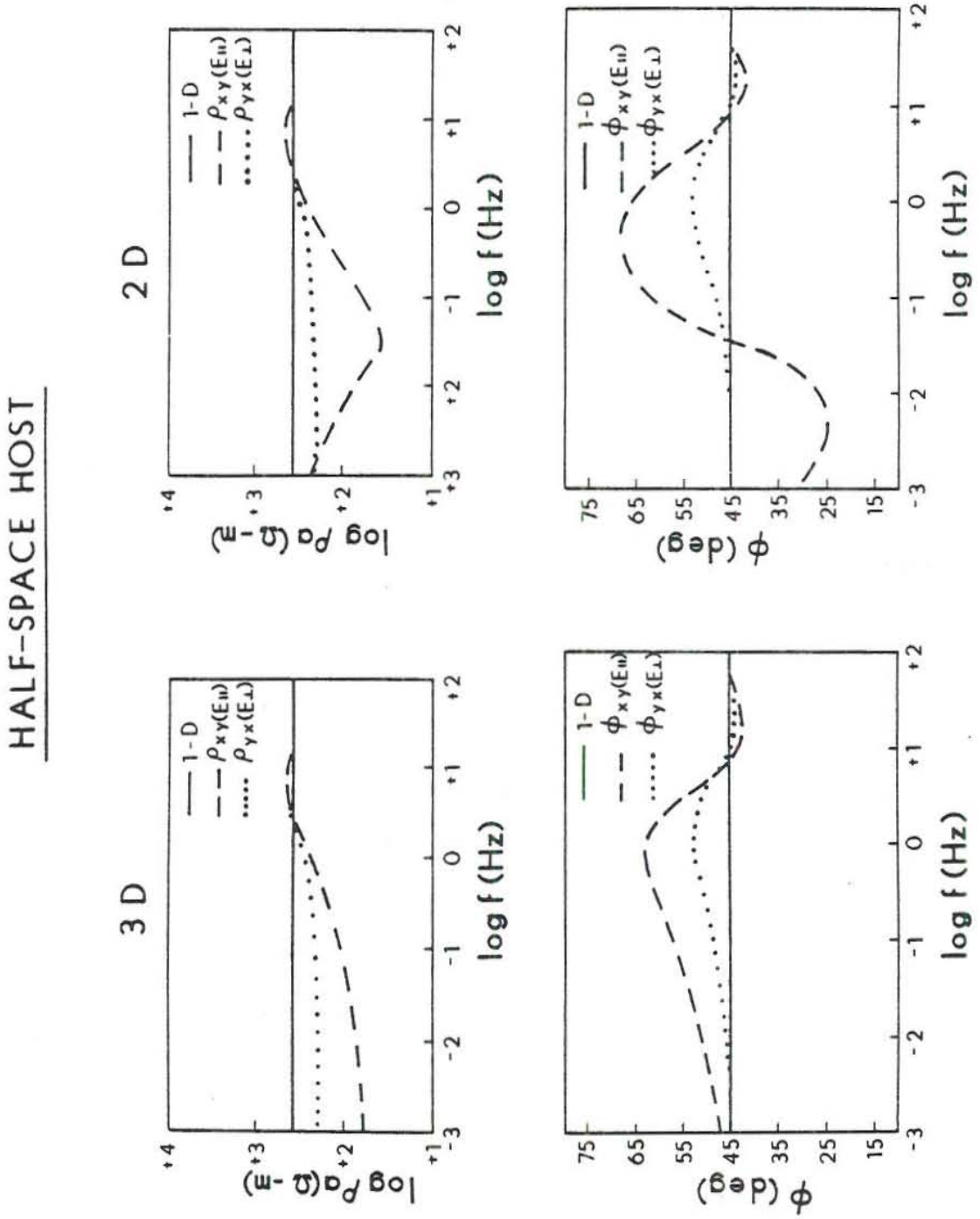

Figure 22. Apparent resistivity and impedance phase curves over the magma chamber of Figure 20, homogeneous half-space (after Newman and Wannamaker, 1983).

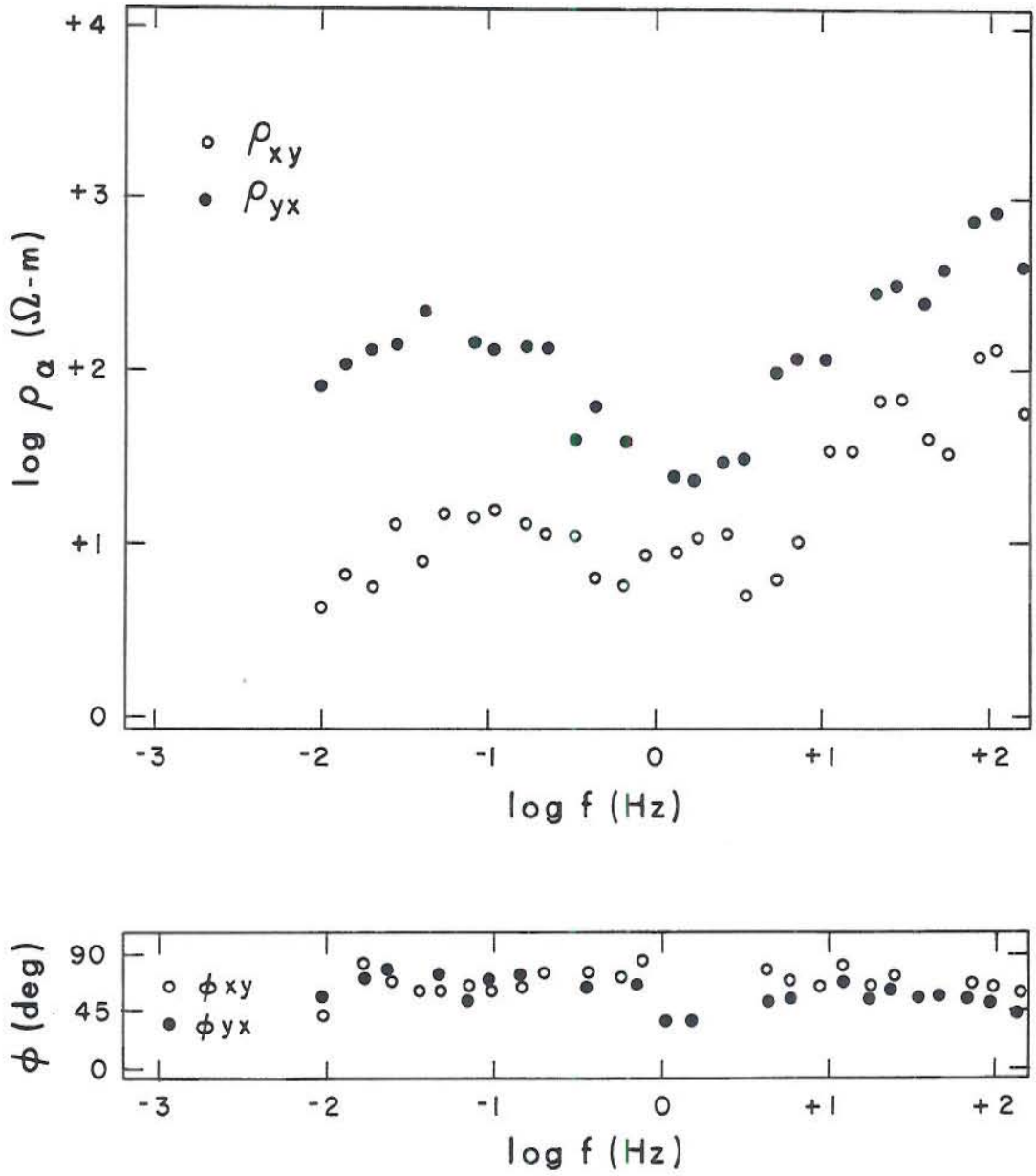

Figure 23. Effect of anistropy on apparent resistivities (after Wannamaker, 1983).

This effect of anisotropy is a great nuisance. A one dimensional inversion of each curve would yield two layered resistivity models whose layer contrasts were essentially the same. However, as can be verified from equation (4), the absolute resistivities of the layers computed from the curve with the lesser apparent resistitivies (ρ_{xy} in this case) would be lower by an order of magnitude while the absolute layer thicknesses would be lower by about a factor of three than those computed from the curve with the greater apparent resistivities (ρ_{yx}).

4.0 ILLUSTRATIVE APPLICATION OF MT/AMT

4.1 Roosevelt Hot Springs Thermal Area

4.1.1 Location

The Roosevelt Hot Springs geothermal system is located along the western side of the Mineral Mountains, approximately 12 mi (19 km) northeast of Milford, Utah (Fig. 24). The geothermal system is a high-temperature water-dominated resource, and is structurally controlled with permeability localized by faults and fractures cutting plutonic and metamorphic rocks.

4.1.2 Regional Setting

Ross et al. (1982) provide the following description of the regional setting.

"The Mineral Mountains are a north-trending horst bounded by Basin and Range normal faults and lie at the western edge of the transition zone between the Colorado Plateau and the Basin and Range physiographic provinces. The area is located on the western edge of the Intermountain seismic belt as defined by Smith and Sbar (1974). In addition, the Roosevelt Hot Springs KGRA lies along east-west-trending magnetic anomalies which follow the trend of the Wah Wah-Tushar mineral belt (Mabey et al., 1978). This belt has been the site of intrusive activity through the Tertiary and into Quaternary time. Associated with this igneous activity are deposits of uranium and base and precious metals.

The central part of the mineral Mountains is a structural high relative both to adjacent ranges and also to the northern and southern parts of the range. In these northern and southern areas, sedimentary rocks of Cambrian through Cretaceous age are exposed. The southern area also contains volcanic

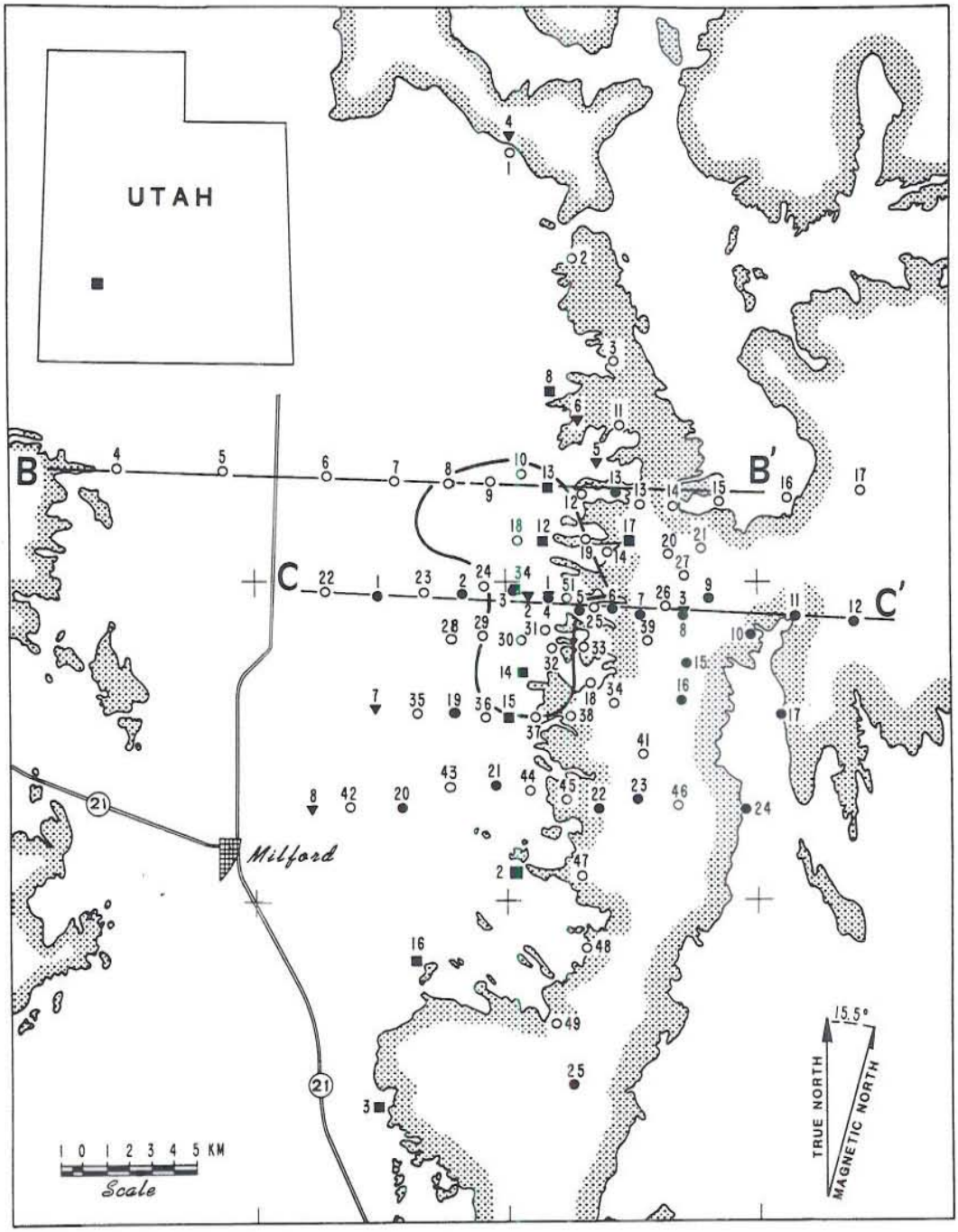

● GEOTRONICS CORP. (1976)

○ GEOTRONICS CORP. (1978)

■ UNIV. OF TEXAS AT AUSTIN (1977)

▼ UNIV. OF CALIFORNIA AT BERKELEY (1979)

MT./AMT. STATIONS
ROOSEVELT HOT SPRINGS KGRA, UTAH

Figure 24. Locations of MT/AMT stations, Roosevelt Hot Springs KGRA, Utah (after Wannamaker et al., 1980).

and plutonic rocks of Tertiary age (Earll, 1957). In contrast, the central part of the Mineral Mountains contains Precambrian metasedimentary rocks and Tertiary plutonic rocks of the Mineral Mountains intrusive complex (Sibbett and Nielson, 1980). These Tertiary rocks possibly represent plutonic equivalents of the Marysvale volcanic province."

4.1.3 Local Setting

Again from Ross et al. (1982) we quote,

"The geology in the vicinity of the Roosevelt Hot Springs geothermal system has been described in detail by Nielson et al. (1978). The central part of the Mineral Mountains has been mapped by Sibbett and Nielson (1980). A simplified geologic map of the Roosevelt Hot Springs area is shown in Figure 25.

The oldest unit exposed in the area of the geothermal system is a banded gneiss which was formed from regionally metamorphosed quartzo-feldspathic sediments. The rock was metamorphosed to the upper amphibolite facies during middle Proterozoic time. The banded gneiss is strongly layered with adjacent layers distinguished principally on the content of mafic minerals. The rock is compositionally heterogeneous and contains thick sequences of quartzo-feldspathic rocks. The unit also contains metaquartzite and sillimanite schist layers which have been differentiated in the more detailed geologic study (Nielson et al., 1978).

The Mineral Mountains intrusive complex is the largest intrusive body exposed in Utah. K-Ar dating and regional relationships suggest that the intrusive sequence is middle to late Tertiary in age. In the vicinity of the geothermal system, the lithologies range from diorite and granodiorite through granite and syenite in composition (Fig. 24).

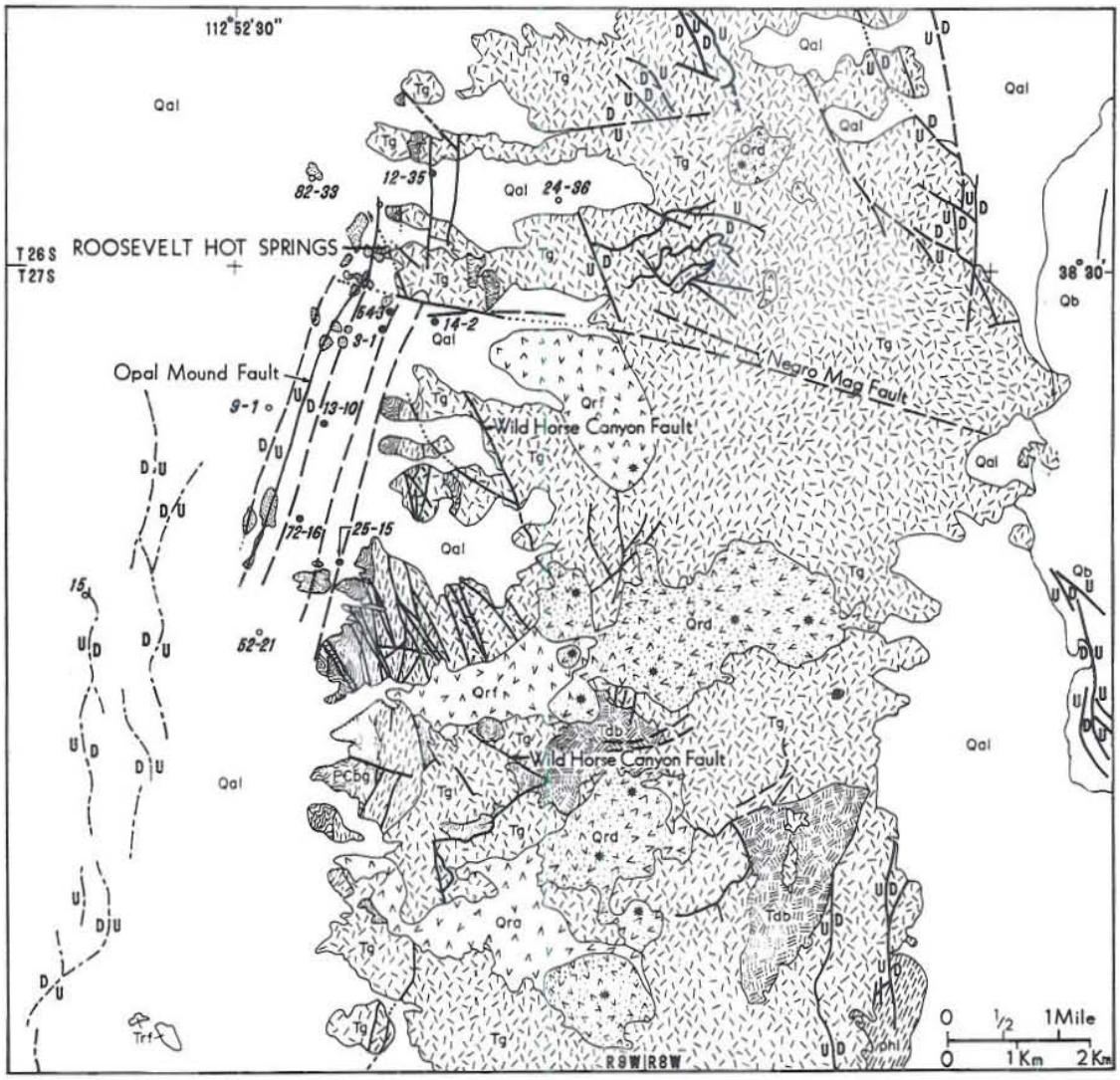

Figure 25. Geologic map of Roosevelt Hot Springs KGRA and vicinity (after Sibbett and Nielson, 1980).

Rhyolite flows, pyroclastics, and domes were extruded along the spine of the Mineral Mountains 800,000 to 500,000 years ago (Lipman et al., 1978). The flows and domes are glassy, phenocryst-poor rhyolites. The pyroclastic rocks are represented by air-fall tuff and nonwelded ash-flow tuffs. Smith and Shaw (1975) hypothesized that young rhyolites such as these are indicative of an upper-level magma chamber which could serve as a heat source for geothermal systems.

Hot spring deposits in the vicinity of the geothermal system have been mapped as siliceous sinter, silica-cemented alluvium, hematite-cemented alluvium, and manganese-cemented alluvium. The principal areas of hot-spring deposition are along the Opal Mound fault and at the old Roosevelt Hot Springs. In both of these areas, the deposits consist of both opaline and chalcedonic sinter.

The geothermal reservoir at Roosevelt Hot Springs is structurally controlled. The controls are thought to be produced by the intersection of the faults mapped in the KGRA (Nielson et al., 1978, 1979). The structural evolution of the Roosevelt Hot Springs geothermal system is envisioned as follows. During rapid uplift of the Mineral Mountains structural block, westward-dipping low-angle normal faults formed. The most important of these is the Wild Horse Canyon fault (Fig. 25). This tectonic event produced intense zones of cataclasis both along low-angle fault planes and within the hanging wall of the principal fault block. The cataclastic zones within the hanging wall are steeply dipping zones up to 10 ft (3 m) wide which strike generally to the northwest. These zones in the hanging wall were produced by internal brecciation and interaction between rigid blocks during the low-angle faulting. East-west-trending high-angle normal faulting, represented by the

Negro Mag fault, cuts the low-angle faults. The trend is parallel with the Wah Wah-Tushar mineral belt and is probably related to movement along this deep-seated structural trend.

The Opal Mound fault and parallel structures are north-northeast-trending faults which are the youngest structures in the area. They localize siliceous hot-spring deposits and are often marked by zones of alteration and silicification of alluvium. To the west of the Mineral Mountains lies the Milford Valley which is underlain by unconsolidated alluvium and minor volcanics to depths as great as 1.5 km."

4.2 MT/AMT at Roosevelt Hot Springs Thermal Area

4.2.1 Description of Data Base

During a period of three years extending from 1976 to 1978, 93 tensor MT soundings were monitored in the central Mineral Mountains and Milford Valley in the vicinity of RHS (see Figure 24). The data collection and processing were performed by Geotronics Corp. of Austin, Texas, the University of Texas at Austin, and Lawrence Berkeley Laboratory of the University of California at Berkeley. Tensor apparent resistivities (ρ_a), impedance phases (ϕ) and the vertical magnetic field transfer functions and strike estimators were provided over a frequency range of 10^{-3} to 10^{2} Hz. In Figure 24 the outcrop pattern of sedimentary, igneous and metamorphic rocks bounding the Milford Valley sediments is lightly stippled while the solid contour is the 400 mWm^{-2} thermal contour. Station numbers referred to in the text have been prefixed according to the year in which they were occupied.

Wannamaker et al. (1980, 1983) provide an extensive interpretation of the MT data at Roosevelt Hot Springs. In what follows, we present a summary of the salient points of that interpretation.

4.2.2 1D Interpretation

We demonstrate the effects of small-scale, near-surface conductors upon 1D interpretations by examining a north-south trending line of soundings that spans the thermal anomaly area. Values of principal apparent resistivity ρ_{xy} over the entire observed frequency range appear for this selected line in the upper half of Figure 26. This quantity was identified by our contractors as transverse electric on the basis of principal axis estimations involving Z-strike and either Y_z-strike or K_z-strike. Due to geologic noise, however, these axes have significant inconsistencies. The stations themselves lie close to the eastern border of the Milford Valley sediments and locations of individual sites may be deduced from Figure 24. The apparent resistivities appear as a pseudosection; log frequency defines the ordinate and horizontal distance defines the abscissa for a contour plot of ρ_{xy}. The major feature of the pseudosection is the complicated low resistivity pattern persisting to the lowest observed frequencies directly over the thermal anomaly area. Assuming that the proposed thermal reservoir and deep heat source exist beneath the thermal anomaly area, then the MT response one observes in Figure 26 will be a composite of the responses of these two features along with the responses of the valley, the regional layered conductivity, and the near-surface variable alteration.

In the lower half of Figure 26 are presented interpreted continuous 1D intrinsic resistivity profiles based upon a simple analytic inversion scheme (Boehl et al., 1977; Stanley et al., 1977). The comparison of these continuous profiles with layered inverse models computed from a given sounding seems reasonably close (Wannamaker, 1978). The character of these inferred continuous resistivity profiles as one crosses the thermal anomaly from one end of the line of stations to the other is very interesting. For every

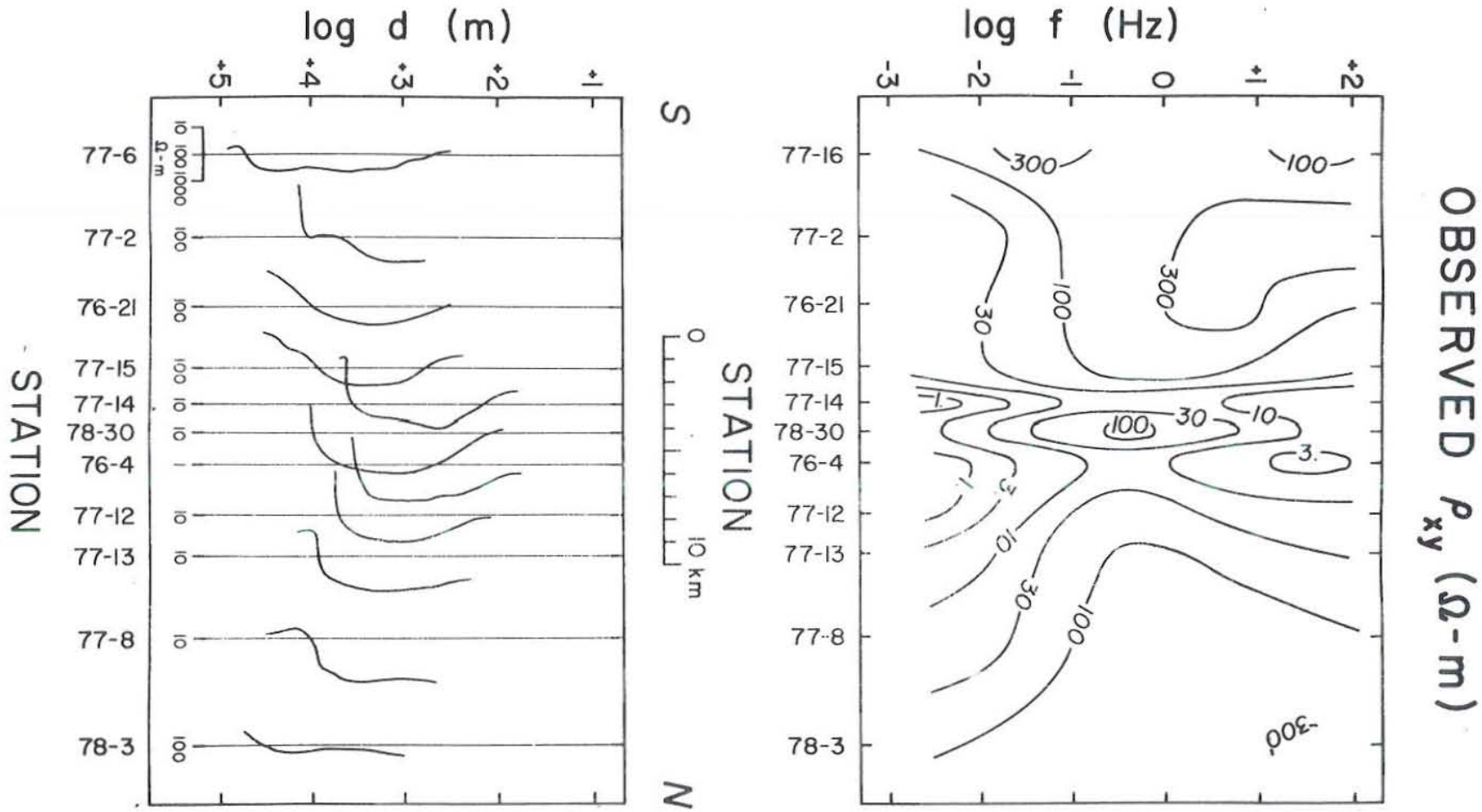

Figure 26. Observed apparent resistivity (ρ_{xy}) pseudosection and continous 1-D inversion results for N-S trending profile of stations over thermal anomaly area. Contour values for pseudosection are in Ω-m. Continuous inversion results plotted on a logarithmic scale with a reference value in Ω-m given for each sounding (note elaborated scale for station 77-16) (after Wannamaker et al., 1980).

station, the intrinsic resistivities at the greatest depths at which the profiles can be computed appear to be decreasing quite rapidly with increasing depths. Under the thermal area, however, depths at which these decreases occur are particularly shallow; 3 to 10 km as compared to 15 to 40 km for sites closer to the ends of the line. These calculations imply that anomalously conductive structure exists in the intermediate crust below the thermal area, perhaps representing a partially molten magma chamber that is the heat source for the geothermal system. We maintain nevertheless that the much greater part of this inferred structure is an artifact of the 1D inversion approach and is actually induced by the near-surface resistivity structure associated with hydrothermal alteration.

To show computationally that the near-surface, low-resistivity structure associated with the thermal anomaly is mostly responsible for the apparently anomalous conductive structure in the intermediate to deep crust below the thermal anomaly, as implied by the continuous 1D inversions of Figure 26, requires an algorithm which can include boundary polarization charges and a layered earth host in its formulation. The finite N-S strike extent of the near-surface resistivity structure just described can be simulated approximately using a 2D TM algorithm. Using this 2D program, we have calculated the resistivity cross section of Figure 27 and the ρ_a pseudosection in the upper half of Figure 28 in an attempt to match the observations. A comparison that is generally close between pseudosections of Figures 26 and 28 has been obtained, particularly concerning the resistivity lows directly associated with the thermal anomaly area, using lateral inhomogeneities which extend no deeper than 500 m. One must conclude from this that many important characteristics of MT observations to arbitrarily low frequencies can be determined by very shallow structure.

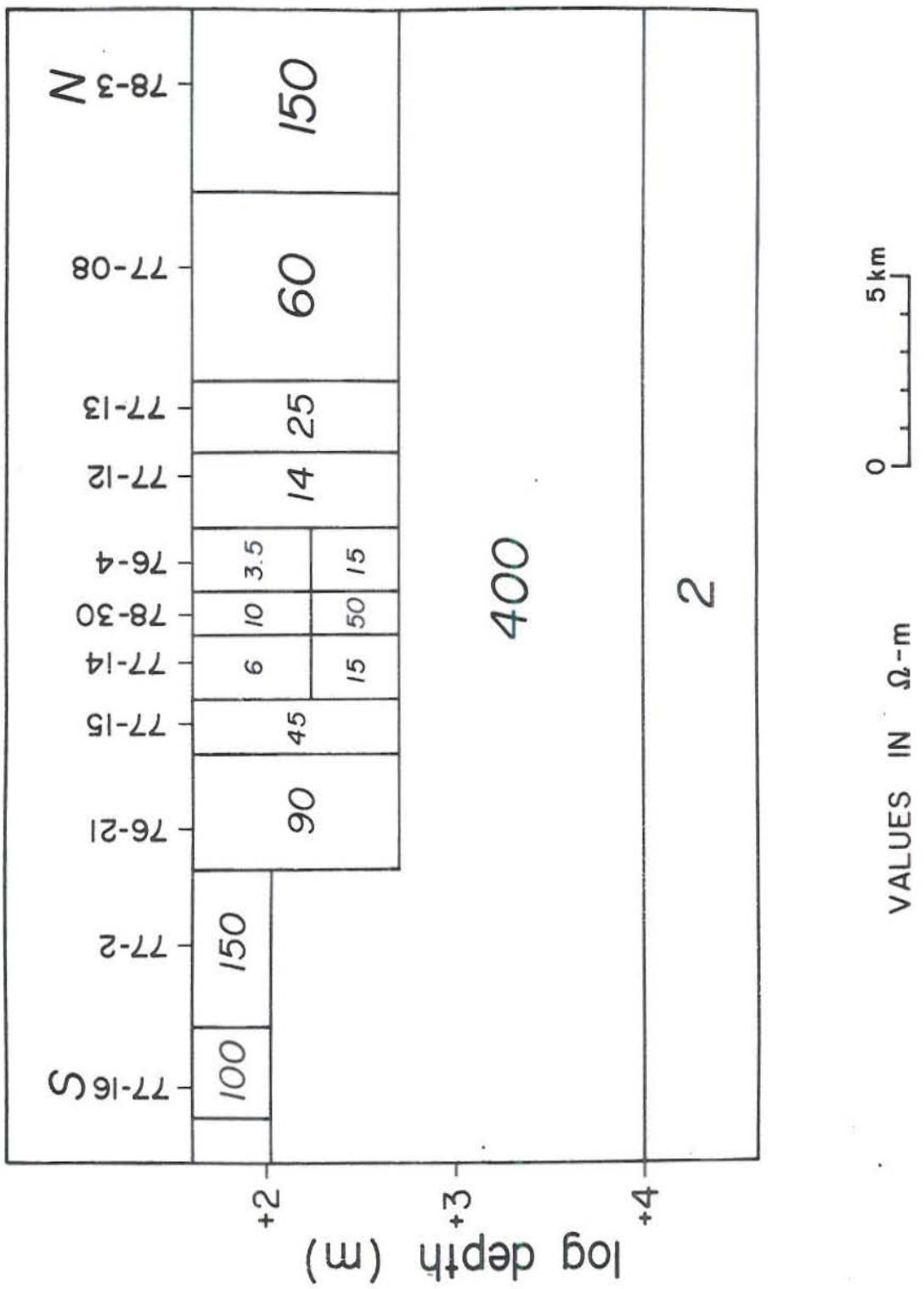

Figure 27. Finite element resistivity section computed using lateral inhomogeneities in only the upper 500 m to fit the observations in the top half of Figure 25. Values of individual media in Ω-m (after Wannamaker et al., 1980).

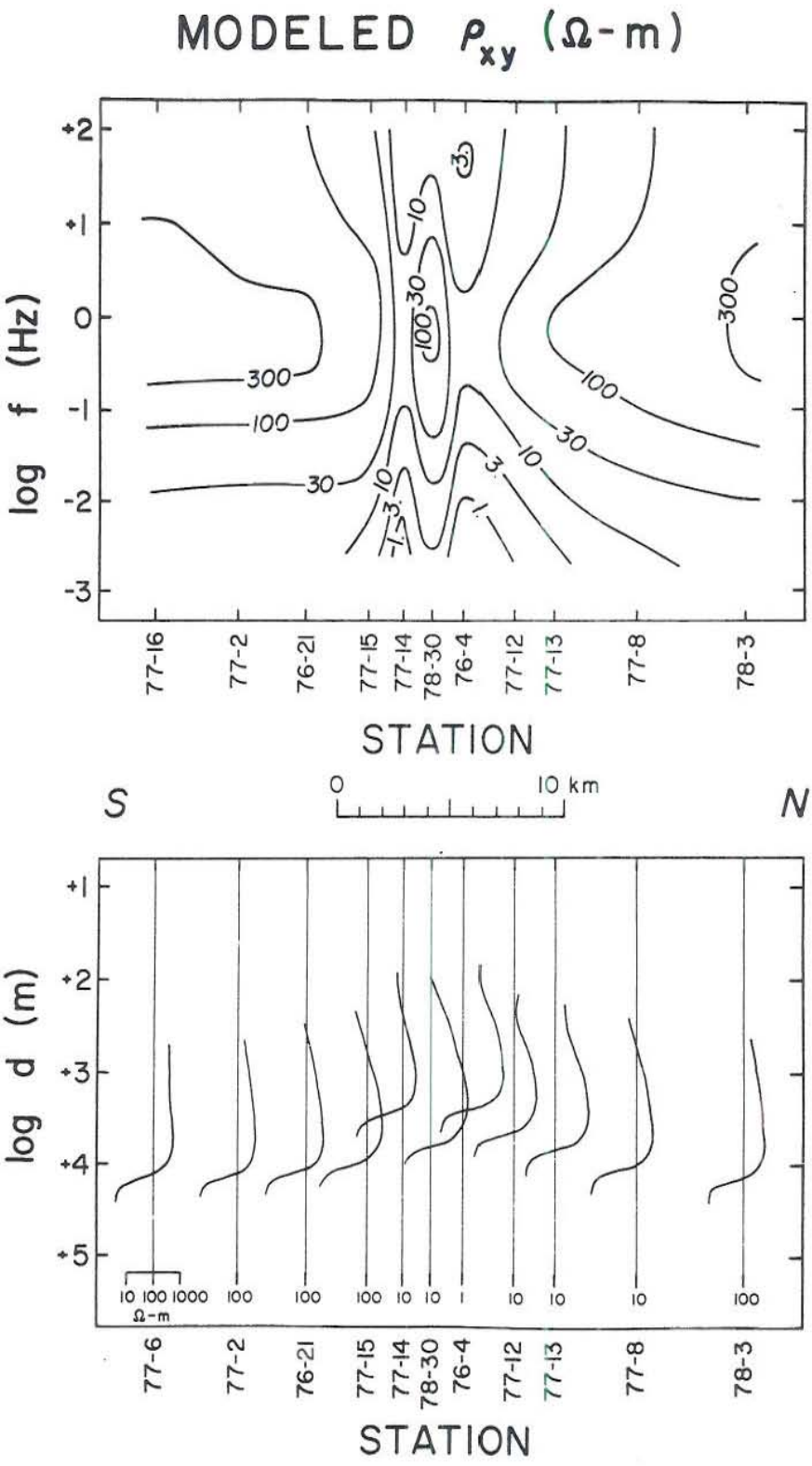

Figure 28. Computed apparent resistivity (ρ_{xy}) pseudosection and continuous 1-D inversion results corresponding to the finite element model of Figure 26. Conventions are as for Figure 25 (after Wannamaker et al., 1980).

We note at this point the progression of resistivities of the layered host in Figure 27 from 600 Ω-m over the depth interval 1 to 20 km to 2 Ω-m at greater depths. This behavior can be explained for the most part as a combination of the effects of the regional layered conductivity and the Milford Valley sediments. As will be discussed later, we believe the true resistivities of the layers of the regional profile are much higher than shown in Figure 27 and the depths to the most conductive units are much greater. Now the length of the line of soundings considered in this exercise is about 25 km, which is less than the N-S strike extent of the valley sediments of 35 to 40 km. The valley is not allowed for by the 2D TM routine that yielded Figure 27 and so falsely conductive and shallow units of the regional profile were inferred.

To complete this investigation, we inverted the computed sounding data to yield the continuous intrinsic resistivity profiles in the lower portion of Figure 28. The ensemble of profiles bears an overall similarity to that in the lower half of Figure 26 with the implication of anomalously conductive structure existing in the deep to intermediate crust directly underneath the thermal area. One must conclude that false conductivities and falsely shallow interface depths will be generated from a 1D inversion scheme using ρ_a and ϕ data measured over 3D near-surface conductive structure. In particular concerning geothermal systems, the near-surface conductivity structure within a thermal area created by the upward convection of hot brines with attendant hydrothermal alteration of rocks and alluvium may itself be the cause of an apparent but false conductor beneath the system, suggestive of a partially molten heat source, if the true complexity of this shallow conductivity makeup is not properly accounted for.

4.2.3 2D Interpretation

Our research group has developed a program capable of calculating multifrequency ρ_{yx} and ϕ_{yx} (identified as TM mode) results for complicated resistivity cross sections within layered hosts (Rijo, 1977; Stodt, 1978). To make use of this algorithm we have chosen profiles of stations B-B' and C-C' of Figure 24 as meeting the necessary criteria. The two profiles trend nearly perpendicular to the margin of the bulk of the valley sediments, as evidenced by geologic mapping and gravity. They are also, for the most part, rather centrally located with respect to the northern and southern limits of the valley, also on the basis of mapping and gravity.

The observations ρ_{yx} and ϕ_{yx} for these two lines appear in Figures 29 and 32, as pseudosections. The coordinate axes for all sites in these profiles lie in a uniform direction which is approximately N15°E. Such an azimuth is compatible with preferred geologic trends indicated by the previously mentioned mapping and geophysical surveys along with some of the better quality tipper-strike estimations. Picking uniform coordinate directions has greatly smoothed certain aspects of the observed data, particularly the mid- to low-frequency values of impedance phase.

Line B-B': We discuss first details of the pseudosections of line B-B' since it lies north of the thermal area and is expected to be affected by just the valley and regional layered structure and not significantly by features directly related to the geothermal system. The observed results for this line exhibit a virtually classic horst-graben response for the TM mode. Within the margins of the conductive valley sediments, apparent resistivities for stations 78-5 to 78-8 (Figure 29) are monotonically decreasing functions as frequency decreases, falling from somewhat over 3 Ω-m at 10 Hz to below 0.1 Ω-

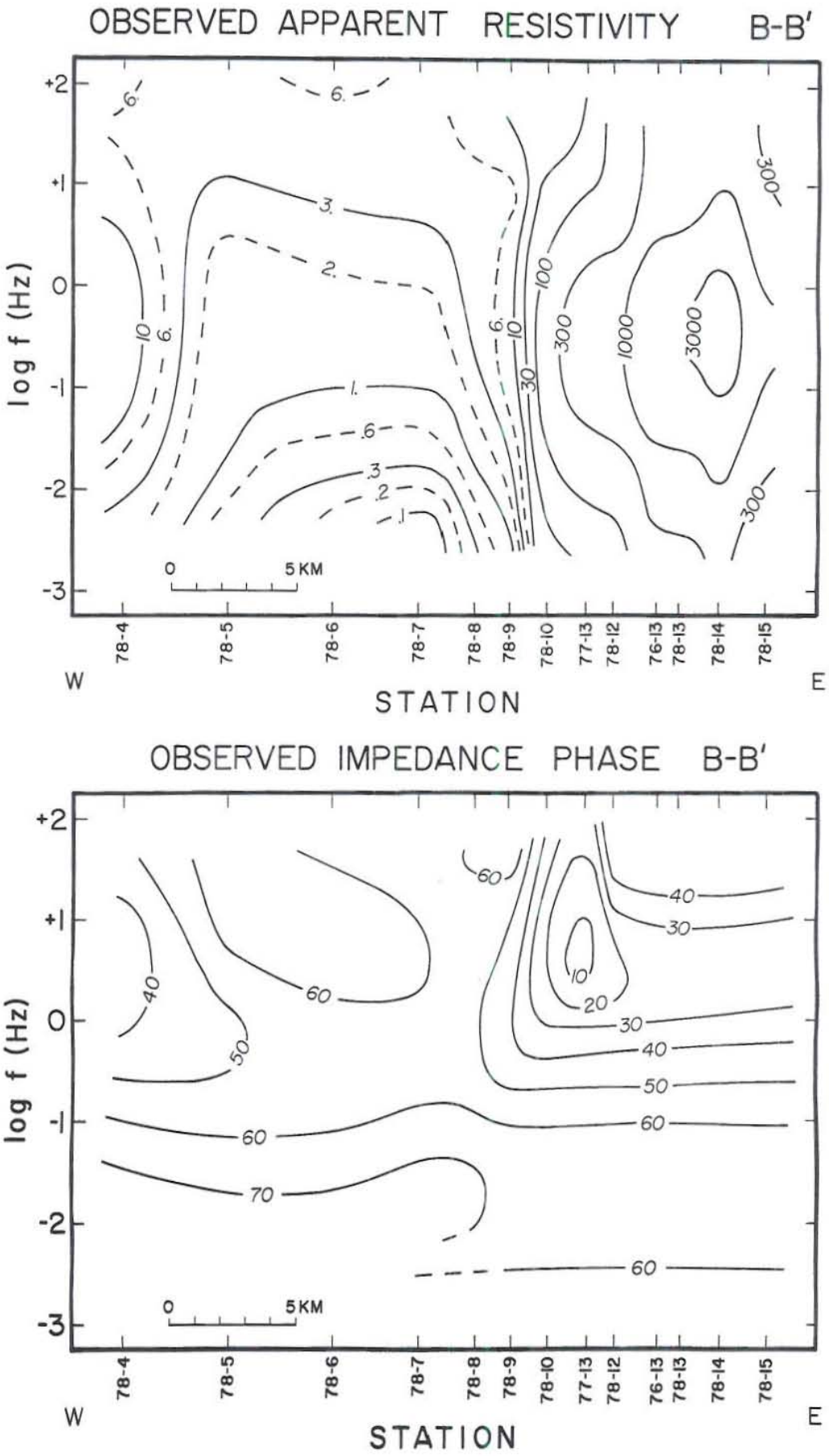

Figure 29. Observed apparent resistivity and impedance phase pseudosections for profile B-B' of Figure 24. Contours of ρ_{yx} are in Ω-m while those of ϕ_{yx} are in degrees (after Wannamaker et al., 1980).

m at very low frequencies for station 78-7. Impedance phase values remain above 45° here with a maximum exceeding 70° at low frequencies. Substantial gradients in ρ_{xy} at mid to lower frequencies are responses due to the rangefront faulting bounding the sediments between sites 78-4 and 78-5 and between 78-8 and 78-10. Likewise, gradients in impedance phase in Figure 29 at the same locations at mid to high frequencies are further responses to the same structures.

Again referring to Figure 29, high apparent resistivities, often exceeding 1000 Ω-m are observed for the mountain soundings east of and including station 77-13; a maximum in the contour values is reached at mid frequencies (0.3 Hz). The impedance phase contours of Figure 29, somewhat less featured over the mountains than those of the apparent resistivity, undergo a minimum near 20° at upper-central frequencies (~ 3 Hz) and a maximum of almost 70° at lower frequencies (~ 0.01 Hz).

The computed ρ_{xy} and ϕ_{yx} pseudosections pertinent to line B-B' appear in Figure 30. About all that needs to be said about this is that the computed (Figure 30) and observed (Figure 29) pseudosections for this line agree within data scatter almost everywhere.

The complicated finite element cross section representing resistivity structure beneath line B-B' appears in Figure 31. The section as we show it in this diagram extends to a depth of only about 3 km although the measurements are sensitive to resistivity structure to depths in excess of 100 km. Figure 31 details just the lateral inhomogeneities beneath B-B' that appear to be affecting these particular measurements; below 2 km a layered regional profile which is common to both lines B-B' and C-C' appears to be the only resolvable geoelectric structure. This layered regional profile will be

Figure 30. Computed apparent resistivity and impedance phase pseuodsections for model finite element section for profile B-B' of Figure 24. Contours as in Figure 28 (after Wannamaker et al., 1980).

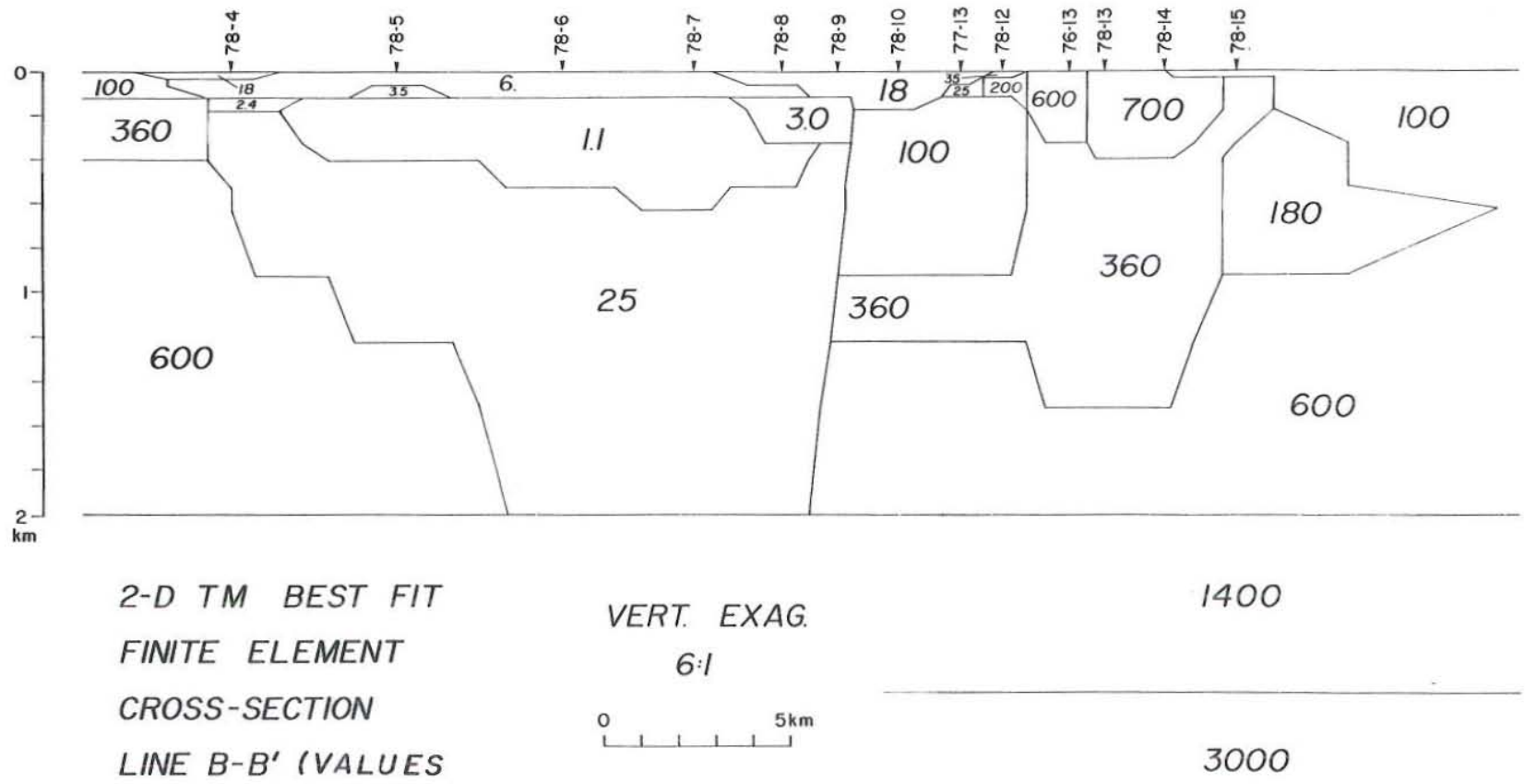

Figure 31. Best 2-D TM finite element section fitting the observations for profile B-B' of Figure 24. Values of individual media are in Ω-m. Vertical exaggeration is 6:1 (after Wannamaker et al., 1980).

discussed later in this report but for now we examine solely the upper-level multidimensional resistivity makeup.

A major feature of the cross section of Figure 31 is one of low to modest resistivity extending about 17 km west of site 78-9. It corresponds to a sequence of conductive sediments which occupy the Milford Valley. The resistivities of units within 140 m of the surface range from 3.5 to 18 Ω-m and with depth pass into a low resistivity medium of 1.1 Ω-m to a maximum depth of around 650 m beneath station 78-7. Deeper still lies a great thickness (>1 km) of modest resistivity material (25 Ω-m) although the depth extent of this material is poorly resolved. This group of media beneath the valley soundings is interpreted as being bounded on its western and eastern margins by steeply dipping interfaces. Though the actual dips are not well resolved, particularly for the western margin, a dip greater than 60° to the west is favored for the eastern limit.

Line C-C': The major characteristics peculiar to the pseudosections of line C-C' are seen for soundings directly over the thermal area nearby to the east of the margin of the Milford Valley sediments. For the higher frequencies about 30 Hz, the apparent resistivities of stations 76-3, 76-4 and 78-51 of Figure 32 are modest to low in amplitude and descend with decreasing frequency. The impedance phase pseudosection, exhibiting some relief in this frequency range, takes on values that overall are greater than 45°. However, in the frequency interval 10 to 1 Hz for these three sites, the apparent resistivities are now rising relatively very rapidly as frequency diminishes while the impedance phase values are below 10°. It has been our experience that such MT function behavior often is indicative of a resistive body at depth. We have paid special attention to attempting to fit this data with our

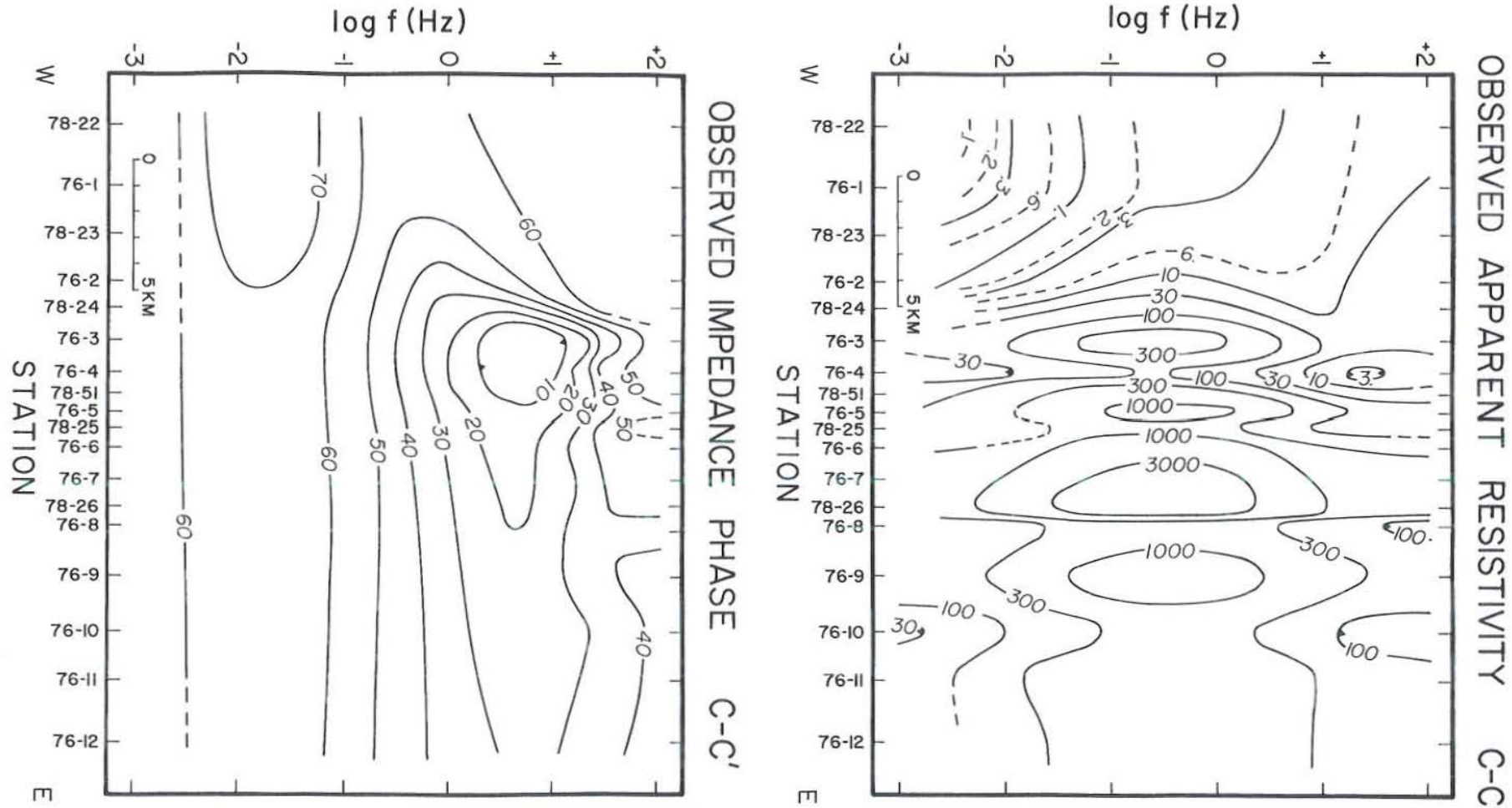

Figure 32. Observed apparent resistivity and impedance phase pseudosections for profile C-C' of Figure 24. Contours as in Figure 28 (after Wannamaker et al., 1980).

2D TM program since such resistive structure beneath the thermal area would have controversial geological ramifications. Below 1 Hz, the shapes of the individual apparent resistivity curves and values of impedance phase are essentially the same as those of soundings on line B-B' which are equivalent distances to the east of the bulk of the Milford Valley sediments.

The computed pseudosection for line C-C' shown in Figure 33 matches the observed pseudosection of Figure 32 reasonably well, but some difficulties with stations 76-3, 76-4 and 78-51 directly beneath the thermal area have been encountered. For these three sites, impedance phases below 10° could not be achieved for the computed results between 10 and 1 Hz, in fact they do not fall far below 20°, unless unrealistic subsurface geoelectric structure is invoked. Furthermore, the calculated apparent resistivities here below 10 Hz could not be made as large as those observed.

The same basic structure as on line B-B' is seen for the finite element cross section for line C-C' in Figure 34, except of course for some features peculiar to the thermal anomaly area of Figure 1. The resistivities of units within 200 m of the surface beneath the valley stations of C-C' range from 6 to 40 Ω-m and as well as for line B-B' pass into lower resistivity material of 1.1 to 2.2 Ω-m to a maximum depth of around 650 m beneath station 78-22. Also, a modest resistivity medium (25 Ω-m) appears to exist at yet greater depth to at least 2 km. It should be mentioned now that the westernmost limit of this conductive series of valley sediments on line C-C' of Figure 34, some 6 km west of station 78-22, is not resolved by our MT measurements but instead is constrained by gravity data and seismic refraction modeling (Carter and Cook, 1978; Gertson and Smith, 1979). Shifting this margin by ±2 km in an east-west sense from its present depiction appears to have no significant

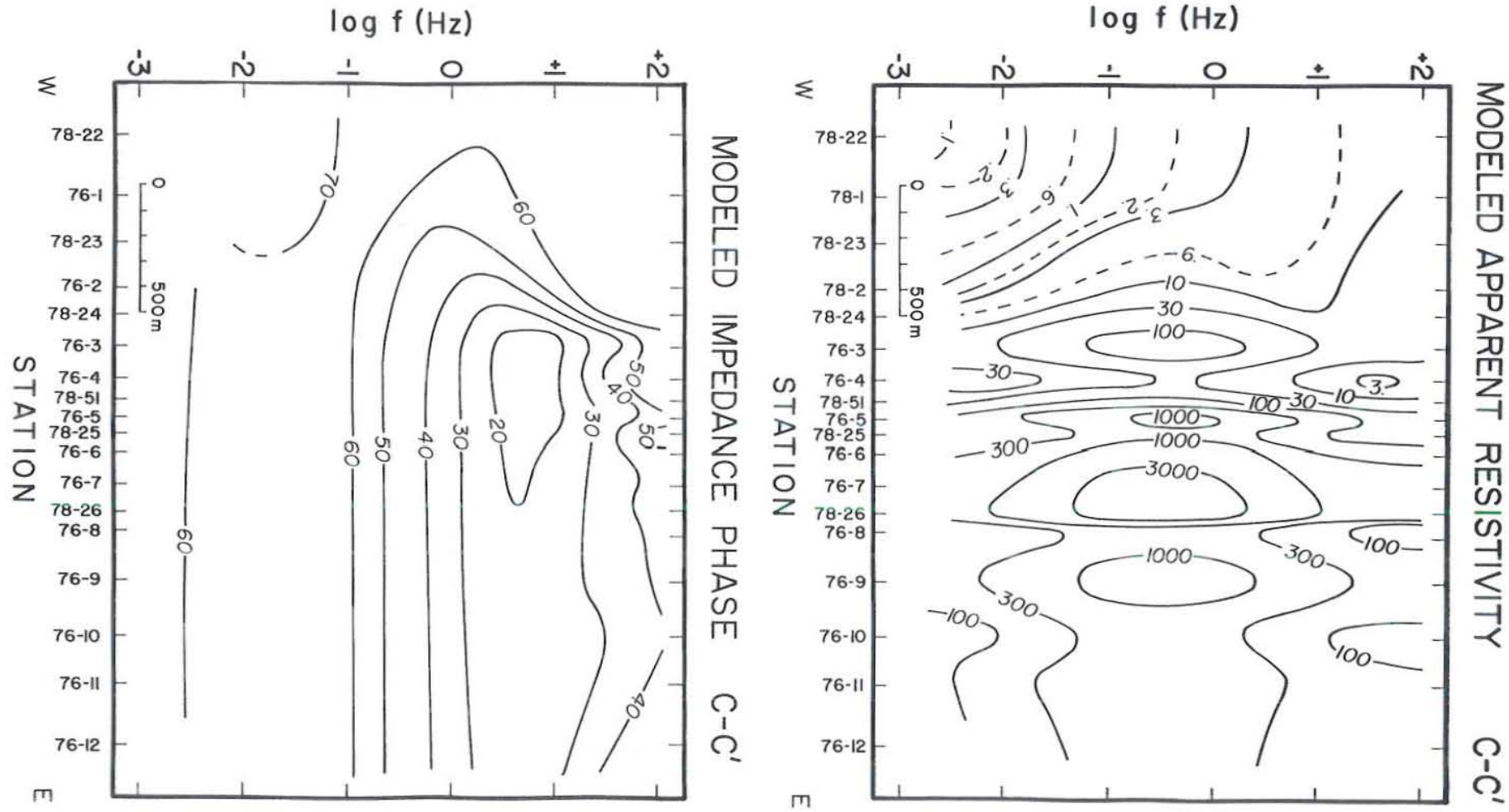

Figure 33. Computed apparent resistivity and impedance phase pseudosections for model finite element section for profile C-C' of Figure 24. Contours as in Figure 28 (after Wannamaker et al., 1980).

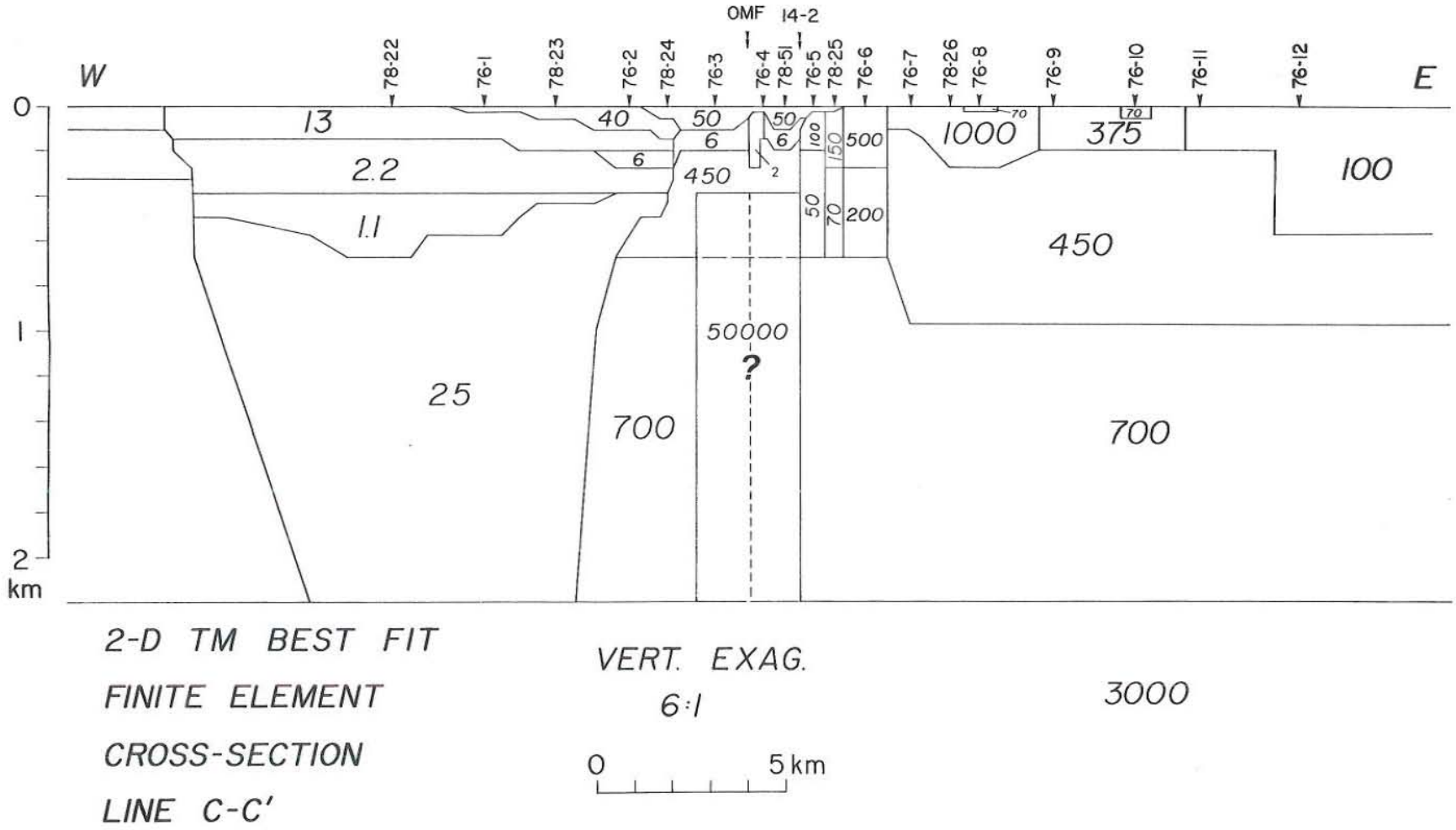

Figure 34. Best-fit 2-D TM finite element section fitting the observations for profile C-C' of Figure 24. Conventions as in Figure 30 (after Wannamaker et al., 1980).

effect upon the calculated MT values. Concerning the eastward margin of this conductive series, the somewhat less steep gradient in observed ρ_{yx} and ϕ_{yx} contours between sites 78-23 and 78-24 of Figure 32 than between sites 78-9 and 78-10 of Figure 29 implies the less abrupt, somewhat stepped transition in Figure 34 between the more conductive material of the Milford Valley and the relatively resistive material beneath much of the thermal area and Mineral Mountains.

Values of intrinsic resistivity in the hundreds of Ω-m in the upper 2 km or so are also seen beneath the mountains sites of line C-C'. The medium of 3000 Ω-m below 2.2 km heralds the onset of the 1D regional profile below C-C'. It is emphasized at this time that the regional resistivity layering below 2-3 km is common to both lines C-C' and B-B' and provides equally excellent fits to the observations of both lines, this being a reassuring circumstance.

As stated earlier, line C-C' straddles the thermal anomaly area as shown in Figure 24 and the major justification for this MT survey is the possible delineation of resistivity structure, perhaps relating to an economic brine reservoir or a deep-seated heat source driving the convective system, beneath this thermal area. Stations 76-3, 76-4 and 78-51 of Figure 24 were occupied directly over the thermal anomaly and the Opal Mound Fault, the latter denoted by OMF in Figure 34. In the upper 300 m of the finite element section, the resistivity progresses downward from 50 Ω-m material of 100 m maximum thickness through more conductive units (2-6 Ω-m) into a resistive medium of 450 Ω-m. This interval of the cross section is determined primarily by observations at frequencies greater than 10 Hz. The limits to the small volume of least resistivity (2 Ω-m) beneath station 76-4 are not resolvable

with the MT measurements since they are measurably affecting only the data of site 76-4. Instead, this unit was defined in conjunction with DC resistivity and controlled source audiomagnetotelluric measurements (Ward et al., 1978; Sandberg and Hohmann, 1982) in order to fit the observations at station 76-4.

The usefulness of small-scale electrical and electromagnetic surveys in detailing the shallow, low resistivity volume of earth beneath the thermal area should be stressed. The average MT station spacing across the thermal area on line C-C' is about 1 km. While being a rather high density compared to other MT surveys, this average spacing is inadequate to sample the complicated MT response over the thermal area, particularly the variable hydrothermal alteration centered near the Opal Mound Fault. Some model uniqueness problems can be avoided if control on the near-surface resistivity structure can be obtained. CSAMT especially appears to be a rapid, inexpensive means of gaining such control and the good agreement between interpreted geoelectric cross sections in this area for the measurements of Sandberg and Hohmann (1982) and our study points out how complimentary to MT is this active source technique. It turns out in addition that our MT cross section in Figure 34 in the upper 300 m agrees satisfactorily with those of Ward and Sill (1976) and Tripp et al. (1978) for dipole-dipole surveys in this area. Three independent electrical methods give similar estimates of the resistivity structure within 300 m of the surface so that we have confidence that the true, natural structure here bears a strong resemblance to that shown in Figure 34.

If one continues downward in this area of the figure one encounters a highly resistive (50,000 Ω-m) prism at a depth of 400 m. The width of this feature is 3 km and it extends to a depth of 2.2 km. The frequency range over

which MT supplies information on the depth and intrinsic resistivity of this prism appears to be around 1 to 10 Hz. Recall from earlier discussion that over this frequency interval the observed impedance phase is some 10° less than the computed and that below 10 Hz, the modeled apparent resistivity could not be made as large as the observed. The lack of fit of calculated to observed data is believed to be a 3D effect, and we do not maintain that the model 50000 Ω-m unit represents true buried structure.

We note briefly from the calculated resistivity cross sections that the data do not appear to detect lateral resistivity inhomogeneities existing below a depth of 2-3 km for either line B-B' or C-C'. In other words, ρ_{yx} and ϕ_{yx} for these lines are not sensitive to the presence of any large, lateral resistivity contrasts which may be associated with a deep-seated, perhaps partially molten heat source that drives the convective system.

4.2.4 Regional Conductivity Profile

It was mentioned earlier that below 2 km, only a layered earth model was required to fit all of the data for lines B-B' and C-C' of Figure 24.

Our best-fit, crust and upper mantle resistivity profile is reproduced in Figure 35 along with estimates of bulk resistivity vs. depth for relevant earth materials based upon laboratory experiments and an assumed conductive geotherm. Aqueous electrolytic conduction in rock pores and fractures, solid-state semiconduction in minerals and ionic conduction in partial melts all have domains of dominance comprising the entire deep resistivity section. The laboratory-derived resistivities must of course be considered as abstractions; given the oversimplifications upon which they were founded, especially the use of a conductive heat flow model in the actively extending eastern Great Basin, departures by our best-fit resistivity profile are inevitable. Such

Figure 35.- Best-fit, crust and upper mantle resistivity profile for southwestern Utah compared to physical model incorporating aqueous electrolytic conduction in rock pores, solid-state semiconduction in minerals and ionic conduction in partial melts, in conjunction with conductive geotherm assuming regional heat flow of 2.4 HFU (Lachenbruch and Sass, 1978; Chapman et al., 1981). Dotted crustal bounds use the aqueous electrolytic conduction measurements of Brace (1971) and the gabbro-plus-granite, solid-state data of Kariya and Shankland (1983). The line of dashes represents buffered olivine measurements of Duba and Heard (1980, and pers. comm.). The curve of dashes and dots corresponds to bulk resistivity of partially melted peridotite using the melt fraction determinations of Mysen and Kushiro (1977), Scarfe et al. (1978) and Wyllie (1979), the melt phase interconnection model of Waff and Bulau (1979) and the melt phase conductivity measurements on alkali olivine basalts of Rai and Manghnani (1978). Individual numbers of partial melting curve indicate percentage of liquid phase.

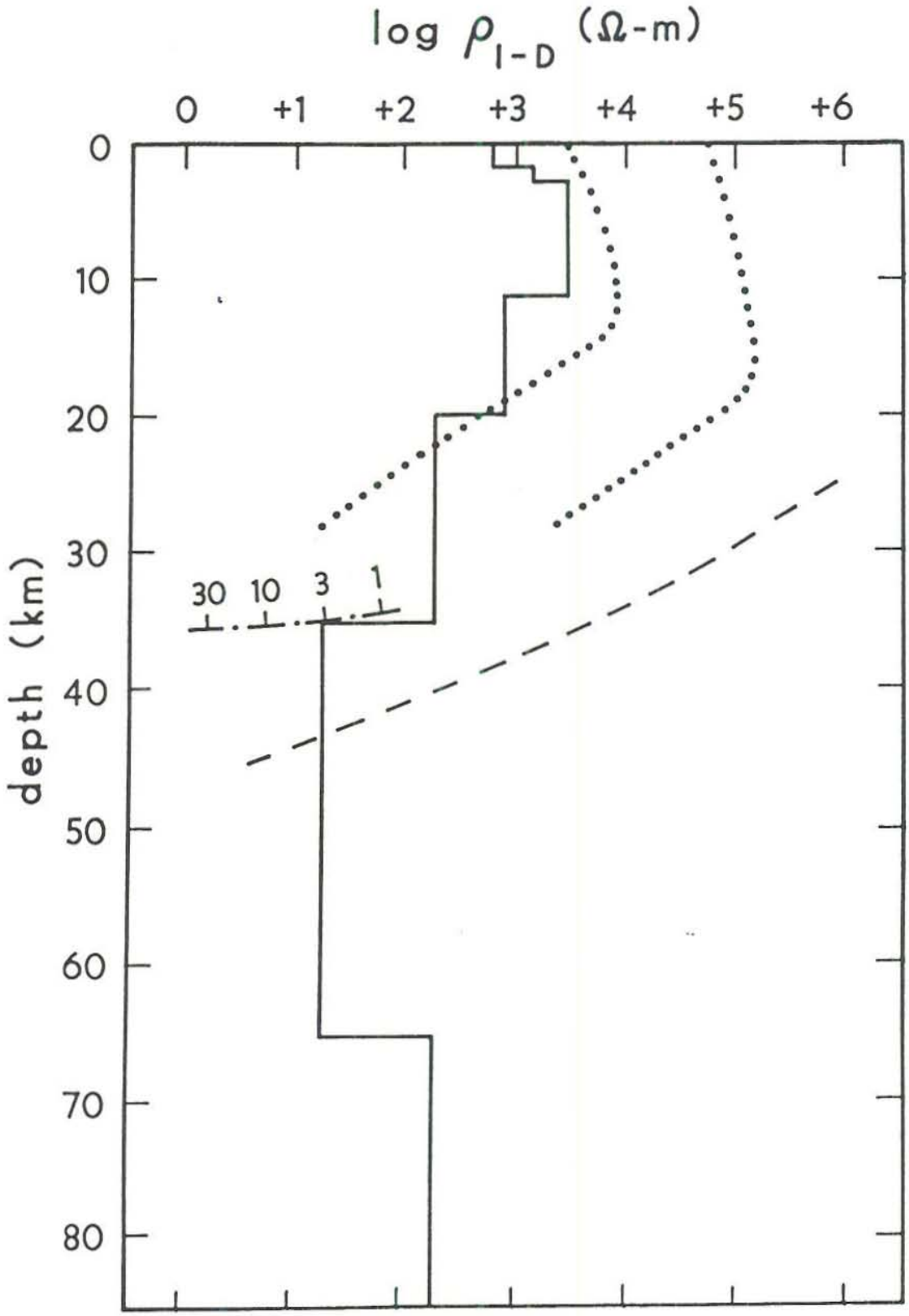
log ρ_{1-D} (Ω-m)
0
+1
+2
+3
+4
+5
+6
depth (km)
0
10
20
30
40
50
60
70
80
30
10
3
1

departures in fact are wholly desireable, since in their explanation lies the means for refining and strengthening our concepts of the physical state at depth in southwestern Utah.

Resistivities of our best-fit deep profile increase rather sharply from 600 to 3000 Ω-m over the depth interval 2 to 3 km. This high resistivity persists to depths exceeding 10 km. Bulk resistivity in these upper levels of the crust is controlled by aqueous electrolytic conduction in rock pores; for comparison with laboratory experiments, we have borrowed from Brace (1971) to construct the upper 10 to 15 km portion of the dotted curves in Figure 35. We note that Brace's resistivities have generally higher values and increase more gradually than do those of our best-fit model. However, in view of the significance of fracture porosity in the upper 2-3 km (Gertson and Smith, 1979; Yusas and Bruhn, 1979) and the uncertainties in electrolyte chemistry (Olhoeft, 1981; Shankland and Ander, 1982), we are not concerned by this disagreement. It is sufficient to conclude in light of Archie's Law that porosities at depths of several kilometers in this area are well under one percent.

From 11 to 35 km depth in Figure 35, our best-fit resistivity profile decreases in a steady manner from 3000 to 200 Ω-m. We have modeled this decline with layers due to the nature of our finite element algorithm, but we believe the actual variation with depth to be smooth. The dotted curves in this diagram representing laboratory investigations also decrease with depth below about 15 km. These curves were constructed from the compilation by Kariya and Shankland (1983) of semiconduction measurements on dry gabbroic and granitic rocks in conjunction with a conductive geotherm assuming a regional heat flow of 2.4 HFU (Lachenbruch and Sass, 1978; Chapman et al., 1981). The

depth to the base of the crust in this area is about 28 km, so it is here at which the dotted curves end. Although the resistivities derived from the laboratory work and the MT observations exhibit an approximate mutual resemblance, the finite element model shows somewhat lower values and a more gradual decrease of resistivity from the middle to the lower crust. Applying the results of Kariya and Shankland (1983), the resistivity model suggests that temperatures at depth, especially around 15-20 km, exceed those produced by our conductive heat flow model. On the other hand, a reduction of mid crustal resistivities by volatiles, either by pore conduction or through a solid-state mechanism, cannot be ruled out (Wannamaker et al., 1983).

The MT observations do not support the notion that temperatures at depth in the crust are high enough to create any widespread, layer-like, electrically conductive zone of interconnected silicic melt. Given the depletion of lower crustal water in the eastern Great Basin (Wannamaker et al., 1983), we believe temperatures exceeding 1000°C would be necessary to do this.

At depths greater than about 28 km, below the Moho in this area, resistivity mechanisms in mantle rocks must be considered. For comparison with our best-fit profile, the inclined curve of dashes in Figure 35 displays a hypothetical resistivity due to pure olivine with f_{O_2} between the magnetite-wustite iron-wustite buffers (Duba and Heard, 1980, and pers. comm.) and with temperature defined by our conductive geotherm. Resistivities of pure olivine with this geotherm decrease rapidly with depth, falling below 20 Ω-m by 45 km, but possess magnitudes in the depth interval 28 to 35 km that are much greater than the 200 Ω-m appearing here in our best-fit deep profile. It may well be that pure olivine is not a representative composition for determining bulk

solid-state resistivities here (Shankland, 1981); on the other hand, a very resistive layer occupying this narrow depth interval may be difficult to resolve with surface MT measurements (Madden, 1971).

Much more disagreeable to us, however, is the discrepancy between shapes of the hypothetical solid-state olivine curve and our best-fit resistivity profile. In an earth with temperatures that increase steadily with depth, such as is the case with our conductive geotherm or even with any of the temperature profiles of Lachenbruch and Sass (1978) which incorporate convective components, the Arrhenius solid-state temperature dependence for any rock results in bulk resistivities which decrease monotonically with depth. Indeed, the fact that activation energies for semiconduction in earth materials also increase with temperature (Duba et al., 1974; Olhoeft, 1979) means that bulk resistivity curves determined by solid-state mechanisms and steadily increasing geotherms do not flatten out with depth. A deep resistivity profile that decreased steadily with depth is rejected as a candidate to explain the low-frequency MT observations at the Roosevelt Hot Springs; the order-of-magnitude rise of resistivity in the upper mantle in our best-fit deep model is a strict requirement. Hence, unless substantial variations in bulk chemical composition with depth exist in the upper mantle of southwestern Utah, a solid-state resistivity mechanism alone is not sufficient to produce a deep resistivity structure resembling our best-fit profile.

We therefore look to partial melting as the cause of the 20 Ω-m deep layer. If our conductive geotherm is imposed, the curve of dots and dashes in Figure 35 arises as a conceptual variation of resistivity with depth due to an interconnected basaltic melt in upper mantle peridotite. Given the presumably

unimportant effects of volatiles upon Late Cenozoic basalt production in the eastern Great Basin (Wannamaker et al., 1983), we derive this curve using the dry peridotite solidus presented by Wyllie (1979), the nearly invariant nature of basalt generation demonstrated by Mysen and Kushiro (1977) and Scarfe et al. (1978), the measurements of electrical conductivity of alkali-olivine basalt of Rai and Manghnani (1978) and the melt phase interconnection model of Waff and Bulau (1979). Individual numbers on the partial melting curve indicate percent liquid phase.

In Figure 35, the value of 20 Ω-m on the laboratory-based partial melt resistivity curve corresponds to a melt fraction of about 3%, but this is specific to the geotherm used. If the conductive temperature profile employed had been somewhat less steep, so that it intersected the solidus at a greater depth and temperature than shown, 20 Ω-m on the partial melting curve would arise from a melt fraction less than 3%. We simply conclude that the interconnected melt fraction in our deep, low resistivity layer is rather small, on the order of 2-3%. We do not discount the possibility that in extensional environments like the eastern Great Basin an unknown portion of the melt may reside in discrete vertical fissures to which our measurements are not sensitive.

On the basis of the MT measurements alone, we cannot exclude easily the possibility that the top of our model low-resistivity layer is as shallow as 28 km, i.e., is at the base of the crust in this area, although we expressed disfavor earlier with the top being at only 25 km. In any event, impressing dry peridotite solidus temperatures at the Moho would lead to rampant melting in the crust above. This would surely be detectable by our MT soundings, but is not.

We have not defined the laboratory-derived curve in Figure 35 beyond melt fractions of about 30% since further melting in most peridotite will not be nearly invariant. Even so, continuation of the conductive geotherm would yield yet greater melt fractions and lower bulk resistivities. Such extreme melt fractions alone condemn the purely conductive geotherm as inaccurate to arbitrarily great depth. Furthermore, the 20 Ω-m material in our best-fit deep profile is a discrete layer, and not an infinitely extending basal half-space. Supported by the approximately invariant, water-deficient character of Late Cenozoic basalt production in the eastern Great Basin, we conclude from the MT interpretation that the dry peridotite solidus is a representative P-T trajectory for the depth interval 35 to at least 65 km of the 20 Ω-m layer below S.W. Utah.

While we have not repeated them here, Wannamaker et al. (1983), have carried out numerous sensitivity tests to establish that the conductivity profile of Figure 35 is unlikely to be significantly in error. In an attempt to learn of the relationship of the partial melt in the upper mantle to the geothermal system at Roosevelt Hot Springs, we are conducting further MT soundings and interpretation.

5.0 CONCLUSIONS

Because of high unit costs for MT/AMT surveying, the method is probably best suited to delineation of major crustal layering, to detection of magma chambers, and to detection of partial melts in the deep crust or upper mantle. Controlled source methods, because of lower costs and higher lateral resolution are more suited to delineation of near-surface fractures, faults, and zones of hydrothermal alteration.

Ward et al. (1981) in commenting on its use in the Basin and Range Province, U.S.A. note that,

"If one were to accept [industrial application of MT in geothermal exploration] at face value, then the MT method would be recommended for use in hydrothermal system exploration due to its advertised attributes of great depth of exploration and ability to detect the hot rock source of heat at depths of several tens of kilometers. Unfortunately, neither of these attributes is necessarily correct. In a three dimensionally inhomogeneous earth, one's ability to predict the distribution of resistivities at depth is severely limited by the influence of surficial conductors such as alluvial fill or shallow alteration zones (Wannamaker et al, 1978). That a hot rock, when molten, is necessarily [highly conducting] must be conjectural, for conductivity in magma at elevated temperature is dependent upon the partial pressure of water (Lebedev and Khitarov, 1964). Hot dry rocks are good insulators almost by definition. If one uses only the standard one or even two dimensional MT interpretation methods when dealing with a three dimensional earth, then one has no assurance that the method is capable of detecting a hot rock source by means of its assumed high conductivity. Means for surmounting this latter problem are evident (Wannamaker et al, 1980, 1982,

1983; Newman et al., 1983) but are seldom applied. Accordingly, we do not recommend using the MT method until late in the exploration sequence when one is justified in applying the higher cost techniques. The poor lateral [definition afforded by normal MT data at 0.5 km to 1.0 km site separations] does not make the method well-suited for siting a drill hole to intersect a given structure in the advanced stage of exploration, but it may be used effectively by a consortium of companies for early reconnaissance evaluation of a region."

In this article we have concentrated on the fundamentals and problems of the MT/AMT method, with only one integrated field case history presented. For similar integrated case histories, the reader is referred to the literature cited in the introduction.

6.0 ACKNOWLEDGEMENTS

Preparation of this report was stimulated by an invitation to one of us (S. H. Ward) to present lectures on this and other material to the United Nations University Program on Geothermal Energy in Reykjavik, Iceland. This latter program is operated by Orkustofnun (The National Energy Authority of Iceland). S. H. Ward is indebted to Dr. Ingvar Birgir Fridleifsson for the opportunity to present this material to the U. N. Fellows and to Orkustofnun personnel during late September, 1982.

Most of the material is based on studies originally funded by the U.S. Department of Energy under contract DE-AC07-80ID12079.

Joan Pingree typed the manuscript, Doris Cullen and Sandra Bromley supervised preparation of the illustrations, while Carl Ruscetta provided technical editing; we are indebted to all of them. We also wish to thank the Earth Science Laboratory of the University of Utah Research Institute for assisting us in preparation of this manuscript.

REFERENCES

Aiken, C. L. V., and Ander, M. E., 1981, A regional strategy for geothermal exploration with emphasis on gravity and magnetotellurics: J. Volc. and Geotherm. Res., v. 9, p. 1-27.

Bannister, P. R., 1969, Source distance dependence of the surface-impedance conductivity measurement technique: Geophysics, v. 34, p. 785-788.

Berktold, A., 1982, Electromagnetic studies in geothermal regions: Proc. 6th Workshop on Electromagnetic Induction in the Earth and Moon, Dept. Physics, Univ. of Victoria, Canada.

Berktold, A., and Kemmerle, K., 1982, Distribution of electrical conductivity in the Urach geothermal area, a magnetotelluric and geomagnetic depth sounding investigation, The Urach Geothermal Project: Stuttgart, E. Schweizerdort'sche Verlagsbuchhandling, p. 289-300.

Bleil, D. F., *ed.*, 1964, Natural electromagnetic phenomena below 30 kc/s: New York, Plenum Press.

Boehl, J. E, Bostick, F. X., Jr., and Smith, H. W., 1977, An application of the Hilbert transform to the magnetotelluric method: Elec. Geop. Res. Lab. Rep., Univ. of Texas at Austin, 98 p.

Bostick, F. X., Jr. and Smith, H. W., 1962, Investigation of large-scale inhomogeneities in the earth by the magnetotelluric method: Proc. I.R.E., v. 50, p. 2339-2346.

Bostick, F. X., Jr., 1977, A simple almost exact method of MT analysis: *in* S. H. Ward, ed., Workshop on Electrical Methods in Geothermal Exploration, U.S.G.S Contract 14-08-0001-G-359, p. 174-183.

Brace, W. F., 1971, Resistivity of saturated crustal rocks to 40 km. based on laboratory measurements: *in* J. G. Heacock, ed., The Structure and Physical Properties of the Earth's Crust, AGU Monograph 14, p. 243-256.

Cagniard, L., 1953, Basic theory of the magnetotelluric method of geophysical prospecting: Geophysics, v. 18, p. 605.

Campbell, W. H., 1967, Geomagnetic pulsations, *in* S. Matsushita, and W. H. Campbell, eds., Physics of geomagnetic phenomena: New York, Academic Press, p. 822-890.

Cantwell, T., 1960, Detection and analysis of low-frequency magnetotelluric signals: Ph.D. thesis, MIT.

Carter, J. A., and Cook, K. L., 1978, Regional gravity and aeromagnetic surveys of the Mineral Mountains and vicinity, Millard and Beaver Counties, Utah: DOE/DGE Final Report, Univ. of Utah, 77-11, 178 p.

Chapman, D. S., Clement, M. D., and Mase, C. W., 1981, Thermal regime of the Escalante Desert, Utah with an analysis of the Newcastle geothermal system: J. Geop. Res., 86(B12), p. 11735-11746.

Dmitriev, V. I., and Berdichevsky, M. N., 1979, The fundamental model of magnetotelluric sounding: Proc. of the IEEE, 67(7), p. 1034-1044.

Duba, A., Heard, H. C., and Schock, R. N., 1974, Electrical conductivity of olivine at high pressure and under controlled oxygen fugacity: J. Geophys. Res., 79, p. 1667-1673.

Duba, A. G., and Heard, H. C., 1980, Effect of hydration on the electrical conductivity of olivine: EOS Transactions, 61(17), p. 404.

Dupis, A. and Iliceto, V., 1974, An example of rapid magnetotelluric investigation of faulted structures: the Carboli area (Lardarello, Italy): Boll. di Geofis. Teorica ed Applicata, v. 16, p. 125-136.

Dupis, A., Iliceto, V., and Norinelli, A., 1974, First magnetotelluric measurements on Lardarello site: Boll. di Geofis. Teorica ed Applicata, v. 16, p. 137-152.

Dupis, A., Marie, Ph., and Petian, G., 1980, Magnetotelluric prospecting of the Mont Dore area: Advances in European Geothermal Research, D. Reidel, Dordrecht, Holland, p. 935-943.

Earll, F. N., 1957, Geology of the central Mineral Range, Beaver Co., Utah: PhD thesis, Univ. Utah, 112 p.

Gamble, T. D., Goubau, W. M., and Clarke, J., 1979a, Magnetotellurics with a remote reference: Geophysics, v. 44(1), p. 53-68.

Gamble, T. D., Goubau, W. M., and Clarke, J., 1979b, Error analysis for remote reference magnetotellurics: Geophysics, v. 44, p. 959-968.

Gamble, F. D., Goubau, W. M., Goldstein, N. E., and Clarke, J., 1980, Referenced magnetotellurics at Cerro Prieto: Geothermics, v. 9, p. 49-63.

Gertson, R. C., and Smith, R. B., 1979, Interpretation of a seismic refraction profile across the Roosevelt Hot Springs, Utah and vicinity: DOE/DGE Topical Report 78-1701.a.3., Univ. of Utah, 116 p.

Goldstein, H. F., Mozley, E., Gamble, T. D., and Morrison, H. F., 1978, Magnetotelluric investigations at Mt. Hood, Oregon: Trans. Geotherm. Resour. Counc., v. 2, p. 219-221.

Goldstein, H. F., Mozley, E., and Wilt, M., 1982, Interpretation of shallow electrical features from electromagnetic and magnetotelluric surveys at Mount Hood, Oregon: Jour. Geophys. Res., v. 87, p. 2815-2828.

Goubau, W. M., Gamble, T. D., and Clarke, J., 1978, Magnetotelluric data analysis: removal of bias: Geophysics, v. 43, p. 1157-1166.

Hermance, J. F., and Pedersen, J., 1977, Assessing the geothermal resource base of the southwestern U.S. status report of a regional geoelectromagnetic traverse: Geophysics, v. 42, p. 155-156.

Hermance, J. F., Thayer, R. E., Bjornsson, A., 1975, The telluric-magnetotelluric method in the regional assessment of geothermal potential: Second U.N. Symp. on the Development and Use of Geothermal Resources, Proc. v. 2, p. 1037-1048.

Hermance, J. F., and Peltier, W. R., 1970, Magnetotelluric fields of a line current: J. Geophys. Res., v. 75, p. 3351-3356.

Hoover, D. B., Long, C. L., and Senterfit, R. M., 1978, Audiomagnetotelluric investigations in geothermal areas: Geophysics, v. 43, p. 1511-1514.

Hoover, D. B., Frischknecht, F. C., and Tippens, C., 1976, Audio-magnetotelluric soundings as a reconnaissance exploration technique in Long Valley, Calif.: J. Geophys. Res., v. 81, p. 801-809.

Hoover, D. B., and Long, C. L., 1975, Audio-magnetotelluric methods in reconnaissance geothermal exploration: Proc. 2nd U. N. Sympos. Devel. Geothermal Resources, p. 1059-1064.

Hutton, V. R. S., Dawes, G. J. K., Devlin, T., and Roberts, R., 1982, Magnetotelluric and magnetovariational studies in the Travale geothermal field: Report for the Commission of the European Communities, Directorate General for Science, Research, and Development.

Isherwood, W. R. and Mabey, D. R., 1978, Evaluation of Baltazor known geothermal resources area, Nevada: Geothermics, v. 7, p. 221-229.

Jackson, D. B., and O'Donnell, J. E., 1980, Reconnaissance electrical surveys in the Coso Range, California: J. Geophys. Res., v. 85, p. 2502-2516.

Jacobs, J. A., 1970, Geomagnetic Micropulsations: Berlin, Springer-Verlag, 179p.

Jiracek, G. R., Mitchell, P. S., and Gustofson, 1982, Two-dimensional magnetotelluric modeling of the Rio Grande Rift, abstract: *in*, Proc. Sixth Workshop on Electromagnetic Induction in the Earth and Moon, Dept. of Physics, University of Victoria.

Jones, F. W., and Vozoff, K., 1978, The calculation of magnetotelluric quantities for three-dimensional conductivity inhomogeneities: Geophysics, v. 43, p. 1167-1175.

Jupp, D. L. B., and Vozoff, K., 1975, Stable iterative methods for inversion of geophysical data: Geophys. J. Roy. Astr. Soc., v. 42, p. 957-976.

Jupp, D. L. B., and Vozoff, K., 1977, Two-dimensional magnetotelluric inversion: Geophys. J. R. Astr. Soc., 050, p. 333-352.

Kariya, K. A., and Shankland, T. J., 1983, Interpretation of electrical conductivity of the lower crust: Geophysics, 48(1), p. 52-61.

Keller, G. V., 1970, Inductive methods in prospecting for hot water: Geothermics, Spec. iss. 2, p. 318-332.

Keller, G. V., and Rapolla, A., 1974, Induction methods in prospecting for hot water: Developments in Solid Earth Geophysics, Netherlands, v. 6, p. 133-166.

Ku, C. C., Hsieh, M. S., and Lim, S. H., 1973, The topographic effect in electromagnetic fields: Can. J. Earth Sci., 10, p. 645-656.

Kunetz, G., 1972, Processing and interpretation of magnetotelluric soundings: Geophysics, 37, p. 1005-1021.

Lachenbruch, A. H., and Sass, J. H., 1978, Models of an extending lithosphere and heat flow in the Basin and Range province: *in* R. B. Smith and G. P. Eaton, eds., Geol. Soc. Am. Mem. 152, p. 209-250.

Larsen, J. C., 1981, A new technique for layered earth magnetotelluric inversion: Geophysics, v. 46, p. 1247-1257.

Lebedev, E. B., and Khitarov, N. I., 1964, Dependence on the beginning of melting of granite and the electrical conductivity of its melt on high water vapor pressure: Geokhimiya, 3, p. 195-201.

Lipman, P. W., et al., 1978, Pleistocene rhyolite of the Mineral Mountains, Utah, geothermal and archeological significance: U.S. Geol. Survey Jour. Research, v. 6, p. 133-147.

Long, C. L., and Kaufman, H. E., 1980, Reconnaissance geophysics of a known geothermal resource area, Weiser, Idaho, and Vale, Oregon: Geophysics, v. 45, p. 312-322.

Mabey, D. R., et al, 1978, Regional magnetic patterns in part of the Cordillera in the western United States, *in* R. B. Smith and G. P. Eaton, eds., Cenozoic tectonics and regional geophysics of the western Cordillera: Geol. Soc. America Mem. 152, p. 313-340.

Madden, T. R., and Nelson, P. H., 1964, A defense of Cagniard's magnetotelluric method: ONR report project NR-371-401, Geophys. Lab., Massachusetts Inst. of Technology.

Madden, T. R., 1971, The resolving power of geoelectric measurements for delineating resistive zones within the crust, *in* J. G. Heacock, ed., The Structure and Physical Properties of the Earth's Crust: AGU Monograph 14, p. 95-105.

Martinez, M., Fabrial, H., and Romo, J. M., 1982, Magnetotelluric studies in the geothermal area of Culiacan, Mexico: Sixth Workshop on Electromagnetic Induction in the Earth and Moon, IAGA., Victoria, British Columbia, Dept. of Physics, Univ. of Victoria (abstract).

Matsushita, S., and Campbell, W. H., eds., 1967, Geophysics and geomagnetic phenomena: New York, Academic Press, 1398 p.

Morrison, H. F., Lee, K. H., Oppliger, G., and Dey, A., 1979, Magnetotelluric studies in Grass Valley, Nevada: Univ. Calif. Berkeley, Lawrence Berkeley Lab., Report. LBL-8646 (UC-66b), 50 p.

Musmann, G., Gramkow, B., Lohr, V., and Kertz, W., 1980, Magnetotelluric survey of the Lake Laach (Eifel) volcanic area: Advances in European Geothermal Research: D. Reidel Co., Dordrecht, Holland, p. 904-910.

Mysen, B. O., and Kushiro, I., 1977, Compositional variations of coexisting phases with degree of melting of peridotite in the upper mantle: Am. Min., 62, p. 843-865.

Nabetani, S., and Rankin, D., 1969, An inverse method of magnetotelluric analysis of a multilayered earth: Geophysics, v. 34, p. 75-86.

Neves, A. S., 1957, The magneto-telluric method in two-dimensional structures: Dept. Geol. and Geophys., M.I.T., Ph.D. thesis.

Newman, G. H., Wannamaker, P. E., and Hohmann, G. W., 1983, A two- and three-dimensional magnetotelluric model study with emphasis on the detection of magma chambers in the Basin and Range: Report in preparation, Earth Science Laboratory, University of Utah Research Institute.

Ngoc, P. V., 1980, Magnetotelluric survey of the Mount Meager region of the Squamish Valley (British Columbia): Rpt. of the Geomagnetic Service of Canada, Earth Physics Section, Dept. of Energy, Mines, & Resources, Ottawa, 26 p.

Nielson, D. L., Sibbett, B. S., McKinney, D. B., Hulen, J. B., Moore, J. N., and Samberg, S. M., 1978, Geology of Roosevelt Hot Springs KGRA, Beaver County, Utah: Univ. Utah Research Inst., Earth Science Lab. Rept. 12, 121 p.

Nielson, D. L., Sibbett, B. S., and McKinney, D. B., 1979, Geology and structural control of the geothermal system at Roosevelt Hot Springs, Beaver County, Utah (abs.): AAPG Bull., v. 63, p. 836.

Nutter, C., 1981, MT2D: An interactive two-dimensional magnetotelluric and line source program: Earth Science Laboratory Report DOE/ID/12079-31, 51 p.

Oldenburg, D. W., 1979, One-dimensional inversion of natural source magnetotelluric observations: Geophysics, v. 44, p. 1218-1244.

Olhoeft, G. R., 1979, Electrical conductivity from 200 to 1000°C for 264 rocks and minerals from data in Parkhomenko and Bondarenko, 1972: U.S.G.S. Open File Rep. 79-846, 23 p.

Olhoeft, G. R., 1981, Electrical properties of granite with implications for the lower crust: J. Geophys. Res. 86, p. 931-936.

Parker, R. L., and Whaler, K. A., 1981, Numerical methods of establishing solutions to the inverse problem of electromagnetic induction: Jour. Geophys. Res., v. 86, no. B10, p. 9574-9584.

Pascoe, L. D., and Jones, F. W., 1972, Boundary conditions and calculation of surface values for the general two-dimensional electromagnetic induction problem: Geophys. J. Roy. Astr. Soc., v. 27, p. 179.

Patella, D., 1976, Interpretation of magnetotelluric resistivity and phase soundings over horizontal layers: Geophysics, v. 41, p. 96-105.

Patrick, F. W., and Bostick, F. X., Jr., 1969, Magnetotelluric modeling techniques: EERL, Univ. Texas, Tech. Rep. No. 59.

Peltier, W. R., and Hermance, J. F., 1971, Magnetotelluric fields of a Gaussian electrojet: Canadian Jour. of Earth Sci., v. 8, p. 338-346.

Petrick, W. R., Pelton, W. H., and Ward, S. H., 1977, Ridge regression inversion applied to crustal resistivity sounding data from South Africa: Geophysics, v. 42, p. 995-1005.

Rai, C. S., and Manghnani, M. H., 1978, Electrical conductivity of basalts to 1550°C: *in* Proceedings of Chapman Conference on Partial Melting in the Earth's Upper Mantle, ed. by H. J. B. Dick: Oreg. Dept. Geol. Min. Ind., Bull. 96, p. 219-232.

Ranganayaki, R. P. and Madden, T. R., 1980, Generalized thin sheet analysis in magnetotellurics: an extension of Price's analysis: Geophys. J. Roy. Astr. Soc., v. 60, p. 445-457.

Rijo, L., 1977, Modeling of electric and electromagnetic data: Ph.D. thesis, Dept. Geol. and Geophys., Univ. of Utah.

Ross, H. P., Nielson, D. L., and Moore, J. N., 1982, Roosevelt Hot Springs Geothermal System, Utah Case Study: Bull. A.A.P.G. v. 66, p. 879-902.

Sandberg, S. K., and Hohmann, G. W., 1982, Controlled-source audiomagnetotellurics in geothermal exploration: Geophysics, 47, p. 100-116.

Scarfe, C. M., Mysen, B. O., and Rai, C. S., 1978, Invariant melting of mantle material: partial melting of two lherzolite nodules: Yearbook of the Carnegie Inst. of Washington, 78, p. 498-501.

Shankland, T. J., 1981, Electrical conduction in mantle minerals: *in* Evolution of the Earth, AGU Geodynamics Series, 5, p. 256-263.

Shankland, T. J., and Ander, M. E., 1982, Electrical conductivity, temperatures, and fluids in the lower crust: Los Alamos National Laboratory, unpublished manuscript.

Sibbett, B. S., and Nielson, D. L., 1980, Geology of the central Mineral Mountains, Beaver Co., Utah: Univ. Utah Research Inst., Earth Science Lab. Rept. 33, 42 p.

Sims, W. E., Bostick, F. X., Jr., and Smith, H. W., 1971, The estimation of magnetotelluric impedance elements from measured data: Geophysics, v. 36, p. 938-942.

Sims, W. E., and Bostick, F. X., Jr., 1969, Methods of magnetotelluric analysis: Electrical Geophysics Research Laboratory, Univ. Texas, Austin, Rep. 58, 86 p.

Smith, R. B., and Sbar, M., 1974, Contemporary tectonics and seismicity of the western states with emphasis on the Intermountain seismic belt: Geol. Soc. America Bull., v. 85, p. 1205-1218.

Smith, R. L., and Shaw, H. R., 1975, Igenous-related geothermal systems, *in* D. E. White and D. L. Williams, eds., Assessment of geothermal resources of the United States: U.S. Geol. Survey Circ. 726, p. 58-83.

Srivastava, S. P., 1967, Magnetotelluric two- and three-layer master curves: Dom. Obs. Publ., v. 35, no. 7, Canada Dept. of Energy Mines and Resources, Ottawa.

Stanley, W. D., 1982, Magnetotelluric soundings on the Idaho National engineering laboratory facility, Idaho: J. Geophys. Res., v. 87, p. 2683-2691.

Stanley, W. D., Boehl, J. E., Bostick, F. X., Jr. and Smith, H. W., 1977, Geothermal significance of magnetotelluric sounding in the eastern Snake River Plain - Yellowstone region: J. Geophys. Res., v. 82, p. 2501-2514.

Sternberg, B. K., Buller, P. L., Kisabeth, J. S., and Mehreteab, E., 1982, Electrical Methods for Hydrocarbon Exploration: II. Magnetotelluric (MT) Method: Proc. Symposium on "Unconventional Methods in Exploration for Petroleum and Natural Gas: Dallas, Texas, Southern Methodist University, (September).

Stodt, J. A., 1978, Documentation of a finite element program for solution of geophysical problems governed by the inhomogeneous scalar or Helmholtz equation: NSF Program Listing and Documentation, Univ. of Utah, 66 p.

Stodt, J. A., 1983, Magnetotelluric Data Acquisition, Reduction, and Noise Analysis: Proc. Workshop on "Electrical Methods in Oil and Gas Exploration", Salt Lake City, Utah, Earth Science Laboratory, University of Utah Research Institute, (January).

Strangway, D. W., Swift, C. M., Jr., and Holmer, R. C., 1973, The application of audio-frequency magnetotellurics (AMT) to mineral exploration: Geophysics, v. 38, p. 1159-1175.

Strangway, D. W., and Vozoff, K., 1970, Mining exploration with natural electromagnetic fields: Econ. Geol. Rep. 26, Can. Geol. Surv., Ottawa, Ont., p. 109-112.

Stratton, J. A., 1941, Electromagnetic Theory, New York, McGraw-Hill Book Co. Inc., 616 p.

Swift, C. M., Jr., 1967, A magnetotelluric investigation of an electrical conductivity anomaly in the southwestern United States: Ph. D. thesis, MIT.

Tikhonov, A. V., 1950, Determination of the electrical characteristics of the deep strata of the earth's crust: Dokl. Akad. Nauk., v. 73, p. 295.

Ting, S. C., and Hohmann, G. S., 1981, Integral equation modeling of three-dimensional magnetotelluric response: Geophysics, v. 46, p. 182-197.

Tripp, A. C., Ward, S. H., Sill, W. R., Swift, C. M. Jr., and Petrick, W. R., 1978, Electromagnetic and Schlumberger resistivity sounding in the Roosevelt Hot Springs KGRA: Geophysics, v. 43, p. 1450-1469.

Vozoff, K., 1972, The magnetotelluric method in the exploration of sedimentary basins: Geophysics, v. 37, p. 98-141.

Waff, H. S., and Bulau, J. R., 1979, Equilibrium fluid distribution in an ultramafic partial melt under hydrostatic stress conditions: J. Geophys. Res., 84 p. 6109-6114.

Wait, J. R., 1962, Theory of magneto-telluric fields: J. Res. N.B.S., v. 66D, p. 509.

Wannamaker, P. E., 1978, Magnetotelluric investigations at Roosevelt Hot Springs and Mineral Mtns. area, Utah: Topical rep. 78-1701.a.6.1, DOE/DGE contract EY-78-S-07-1701, Univ. of Utah, 53 p.

Wannamaker, P. E., Ward, S. H., Hohmann, G. W., and Sill, W. R., 1980, Magnetotelluric models of the Roosevelt Hot Springs thermal area, Utah: Dept. Geol. and Geophys., Univ. Utah, Rep. DOE/ET/27002-8, 213 p.

Wannamaker, P. E., and Hohmann, G. W., 1982, Electromagnetic modeling of three-dimensional bodies in layered earths using integral equations: Earth Science Laboratory Rept. 64, Salt Lake City, 50 p.

Wannamaker, P. E., Ward, S. H., and Hohmann, G. W., 1982, Magnetotelluric responses of three-dimensional bodies in layered earths: Report DOE/ID/12079-87, Earth Science Laboratory, University of Utah Research Institute, 83 p.

Wannamaker, P. E., Ward, S. H., Hohmann, G. W., and Sill, W. R., 1983, Deep resistivity structure in S.W. Utah and its geothermal significance: ESL Report DOE/ID/12079-89, 95 p.

Wannamaker, P. E., 1983, Interpretation of Magnetotelluric Data: Proc. Workshop on "Electrical Methods in Oil and Gas Exploration", Salt Lake City, Utah, Earth Science Laboratory, University of Utah Research Institute, (January).

Ward, S. H., Parry, W. T., Nash, W. P., Sill, W. R., Cook, K. L., Smith, R. B., Chapman, D. S., Brown, F. H., Whelan, J. A., and Bowman, J. R., 1978, A summary of the geology, geochemistry and geophysics of the Roosevelt Hot Springs thermal area, Utah: Geophysics, 43, p. 1515-1542.

Ward, S. H., Ross, H. P., and Nielson, D. L., 1981, Exploration strategy for high-temperature hydrothermal systems in Basin and Range Province: Bull. AAPG, v. 65, p. 86-102.

Ward, S. H., and Sill, W. R., 1976, Dipole-dipole resistivity surveys, Roosevelt Hot Springs KGRA: NSF Technical Report, 76-2, Univ. of Utah, 29 p.

Ward, S. H., Peeples, W. J., and Ryu, J., 1973, Analysis of Geoelectromagnetic Data, *in* B. A. Bolt, Ed.: Methods in Computational Physics, v. 13, p. 163-238, New York, Academic Press.

Word, D. R., Smith, H. W., and Bostick, F. X., Jr., 1970, An investigation of the magnetotelluric tensor impedance method: EGRL Tech. Rpt. 82, Univ. of Texas, Austin.

Wu, F. T., 1968, The inverse problem of magnetotelluric sounding: Geophysics, v. 33, p. 972-979.

Wyllie, P. H., 1979, Petrogenesis and the physics of the earth, *in* H. S. Yoder, ed., The Evolution of the Igenous Rocks, Princeton University press, p. 483-520.

Yungul, S. H., 1961, Magnetotelluric sounding three-layer interpretation curves: Geophysics, v. 26, p. 465-

Yusas, M. R., and Bruhn, R. L., 1979, Structural fabric and in-situ stress analyses of the Roosevelt Hot Springs KGRA: ESL Report DOE/ID/78-1701.a.6.5.1, 62 p.